

Machine Learning in Modeling of the Dynamics of Polymer Electrolyte Fuel Cells

Wei Zou

Energie & Umwelt / Energy & Environment

Band / Volume 560

ISBN 978-3-95806-601-4

Forschungszentrum Jülich GmbH
Institut für Energie- und Klimaforschung
Elektrochemische Verfahrenstechnik (IEK-14)

Machine Learning in Modeling of the Dynamics of Polymer Electrolyte Fuel Cells

Wei Zou

Schriften des Forschungszentrums Jülich
Reihe Energie & Umwelt / Energy & Environment

Band / Volume 560

ISSN 1866-1793

ISBN 978-3-95806-601-4

Bibliografische Information der Deutschen Nationalbibliothek.
Die Deutsche Nationalbibliothek verzeichnet diese Publikation in der
Deutschen Nationalbibliografie; detaillierte Bibliografische Daten
sind im Internet über <http://dnb.d-nb.de> abrufbar.

Herausgeber
und Vertrieb: Forschungszentrum Jülich GmbH
 Zentralbibliothek, Verlag
 52425 Jülich
 Tel.: +49 2461 61-5368
 Fax: +49 2461 61-6103
 zb-publikation@fz-juelich.de
 www.fz-juelich.de/zb

Umschlaggestaltung: Grafische Medien, Forschungszentrum Jülich GmbH

Druck: Grafische Medien, Forschungszentrum Jülich GmbH

Copyright: Forschungszentrum Jülich 2021

Schriften des Forschungszentrums Jülich
Reihe Energie & Umwelt / Energy & Environment, Band / Volume 560

D 82 (Diss. RWTH Aachen University, 2021)

ISSN 1866-1793
ISBN 978-3-95806-601-4

Vollständig frei verfügbar über das Publikationsportal des Forschungszentrums Jülich (JuSER)
unter www.fz-juelich.de/zb/openaccess.



This is an Open Access publication distributed under the terms of the [Creative Commons Attribution License 4.0](https://creativecommons.org/licenses/by/4.0/),
which permits unrestricted use, distribution, and reproduction in any medium, provided the original work is properly cited.

Abstract

Polymer electrolyte fuel cells (PEFCs) are a promising energy conversion technology that generates electricity from hydrogen with low noise, and less or zero emission properties. Phenomena during the fuel cell operation are complex, which are caused by many interrelated factors. In addition, the dynamic behaviors of the fuel cells will change due to different operating conditions and load changes. A fast response model that can predict the PEFCs dynamic behavior is helpful to implement optimal control to the fuel cell systems obtaining a desired performance.

The aim of the thesis is to developing, analyzing and modifying a fuel cell dynamic model, in which a least squares support vector machine (LSSVM) is employed. The efficiency of the LSSVM model is first demonstrated in comparison to experimental data collected from a fuel cell test rig. Analyzing the model's performance under various fuel cell load changes is carried out with the help of experimental data collected from our test rig and artificial data generated by a white-box model that based on the mechanism of the fuel cell systems. Two types of artificial data are generated: one is idealized artificial data with determined cell voltage and another one is oscillated artificial data that includes the oscillation on the cell voltage.

Various load changes, namely current density changes, are considered in the analysis, and are represented by a combination of two factors called as ramp time and ramp value. Ramp time is used to show how fast the load is changed and ramp value is used to describe the range of load change. In addition, considering the data-driven nature of the LSSVM method, sampling interval of the test rig that determines the frequency of data collection is considered. It is found that the performance of the LSSVM model is better when smoother load changes are imposed on the system, so large ramp time and small ramp value are preferable in order to achieve good model accuracy. Moreover, to modeling a high dynamic fuel cell system, a high frequency sampling is suggested to reach a desirable model performance.

The thesis defines a working zone for the LSSVM model when predicting the PEFCs dynamic response to sudden load change. Based on the acceptable error to the modeling, a set of workable combinations of sampling interval, ramp time and ramp value can be found. The working zone helps to instruct the future application of the LSSVM model when different operating load changes are applied.

Last but not the least, the LSSVM model is modified in order to improve its modeling performance when predicting the dynamic behavior of the fuel cell. An online adaptive LSSVM model is developed. Determination of initial value of the internal parameters to the LSSVM model is optimized by employing a genetic algorithm to search global optimum instead of manual search. An adaptive process is carried out to update these internal parameters online. With a suitable starting point of the internal parameters and online updating processes, this online adaptive LSSVM model can well deal with complex nonlinear fuel cell systems with frequent load changes.

Kurzfassung

Polymerelektrolyt-Brennstoffzellen (PEFCs) sind eine vielversprechende Energiewandlungstechnologie, die Strom aus Wasserstoff mit geringer Lautstärke und wenig oder keinen Emissionen erzeugt. Phänomene während des Brennstoffzellenbetriebs sind komplex und werden durch viele miteinander verbundene Faktoren verursacht. Darüber hinaus ändert sich das dynamische Verhalten der Brennstoffzellen aufgrund unterschiedlicher Betriebsbedingungen und Laständerungen. Ein schnelles Reaktionsmodell, das das dynamische Verhalten der PEFCs vorhersagen kann, ist hilfreich, um eine optimale Steuerung der Brennstoffzellensysteme zu implementieren und eine gewünschte Leistung zu erzielen.

Ziel der Arbeit ist es, ein dynamisches Modell für Brennstoffzellen zu entwickeln, zu analysieren und zu modifizieren, in dem eine Least-Squares-Vektor-Maschine (LSSVM) eingesetzt wird. Die Effizienz des LSSVM-Modells wird zunächst im Vergleich zu experimentellen Daten demonstriert, die von einem Brennstoffzellen-Teststand gesammelt wurden. Die Analyse der Leistung des Modells unter verschiedenen Laständerungen der Brennstoffzelle erfolgt mit Hilfe von experimentellen Daten, die von unserem Teststand gesammelt wurden, und künstlichen Daten, die von einem White-Box-Modell generiert wurden, das auf der Funktionsweise der Brennstoffzellensysteme basiert. Es werden zwei Arten von künstlichen Daten erzeugt: eine sind idealisierte künstliche Daten mit deterministischer Ausgabe und eine andere sind künstliche Daten, die Oszillationen in der Zellenspannung enthalten.

Verschiedene Laständerungen, nämlich Änderungen der Stromdichte, werden in der Analyse berücksichtigt und durch eine Kombination von zwei Faktoren als Rampe dargestellt, nämlich die Dauer und die Höhe der Rampe. Die Rampendauer wird verwendet, um zu zeigen, wie schnell sich die Last ändert, und der Höhe der Rampe wird verwendet, um den Bereich der Laständerung zu beschreiben. Gemäß der datengesteuerten Natur des LSSVM-Modells wird außerdem das Abtastintervall des Teststandes berücksichtigt, das die Frequenz der Datenerfassung bestimmt. Es zeigt sich, dass die Leistung des LSSVM-Modells besser ist, wenn dem System moderate Laständerungen auferlegt werden. Daher führen eine hohe Rampendauer und eine kleine Rampenhöhe zu einer guten Modellgenauigkeit. Darüber hinaus wird zur Modellierung eines hochdynamischen Brennstoffzellensystems eine hohe Abtastfrequenz vorgeschlagen, um die Güte des Modells zu erhöhen.

Das Manuskript definiert eine Arbeitszone für das LSSVM-Modell für den Fall, dass die dynamische Reaktion der PEFC auf Laständerungen vorhergesagt werden soll. Basierend auf einer Fehlertoleranz bei der Modellierung kann eine Reihe praktikabler Kombinationen aus Abtastintervall, Rampendauer und Rampenhöhe gefunden werden. Die Arbeitszone hilft dabei, zukünftige Anwendung des LSSVM-Modells zu konfigurieren, wenn auf Änderungen der Betriebslast adäquat reagiert werden soll.

Zu guter Letzt wird das LSSVM-Modell modifiziert, um seine Qualität bei der Vorhersage des dynamischen Verhaltens der Brennstoffzelle zu verbessern. Ein adaptives Online-LSSVM-Modell wird entwickelt. Die Bestimmung des Anfangswertes der internen Parameter für das LSSVM-Modell wird optimiert, indem an Stelle der manuellen Suche ein genetischer Algorithmus verwendet wird, um das globale Optimum zu ermitteln. Ein adaptiver Prozess wird durchgeführt, um diese internen Parameter online zu aktualisieren. Mit einem geeigneten Ausgangspunkt für die internen Parameter und Online-Aktualisierungsprozesse kann dieses adaptive Online-LSSVM-Modell auch komplexe nichtlineare Brennstoffzellensysteme mit häufigen Lastwechseln bewältigen.

Table of Contents

Abstract	i
1 Introduction.....	1
1.1 Polymer electrolyte fuel cells	1
1.2 PEFCs in operation.....	3
1.2.1 Reactants flow rates.....	3
1.2.2 Operating temperature and pressure	4
1.2.3 Humidification.....	4
1.2.4 Load changes.....	4
1.3 Motivation	5
1.4 Contributions and organization of the thesis	6
2 Modeling methods for fuel cells dynamics	9
2.1 White-box models	10
2.1.1 Isothermal models	10
2.1.2 Non-isothermal models	11
2.2 Black-box models: data-driven methods	13
2.2.1 Artificial neural networks.....	14
2.2.2 Fuzzy logic	18
2.2.3 Support vector machine.....	19
2.2.4 Least-squares support vector machine.....	22
2.3 Gray-box models: parameter estimation methods	23
2.3.1 N-order polynomial regression.....	24
2.3.2 Genetic algorithm	24
2.3.3 Artificial neural networks.....	26
2.4 Conclusions and ideas	26
3 A LSSVM model for PEFCs dynamics	31
3.1 Time-varying voltage behavior	31
3.2 Least squares support vector machine.....	32
3.2.1 Cross-validation.....	33

3.3	Experimental setup	34
3.3.1	Dataset preparation	36
3.4	LSSVM model	38
3.4.1	LSSVM performance	40
3.5	Conclusions	41
4	Analysis of the suitability of the LSSVM model under ideal cases	43
4.1	Methodology	43
4.2	White-box model	44
4.3	Artificial data	48
4.4	The LSSVM model performance	53
4.4.1	Sampling interval	53
4.4.2	Ramp value	56
4.4.3	Ramp time	59
4.5	Analysis on the LSSVM model	61
4.6	Conclusions	64
5	Credibility of the LSSVM model under oscillation cases	65
5.1	Artificial data preparation	65
5.1.1	Experiments	66
5.1.2	Oscillation analysis	69
5.1.3	Artificial data validation	71
5.2	Impacts of factors on the LSSVM model	73
5.2.1	System's setup	73
5.2.2	Load changes	76
5.3	Working zone for the LSSVM model	82
5.4	Conclusions	86
6	An online adaptive model for nonlinear dynamics of fuel cell	87
6.1	Problem description	87
6.2	Methodology	88
6.2.1	Genetic algorithm	89

6.2.2	Gradient method	91
6.3	Online adaptive model.....	92
6.4	Model validation.....	93
6.4.1	Validation based on experimental data.....	93
6.4.2	Validation based on artificial data	101
6.5	Conclusions	103
7	Discussions	105
8	Conclusions.....	109
	Appendix	111
A.1	Workflow of the modeling process in chapter 3.....	111
A.2	Workflow of the modeling process in chapter 4.....	113
A.3	White-box model for generating artificial data.....	115
A.3.1	Voltage module.....	115
A.3.2	Anode module.....	116
A.3.3	Cathode module.....	117
A.3.4	Membrane module.....	118
A.4	Workflow of the modeling process in chapter 5.....	120
A.5	Workflow of the modeling process in chapter 6.....	123
	Reference.....	125
	List of Figures.....	131
	List of Tables.....	137
	Acknowledgments	139

1 Introduction

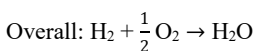
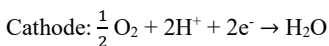
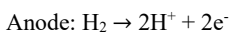
Ever increasing development in economic have escalated energy demands accompanied with the exploitation and utilization of fossil fuels, such as petroleum, coal, naturel gas and etc., through which produced large amount of the greenhouse gases and pollutant, which are released to the environments [1,2]. Public awareness for environmental protection and overexploitation has risen and the development of clean and renewable energy sources has attracted increasing interest and attention. It is foreseen that hydrogen energy technology will play an important role against global warming through replacement of fossil fuels [3]. Fuel cells are electrochemical energy converters that convert chemical energy of fuel into electricity and have been regarded as a promising energy converters for the future. When hydrogen is used as fuel, water is the only by-product. The fuel cells combine the best features of conventional heat engines and batteries: as an engine, the fuel cells are able to delivery electricity as long as fuel is available; as a battery, no intermediate mechanical energy conversion exhibits in the fuel cells and the characteristics of fuel cells are similar to a battery under load changes [4].

There are five main categories of fuel cells that have received primary efforts of research in recent years: 1) Polymer electrolyte fuel cells (PEFCs); 2) Direct methanol fuel cells (DMFCs); 3) Solid oxide fuel cells (SOFCs); 4) Alkaline fuel cells (AFCs); 5) Molten carbonate fuel cells (MCFCs).

Amongst, the PEFCs, due to its simplicity, viability, and quick start-up, have been considered as major participant in energy diversification and recommended for portable devices, space vehicles, military technology, stationary power and automotive vehicles [5–10]. Although PEFCs have passed the demonstration phase and are starting to move into the commercialization phase, there are still a wide range of challenges have to be overcome to achieve worldwide commercialization of the PEFCs.

1.1 Polymer electrolyte fuel cells

The polymer electrolyte fuel cells are energy converters that transform chemical energy directly into electrical energy. Fuel and oxygen are continually delivered to the fuel cell then generate electricity. The electrochemical reactions occur simultaneously on anode and cathode sides. Electrolyte separates the reaction spatially, which allows only protons passing through and not electrons. As pure hydrogen is used as fuel and oxygen as oxidant, water is the only by product, its reaction can be described as:



1 Introduction

At the anode side, hydrogen is split by electrocatalytical processes into protons and electrons. The protons are passing through the membrane directly but the electrons are forced to be transferred through the exterior circuit. At the cathode side, oxygen enters the fuel cell and then combines with electrons that are delivered from the exterior circuit and protons that are passing through the electrolyte.

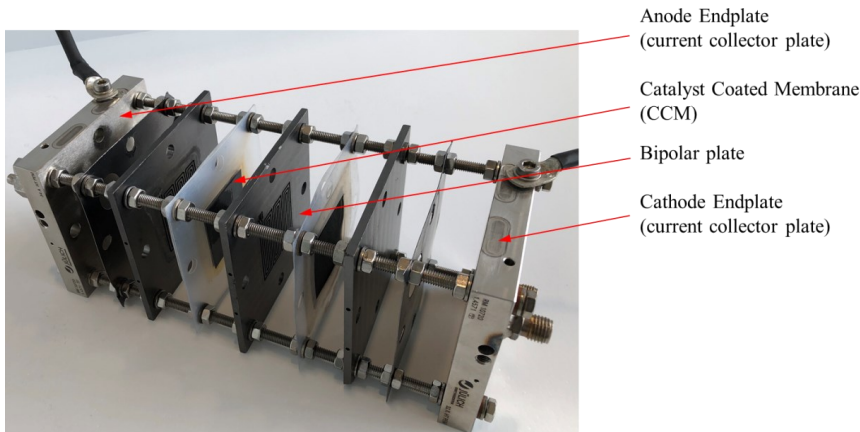


Figure 1-1: The main parts of a PEFC in Forschungszentrum Jülich: Exposed fuel cell components.

The main parts of a PEFC are illustrated in Figure 1-1. Endplates are usually used to compress the fuel cell stack from the outer ends of a single cell or a fuel cell stack, which maintain the stack structure and prevent reactant gas leakage. The materials can be stainless steel, aluminum, magnesium, gold-coated or carbon based composite materials [11,12]. They are also called as current collector plates, which conduct the electrical current from the end anode to the corresponding end cathode via an external circuit. Bipolar plates are traditionally fabricated from graphite composite as good electrical conductivity, corrosion resistance, and low gas permeability are required. It is also important to electrically connect the anode and the cathode and provide flow-fields of reactive gases [13,14]. Bipolar plates, also called gas flow plates, form a major part of the weight and volume of the PEFCs. They distribute the reactants to the cell and remove the products while conducting the electrons and heat. Insufficient supply of reactant gases results in fuel/oxidant starvation, reducing cell performance and durability. Local hot spot formation can degrade the membrane and cause pin-hole or crack formation. Thus, the bipolar plates must be conformable, high-strength but lightweight, thermally and electrically conductive, and impermeable to gases [5]. Gas diffusion layers (GDLs) provide a flow path for reactant supply and product removal. A porous material in the design of the GDL is essential. Through the vacant space of the GDL, the reactant gases move from the gas flow channel towards the catalyst layers, and distribute along the area, while electrons and heat can

be transferred through the remaining solid structure [15]. It also provides robust mechanical support and protection for the delicate catalyst layer and membrane during both assembly and operation [16]. Membrane is coated with catalyst layers on each side to form a catalyst coated membrane (CCM). The membrane exhibits non-electrically conducting but high ionic conductivity, and is designed to conduct only protons while block the transportation of electrons and reactant gases. The electrons are forced migrates through the external circuit but the proton can be transport directly through the membrane.

1.2 PEFCs in operation

Phenomena during fuel cell operation are complex, involved in several physical processes including mass/heat transfer, electrochemical reactions, ionic/electronic transport [8,17,18]. During the operation of the PEFCs, frequent load change is inevitable. The dynamic responses of the fuel cell under load changes are influenced by many highly coupled factors including the membrane hydration, the charge double-layer effects, the operating temperature, and the mass transfer mechanism. Understanding the dynamic behavior of the PEFCs is important to reach better performance and longer lifetime [19].

1.2.1 Reactants flow rates

The reactants to some extent must be supplied in excess of they have been consumed. The ratio between the supplied rate and the consumed rate of the reactant is called stoichiometric ratio or stoichiometry. Theoretically, hydrogen may be supplied at it is being consumed. But taking crossover permeation or internal currents into account, then the supply rate of hydrogen to the fuel cell is slightly higher than the consumption rate that is required by the electrical current demand. On cathode side, the stoichiometric ratio must greater than 1 in order to avoid oxygen starvation [20,21]. In addition, water is generated in cathode side; excess flow of reactant can flush out the water in case of water accumulation in the flow channel.

The stoichiometry indirectly affects the voltage output and the rate of water production, because it governs the flow rate of reactants, in other words, adjust their partial pressures [22]. A small stoichiometric ratio could lead to an uneven chemical reaction that causes many critical issues to the fuel cell such as non-uniform water, heat and current productions, and further causes flooding, hotspots, and reactant starvation [23,24]. Larger stoichiometric ratio brings about higher fuel cell performance¹, but the excessive gases will increase the burden of the compressor and consume more energy. During the operation of the PEFCs, altering anode

¹ This is reported with respect to fuel cell performance later in this paper. Higher fuel cell performance indicates higher cell voltage.

stoichiometric ratio will not bring about much impact on the performance of the fuel cell, while the variation of cathode stoichiometry changes the fuel cell performance significantly [25].

1.2.2 Operating temperature and pressure

Operating temperature and pressure are positively correlated with the fuel cell efficiency [26]. When the operating temperature is lower than anticipated temperature, the PEFCs will result in reduced performance. Generally, a higher temperature brings about a higher cell output. But if the fuel cell operates with temperature that is higher than required working temperature, it will cause not only fuel cell underperformance but also possibly permanent damage to the fuel cell materials [27]. In addition, the uniform temperature distribution of the PEFCs in operation brings in better performance and avoids the degradation of membrane and electrode caused by local hotspots [28]. Under some certain operating conditions, a more uniformly distributed temperature distribution can be achieved by increasing the operating pressure [29]. An increased operating pressure gains some potential then generates more power [30], but extra power is required when supply the PEFCs with pressurized reactant gases, which may offset the benefits brought by high operating pressure. So a tradeoff between the high power output and the system auxiliary consumption should be considered when increasing the operating temperature and pressure.

1.2.3 Humidification

In PEFCs systems, both the hydrogen and oxidant must be humidified before being delivered into the cell in order to prevent membrane drying out. Dehydration of the polymer electrolyte membrane limits the electrode kinetic reactions and brings on a makeable decrease in its ion conductivity, as consequence, causes energy losses due to the increase in the internal electrical resistance of the cell [31]. In general, the cell voltage is positive related to relative humidity, thus high relative humidity is preferred during fuel cell operation. Cho et al. [32] showed that the dynamic response of the PEFCs is optimal when both anode and cathode sides were fully-hydrated. In comparing with less hydrated operating conditions, smaller overshoot and undershoot are observed during load change at 100% relative humidity, what's more, resulting a higher fuel cell voltage. However, at high levels of humidification, the cell voltage drops sharply with increasing relative humidity, as void space in the gas diffusion layer may be filled by excess water then inhibits mass transfer.

1.2.4 Load changes

The dynamic behavior of the PEFCs under load change varies widely at different operating conditions. In the meantime, changing in load affects parameters such as the gas excessive coefficient, the temperature, the pressure, and the humidity [19].

Different load change behaviors have different effects on the fuel cell performance. Increasing same load range but with different time results in different dynamic response of the fuel cell. The shorter the time is and the faster the voltage changes, but the larger the magnitude of undershoot [33]. In addition, under same operating condition, increasing load from same starting point to different final points will lead to different fuel cell outputs. Larger load change value results more obvious undershoot and smaller cell voltage. Also, longer time is required to reach a new steady-state value [34].

1.3 Motivation

Modeling is the first step for many applications such as prediction, control and optimization. A model that can fully reflect the dynamic behavior of the PEFCs is necessary for achieving a stable, accurate and desirable fuel cell dynamic performance. Mechanism-based modeling methods and data-driven modeling methods are widely used to characterize the fuel cell operating processes. The mechanism-based method often leads to complex partial differential equation models with unknown uncertainties and often accompanied with some assumptions. They often result in infinite-dimensional models, making the reduction of the models' order necessary, which sacrifice the model accuracy for simplification. In addition, some uncertainties and disturbances showed up during the operation are impossible to be handled by the mechanism-based modeling methods. In contrast, the data-driven modeling methods derive from substantial processes, which merely rely on the prior knowledge, conceiving acceptance for its closeness in predicting the behavior of the fuel cell. Different from mechanism-based models that attempt to simulate heat transfer, mass transportation and electrochemical phenomena occurring within it, the data-driven modeling methods focus on the relationship among the fuel cell system's operating information without having deep insight on the physical and electrochemical phenomena – though considering them inherently with the data. This property makes the data-driven methods convenient for online analyzing the PEFCs dynamic behavior at different operating conditions and various load changes, then implements online predicting for the fuel cell dynamic behaviors. Therefore, they have been widely used in modeling fuel cell behaviors.

Data-driven method have many candidates. Neural networks (NNs) provides a nonlinear approximation which is robust against system noise when predicting the fuel cell voltage reduction caused by degradation during nominal operating condition [35]. Fuzzy logic was proposed to describe the dynamic behavior of a PEFC system and has reached a good degree of approximation [36]. Principal component analysis (PCA) is capable of extracting main factors from multiple variable vectors which can reveal the characters of them [37]. This data dimensionality reduction algorithm can be applied to identify the system in a less time-consuming way [38]. The support vector machine (SVM) method can reduce the dimensionality

and complexity of the system. It has been applied to predict the performance of a PEFC system, and the predictions by this modeling method were validated by the experimental with a coefficient of determination of approximately 99% [39]. Least squares support vector machines (LSSVM) have the ability to approximate any nonlinear system by mapping the input data in a primal space into a feature space [40]. They have already been used to predict the residual useful life of the PEFCs [41], and to build a nonlinear offline model for the PEFC stack in order to control the stack temperature [42]. Although the above-mentioned data-driven modeling methods have achieved an overall good modeling accuracy, their modeling performance under various load changes has not been clarified. Thus, the credibility of the data-driven modeling methods under different load demand (various current density changes) should be further discussed.

1.4 Contributions and organization of the thesis

The thesis will not only focus on the modeling problems of the dynamic behavior of the polymer electrolyte fuel cells, but also implements a systematic, qualitative and quantitative comprehensive evaluation on the fuel cell dynamic model.

The objective of this thesis is to develop a dynamic fuel cell model based on the least squares support vector machine (LSSVM), to investigate the impacts of the load changes on the model's performance, to analyze the credibility of the model in predicting the dynamic behavior under various load changes, to define the model's reliable working zone which regulates the load behavior, and to optimize the LSSVM model to improve its modeling performance and to better adapt the dynamics in the fuel cell. It mainly includes:

- To provide a systematic literature survey on the dynamic modeling methods;
- To establish a LSSVM model for PEFCs to predict its dynamic behavior;
- To analyze the LSSVM model under ideal cases, in which artificial data are introduced;
- To analyze the LSSVM model under oscillated cases, with the help of a statistical analysis on the fuel cell voltage information from experiments;
- To optimize the LSSVM model in order to improve its modeling performance;

In the following, the contents of each chapter are summarized with emphasizing the main contributions:

Chapter 2 introduces the dynamic modeling methods. Their pros and cons are summarized;

In Chapter 3, a least squares support vector machine is introduced and a dynamic model based on the LSSVM method for a PEFC voltage is established and validated against the experimental data;

In chapter 4, a mechanism-based white-box model is first introduced, by which artificial data are generated. The artificial data are used to investigate the suitability of the LSSVM model.

Here, only ideal cases are considered, in which determined fuel cell voltage are generated by the white-box model;

In chapter 5, the credibility of the LSSVM model under oscillated cases is discussed. Results from statistical analysis on the oscillation of the experimental cell voltage in combination with the artificial data generated in chapter 4 were used to generate oscillated artificial data. A reliable working zone for the LSSVM model is provided, by which the load changes are restrained;

In chapter 6, the LSSVM is modified in order to achieve a better modeling performance. Determination of initial value of the internal parameters to the LSSVM model is optimized by employing a genetic algorithm to search the global optimum instead of manually search. A fast running adaptive process is carried out to update these internal parameters online;

Chapter 7 discusses the main results;

Chapter 8 provides conclusions and suggestions for future research.

2 Modeling methods for fuel cells dynamics

Dynamic modeling methods for fuel cells are reviewed in this chapter. The modeling methods focusing on online prediction are classified into 3 groups: white-box models for known system in section 2.1, black-box models for unknown structure of system in section 2.2, and gray-box models for partially-known system in section 2.3. Section 2.4 draws the conclusions.

Fuel cell models are effective tools for understanding the electrochemical reaction, thermal behavior, and fluid transfer mechanism in the fuel cells undergoing various load changes. The main advantages of employing fuel cell models including cost effective, safety insurable and operation flexible as they can investigate critical situations without imposing any real-life danger, and be used to evaluate a fuel cell system under varying working conditions [39].

Dynamic behavior of the PEFCs can be observed at load changes [43]. The dynamic behavior of PEFCs is critical to evaluate the performance of the PEFCs for real application. For automotive application of a fuel cell, it often experiences various load changes, such as sudden start-up, shut-down, idle speed, and acceleration. A suddenly increase in load will lead to a fall of fuel cell voltage in a very short time, then gradually rose to a relatively stable state, showing a significant undershoot [44]. In this case, the fuel on the anode side was rapidly consumed, but it takes a certain time to deliver hydrogen to the active area, which results in hydrogen shortage, consequently, the fuel cell performance deteriorated [18].

Based on the models' dependency on the system mechanism and data, the models can be classified into three types: (1) white-box models, (2) gray-box models, or hybrid models, and (3) black-box models, or data-driven models, as shown in Figure 2-1. The white-box models are originated from the mechanism analysis on the system under some assumptions. Despite there are slight difference between the models and real systems, but they can still capture the dominant dynamics for the systems. The data-driven models are strongly relied on the data, and they can be only established after experimental data are collected from the system. The hybrid models are regarded as a combination of the white-box model and black-box model as they rely on not the prior knowledge but also experimental data. Generally, the structure of the system can be deduced from the prior knowledge, and only some parameters remained to be estimated from the data.

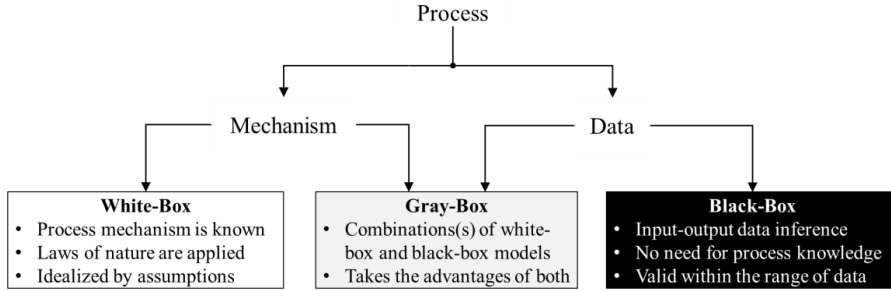


Figure 2-1: Classification of dynamic models based on their dependency on mechanisms and data [45]².

2.1 White-box models

The white-box models are derived from the underlying science and engineering laws. With the help of the previous researches on physical and chemical knowledge on the system, a mathematical description of the system is obtained. They provide a deep understanding about the fuel cell dynamics, and can be used to research how operating conditions and load changes affect the fuel cell performance during operation. The white-box models can provide numerical data about the fuel cells to the development a fuel cell controller. These numerical data can be used to test the accuracy and robustness of the controller, by which eliminating the experimental uncertainties and possible safety issues before applying the fuel cell controller to the real application. However, the establishment of the models confronts several challenges such as nonlinearity, multi-scales, disturbances, highly coupled properties, and high dimensionality. Considering that temperature changing rate is slower than electrical changes that vary within milliseconds, the temperature in some models is assumed being constant. Based on whether temperature is considered in the model, the white models can be classified into two types: isothermal models and non-isothermal models.

2.1.1 Isothermal models

Li et al. [43] established an 1-D isothermal transient model considering gas species transport in porous electrode, water transport in membrane, and electrochemical reactions and current transport. Only single-phase flow was considered. The temperature of fuel cell was assumed be well controlled, which remaining constant during the whole modeling process. With their model, dynamic behavior of the PEFCs under multiple cathode gas humidity was studied.

² "Reprinted from Applied Energy, 228, Sohrab Zendehboudi, Nima Rezaei, Ali Lohi, Applications of hybrid models in chemical, petroleum, and energy systems: A systematic review, Pages No. 2539-2566, Copyright (2018), with permission from Elsevier"

Na et al. [46] presented a dynamic nonlinear model for a nonlinear PEFCs controller on the purpose of prolonging the lifetime of the fuel cell stack. In their model, the ideal gas law and mole conservation rule were applied and the partial pressure of water on the anode side and nitrogen on the cathode side were included. With the help of the nonlinear model, a controller was constructed that aims at controlling the pressure difference between both two sides in a certain small range thus to protect the membrane from damage.

Chavan et al. [47] proposed a simple, flexible model running in Matlab/Simulink environment in order to evaluate the PEFCs' performance under different hydrogen flow rates, humidity, and partial pressures. With the help of their model, the effects of each parameter on the cell performance can be easily discussed. They found that sufficient hydrogen must be supplied to the fuel cell to avoid voltage suddenly goes down, and well-hydrated hydrogen benefits the fuel cell performance because high voltage is reached by the cell with high relative humidity.

Wang et al. [48,49] established a 3D transient CFD model, by which revealed the importance of gas transport through the gas diffusion layer (GDL), electrochemical double-layer discharging, and membrane hydration, especially their properties in transience. During their models, it took 10 s of the system to reach the steady state because the water accumulated in the membrane. In addition, they subsequently illustrated the interactions between the water transport dynamics and cell voltage response.

Abovementioned models assumed that the temperature in the fuel cell has been well controlled. Though these models presented a series good understanding of the dynamic behavior of the PEFCs and how the system parameters affect the fuel cell, still, due to their lack of consideration on the effects of the fuel cell temperature, these models still have their limitations.

2.1.2 Non-isothermal models

Shan et al. [50–52] developed non-isothermal dynamic fuel cell models and studied the effects of temperature on the transient behavior of the PEFCs. A one dimensional model [50] for a single fuel cell was first established, in which the energy conservation equation is used to express thermal dynamics. They spotted the highest temperature at the cathode catalyst layer, and associated it with the over potential at this side is higher than the other side. Also, they found that the slow response of temperature to current density decrease is the reason of second wave of voltage overshoot. The first overshoot was caused by the variation of the proton concentration, while the second is due to the slow increase of temperature in all the layers. The effects of temperature on a PEFC stack were also discussed [51]. First, the impact of temperature (from 333 K to 363 K by 10 K) on the fuel cell under steady state was discussed. The polarization curves showed that the higher the temperature, the better the fuel cell

performance. Then, dynamic behavior was considered. The rising time of each cell's temperature was found closely related to where a cell is located in the stack. The heat of the end cells can be quickly dissipated to endplates, while middle cells are stored in the cell itself, and as a result, the middle cell had the highest temperature among others. A two-dimensional model [52] considering two-phase flow was used to analyze the dynamic temperature distribution in the through-plane direction the fuel cell stack that had two cells. The anode side of cell 1 and cathode side of cell 2 were next to the endplates. The mass and charge transport were described by using the mass conservation equation and momentum conservation, and the heat flux was described by the Navier–Stokes and the energy conservation equations. Same increase in temperature of both cells was found when the stack got operated (temperature was measured within 0.1 s). The highest temperature was found in the cathode catalyst layers of two cells. Over time, the heat flux diffuses and the temperature of all the planes risen. The endplate effect became obvious from 0.2 s, as a low temperature at anode side of cell 1 was observed. From 0.5 s, the temperature difference on the both sides and the peak temperature values of both cells got larger. The temperature of cathode sides became higher than anode side, and the peak temperature of cell 1 was larger than that of cell 2. In the meantime, a better performance of cell 1 was found in comparing with cell 2, confirming that high temperature benefits the performance of fuel cell. The modeling results were compared with their previous model [50], and found that the voltage drop at the two-phase case is larger than that of at the single-phase flow.

Liso et al. [53] established a nonlinear dynamic model of the fuel cell to study temperature variations over fast load changes. The model is developed using electrochemical, thermodynamic and zero-dimensional fluid mechanics principles. Gibbs free energy and three voltage loss (activation loss, ohmic loss, and concentration loss) were considered in the fuel cell model. The gas flow behavior was considered in a lumped mode, no spatial information were included. All gases were assumed as ideal gas and mass balance was used to calculate the gas flow of the fuel cell with respect to time. Thermal behavior was model based on the energy balance. An increase in temperature was found when load is changed then smoothly decreased. As the temperature changed, even under constant load condition, the value of the cell voltage will also change.

Fly and Thring [54] used a lumped parameter fuel cell model validated by using an experimental data and to study the temperature regulation in a evaporative cooled PEFC stack. They found that the heat generation tripled within the stack while the temperature only increased by 3.5 °C, when the current density suddenly increased from 0.3 A cm⁻² to 0.8 A cm⁻². It takes few seconds for the temperature to reach a steady state. When the current density suddenly decreased from 0.8 A cm⁻² to 0.3 A cm⁻², the temperature decreased by 3.5 °C. But it took longer time than before for the temperature to reach a steady state.

Rakhtala et al. [55] built a PEFC dynamic model that was made using the relationship between output voltage and partial pressure of oxygen, hydrogen, and water. Then, the model was integrated into a fuzzy PID controller, by which the voltage variation rate in response to the load change can be adjust at a desired level. Mahjoubi et al. [56] established a multi-physical fuel cell model including electrical model and thermal model. Their model can accurately and precisely emulate the fuel cell dynamic behavior, and the model's estimation ability has been validated by the experimental data. With the help of the model, the impacts of temperature variation and air flow rate on the fuel cell were discussed. A best compromise between the temperature and air flow rate was found in order to ensure an optimal performance for their fuel cell.

Huangfu et al. [57] proposed a multi-physics dynamic model for solid oxide fuel cell, considering electrochemical reaction, fluid properties and thermal effects. In this model, a parameters sensitivity study was carried out by using statistical multi parameter sensitivity analysis method, and then the impacts of parameters on the modeling accuracy were analyzed.

Obtaining an accurate nominal description of a system, to most of the industry processes, is very difficult. Flawed theory and incomplete process knowledge result in white-box models with unknown model structure accompanying with unknown parameters. Beside, uncertainties existed in the process makes model parameters varying greatly with different working conditions, and then affect the accuracy of the models.

2.2 Black-box models: data-driven methods

Black-box models, due to its high dependency on the data collected from the system, are also called as data-driven methods. Specific knowledge of the intrinsic system behavior is not required by the black-box model. Monitored and historical data are used to learn the system's behavior and use to perform the modeling and predicting process. They are appropriate to the complex systems whose dynamic behavior cannot be estimated and derived from the mechanism-based analysis. The implementation and computation of the data-driven methods are faster and more time-saving when comparing with other techniques [58,59]. In general, establishing a black-box model has following steps: data collection, analysis, filtering, model training and model validation, as shown in Figure 2-2. If the results satisfy the modeling requirements, then the model is used for prediction; otherwise, the model should be retrained. To establish a black-box model means the corresponding method is used for model training.

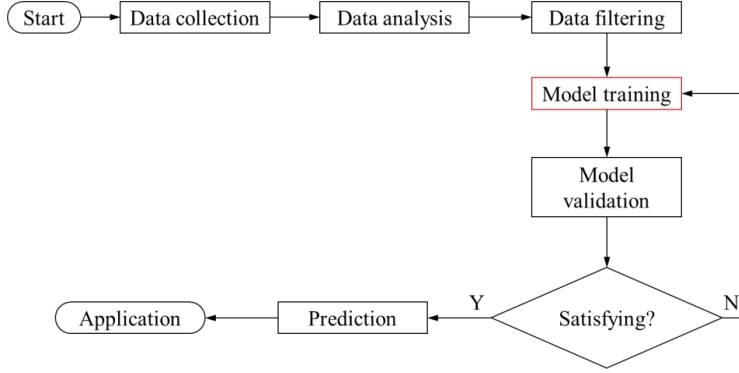


Figure 2-2: General processing procedure of black-box modeling.

2.2.1 Artificial neural networks

The human brain contains nerve cells, which are called as neurons. They are connected to one another, transmit and process the information received from our senses. Axons and dendrites are used during the information transmission and processing [60]. The connecting regions between axons and dendrites are referred to as synapses, and the connections are shown in Figure 2-3. The strengths of synaptic connections vary with regards to external stimuli. This variation is how learning happens in our brain [61].

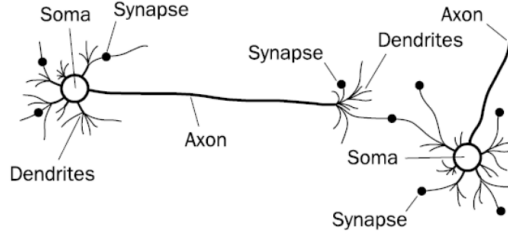


Figure 2-3: Biological neural network [62].

An artificial network (ANN) that inspired by the human brain consisting of neurons or nerve cells, shares the same concept of the network of neurons, and is used in machine learning algorithm. In the artificial network, computation units, also called as artificial neurons, are created artificially on a computer. The connections of the artificial neuron are called as weights that simulate the strengths of synaptic connections in our brain. An artificial neural network is created by computing a function of the inputs to the output(s) from the input neurons to the output neurons thorough the weights as intermediate parameters. Learning takes place by adjusting the weights connecting the neurons, where training data containing examples of input-output pairs is provided to artificial neural networks just as external stimuli are required for learning in human brain [61].

An ANN consists of three layers, namely input layer, hidden layer(s), and output layer. A typical three layers ANN is shown in Figure 2-4, in which the input layer consists of K input neurons, and each neuron represents an input variable x_1, \dots, x_K . N neurons are considered in the hidden layer, and the system has J outputs y_1, \dots, y_J . The weights (w) that connect the neurons are adjusted based on training input-output pairs.

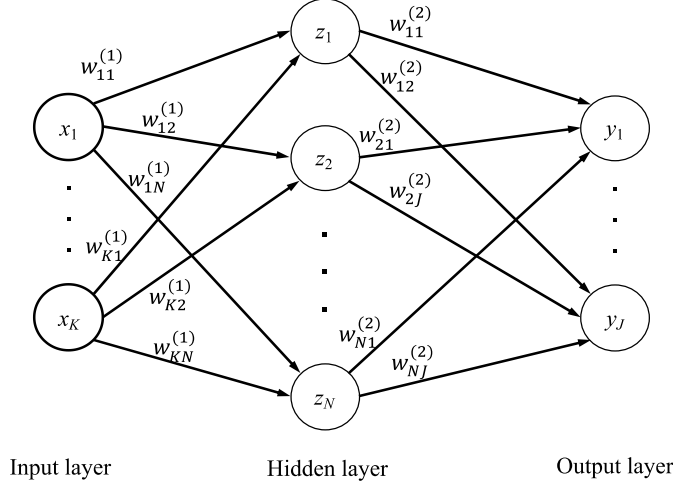


Figure 2-4: Configuration of an artificial neural network with three layers: one hidden layer.

The mathematical formulation for the nodes in hidden layer with K inputs is as following:

$$z_n = g \left(\sum_{k=1}^K w_{kn}^{(1)} x_k + b_n^{(1)} \right) \quad (2-1)$$

here, $w_{kn}^{(1)}$ denotes the controlling weight mapping input x_k to the hidden node z_n , and $b_n^{(1)}$ is the bias term, $g(\cdot)$ stands for activation function.

The multi-outputs are given by the following expression:

$$\hat{y}_j = f \left(\sum_{n=1}^N w_{nj}^{(2)} z_n + b_j^{(2)} \right) \quad (2-2)$$

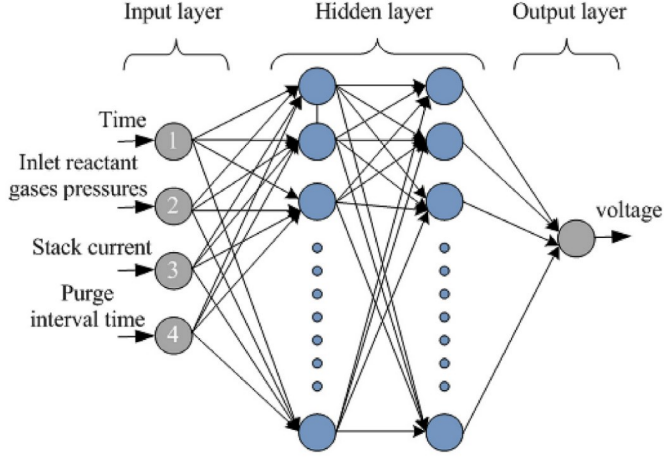
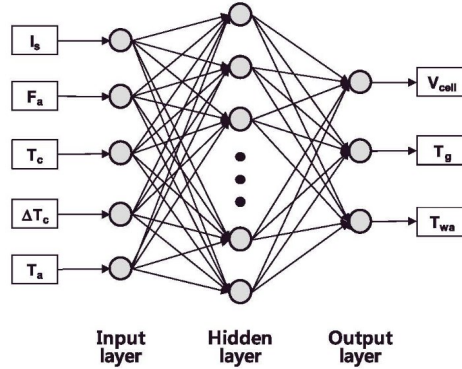
here, $w_{nj}^{(2)}$ denotes the controlling weight mapping hidden layer nodes z_n to the ANN output \hat{y}_j , $b_j^{(2)}$ is the bias term, $f(\cdot)$ stands for transfer function. The commonly used activation and transfer functions are listed in Table 2-I.

Table 2-I: Activation and transfer functions used in the ANNs [63].

Activation function	Formula	Output range
Step	$g(x) = \begin{cases} 1 & x \leq 0 \\ -1 & x > 0 \end{cases}$	$[-1, 1]$
Bipolar step	$g(x) = \begin{cases} 1 & x < 0 \\ 0 & x = 0 \\ -1 & x > 0 \end{cases}$	$[-1, 1]$
Unit step	$g(x) = \begin{cases} 1 & x \leq 0 \\ 0 & x > 0 \end{cases}$	$[0, 1]$
Linear	$g(x) = x$	$[-\infty, \infty]$
Piecewise linear	$g(x) = \begin{cases} 1 & x < 0 \\ x + 1/2 & -1/2 \leq x \leq 1/2 \\ 0 & x > 0 \end{cases}$	$[0, 1]$
Symmetric ramp	$g(x) = \begin{cases} a & x < a \\ x & -a \leq x \leq a \\ -a & x > a \end{cases}$	$[-a, a]$
Sigmoid	$g(x) = \frac{1}{1 + e^{-x}}$	$[0, 1]$
Bipolar sigmoid	$g(x) = \frac{1 - e^{-x}}{1 + e^{-x}}$	$[-1, 1]$
Tangent hyperbolic	$g(x) = \tanh(x) = \frac{e^x - e^{-x}}{e^x + e^{-x}}$	$[-1, 1]$
Gaussian	$g(x) = \frac{1}{\sqrt{2\pi}\sigma} e^{\left \frac{-(x-\mu)^2}{2\sigma^2} \right }$	$[0, 1]$

Collecting the experimental data is the first step to build the model. And the collected data are randomly divided into two datasets, meaning training dataset for establishing model and testing dataset for validating the neural network model. The activation and transfer functions are critical to the establishment of neural network model. They are carefully selected based on different modeling problems and type of system outputs. The number of hidden layers and nodes used in each hidden layer are the tuning parameters in the neural network. ANNs model is trained by increasing the number of hidden nodes as well as the number of hidden layers from 1 to a target number. In general, with the increasing number of hidden layers and hidden nodes, the model complexity increases whereas the training error decreases. Therefore, tradeoff between the neural network model accuracy and model complexity should be carefully determined.

Barzegari et al. [64] employed an ANN method to build a model for the PEFCs stack, as shown in Figure 2-5. The input layer of ANN was comprised of four inputs, namely time, inlet reactant gases pressures, stack current and purge interval time. And stack voltage was considered to be the output layer of ANN. Two hidden layers were employed. This ANN model can be employed to guide the controller design and fault diagnosis of the PEFCs stack operating on pure oxygen and hydrogen in dead-end condition.

Figure 2-5: Two hidden layers neural network model [64]³.Figure 2-6: Neural network structure for modeling the stack-humidifier [65]⁴.

Han et al. [65] developed an empirical model for the stack-humidifier to predict three variables, namely the average cell voltage of the stack (V_{cell}), the temperature of the stack exhaust gas (T_g), and the temperature of the humidified air from the humidifier (T_{wa}). In Figure 2-6 shows the structure of the neural network, which consists of the five input variables

³ "Reprinted from Energy, 188, Mohammad Mahdi Barzegari, Seyed Majid Rahgoshay, Liliya Mohammadpour, Davood Toghraie, Performance prediction and analysis of a dead-end PEMFC stack using data-driven dynamic model, Pages No. 116049, Copyright (2019), with permission from Elsevier"

⁴ "Reprinted from Energy Conversion and Management, 113, In-Su Han, Sang-Kyun Park, Chang-Bock Chung, Modeling and operation optimization of a proton exchange membrane fuel cell system for maximum efficiency, Pages No. 52-65, Copyright (2016), with permission from Elsevier"

including the stack current I_s , the air flow rate to the stack F_a , the cooling water temperature T_c , the temperature rise of the cooling water through the stack ΔT_c , and the air temperature T_a). They used sigmoid formula as activation function, and linear formula as transfer function. The root mean squared error between the predicted and measured outputs, obtained from the neural network model and from the testing data set was used as the criterion to determine the optimal number of hidden nodes. After the model was established, the sensitivity analysis with respect to the system efficiency was carried. The results showed that both the air flow rate F_a and the cooling water temperature rise ΔT_c , have greater impact on the system efficiency than others. In addition, an increase in the air flow rate has either positive or negative effect on the system efficiency depending on the applied power load.

2.2.2 Fuzzy logic

When humans make decisions in their daily life, due to the imperfect senses and observation instruments of human beings, the decisions are not always reach an infinite precision, but with uncertainty. For example, when the basin is full of water, we can know the temperature of the water in the basin by a thermometer, and then we need to make a decision: whether it is safe to reach into the water. The decision making may include a range of possibilities between YES and NO, as listed in Table 2-II. These decisions are drawing by our “intuition” and “gut-feelings”, which can only make after learning from experience [66].

Table 2-II: Fuzzy decision of humans whether they reach their hand into the water.

Temperature	Decision
<40°C	Definitely YES
40°C ~ 45°C	Possible YES
45°C ~ 50°C	Cannot Say
50°C ~ 70°C	Possibly NO
>70°C	Definitely NO

Fuzzy logic (FL) was first proposed by Zadeh [67] aiming at modeling human thinking and reasoning, trying to equip computers with the ability of humans processing special data as well as making use of their experiences and insights. It is capable of expressing a complex system in the form of fuzzy implications and has been reported to smoothly approximate any nonlinear system over a large working region [68]. In general, the fuzzy logic consists of three parts: fuzzification unit, rule processing unit, and de-fuzzifier unit and output information [69]. A membership value is assigned to each numerical data (quantitative information) entering into the fuzzification unit. Based on the membership value, the numerical parameters of input and output variables were fuzzified as linguistic classes, for example, very very low, very low, low, negative medium, medium, positive medium, high, very high and very very high [69]. The

rule processing unit forms the linguistic classes as *if-then* rules. The statement is: *if* antecedent proposition *then* consequent proposition. Results obtained using logical decision propositions according to the structure of the problem is sent to the de-fuzzifier unit, then each fuzzy information is converted into real number with scale change.

Let X be input (regression) matrix and Y an output, x the antecedent variable representing the input in the fuzzy system, and y the consequent variable related to the output of the fuzzy system, then the linguistic fuzzy consists of rules R_i is given as [70]:

$$R_i: \text{if } x \text{ is } A_i \text{ then } y \text{ is } B_i, \quad i = 1, 2, \dots, P$$

here, A_i and B_i being linguistic classes fuzzy sets defined by $\mu_{A_i}(x): X \mapsto [0, 1]$ and $\mu_{B_i}(y): Y \mapsto [0, 1]$ respectively; $\mu_{A_i}(x)$ and $\mu_{B_i}(y)$ are membership functions of the correspondent variables; R_i denotes the i^{th} rule and P is the number of rules in the rule base.

Fuzzy logic can be effectively employed in engineering, science, and business for a variety of purposes such as decision making, analysis of complex problems, function approximation, process control, risk assessment, and classification. In addition, it can address disturbances in systems, so are widely used in modeling fuel cells or stacks, which can reach a good degree of approximation in the systems themselves [35].

Zhang and Gang [71] used a Takagi–Sugeno (T–S) fuzzy model to represent approximately the nonlinear dynamics of solid oxide fuel cells (SOFCs). Since the fuzzy model approximates locally and dynamically the nonlinear dynamics by a set of linear models at each sampling period, linear model predictive control theory can be used easily to design an offset-free fuzzy model predictive control for the load following of SOFCs. Within the fuzzy model, fuel utilization, hydrogen/oxygen ratio, and pressure difference are used to monitoring the operating fuel cell performance.

Kheirandish et al. [36] established a fuzzy model for fuel cell system. Four properties were used to describe the fuel cell system, namely hydrogen flow rate, temperature, relative humidity, and efficiency of the system. The fuzzy rules were applied to explain the causes and effects between system properties instead of using analytical descriptions, thus eliminated the need for expert knowledge.

Yang et al. [72] reported a dynamic fuzzy model of a MCFC, which consists of a voltage and a temperature sub-model. However, the temperature sub-model can only be valid within a relatively narrow temperature range. In addition, the identification procedure of the model, which contains an antecedent identification and a consequent identification, is complicated.

2.2.3 Support vector machine

Support vector machines (SVMs) were introduced in the 1960s, which apply the structural risk minimization rule, and exhibits good performance even with noise-contaminated data or high dimensional data [73]. The idea is to find a way that separates features with maximum

margins. As shown in Figure 2-7, there are two features in the dataset, marked as class 1 (circles) and class 2 (squares). The dash line separates the two features, which is called as separation decision. On both sides of the dash line, through the points closest to the dash line draws a solid line parallel to the dash line. The distance between the two solid lines is called margin. Figure 2-7 shows two separation decisions. It can be found that the margin in Figure 2-7a is smaller than that of in Figure 2-7b, which means a poorer separation decision of Figure 2-7a.

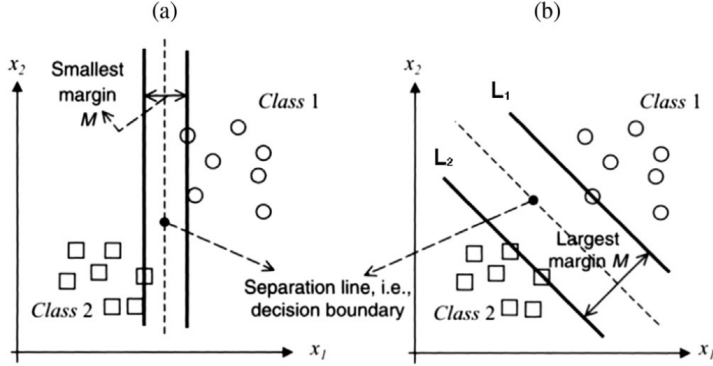


Figure 2-7: Classification of class 1 (circles) and class 2 (squares) data using a line classifier, having: (a) the smallest margin and (b) the largest margin [74] ⁵.

Let the training data set to be shown with $\{(x_i, y_i), i = 1, 2, \dots, N\}$, where $x_i \in \mathbb{R}^n$ is the input data which has d dimensions, N the number of training data points, y_i that can take values of $+1$ or -1 will help to classify the input data. The decision function is then obtained as follows:

$$y = \text{sgn}(\langle \omega, \varphi(x) \rangle + b) \quad (2-3)$$

here, ω is the weight vector in the primal weight space, and b the bias term, $\varphi(x): \mathbb{R}^n \rightarrow \mathbb{R}^{n_h}$ is a projected function mapping the input data onto a higher dimensional feature space. For a data point (x, y) , if $y = 0$, then the x falls on the separation line that is shown by the dash line in Figure 2-7. If $y = 1$, then the x falls on the solid line that belongs to class 1, which if $y = -1$, x falls on the solid line that belongs to class 2. The optimal classification is to find the largest margin that separates the data, then the optimization problem can be written as [75]:

$$\begin{aligned} \min \frac{1}{2} \|\omega\|^2 \\ \text{s.t. } y_i(\langle \omega, \varphi(x_i) \rangle + b) \geq 1 \end{aligned} \quad (2-4)$$

⁵ "Reprinted by permission from Springer nature [Support Vector Machine – An Introduction] by Vojislav Kecman, Copyright (2005) "

This optimization problem can be converted to a so-called dual problem. In the present case, it will turn out that it is more convenient to deal with the dual. To derive it, we introduce the Lagrangian multipliers ($\alpha_i \geq 0$) were introduced:

$$\min_{\omega, b} \mathcal{L}(\omega, b, \alpha) = \frac{1}{2} \|\omega\|^2 - \sum_{i=1}^N \alpha_i (y_i (\langle \omega, \varphi(x_i) \rangle + b) - 1) \quad (2-5)$$

The objective is then to minimize Eq. 2-5 with respect to ω and b and simultaneously require that the derivatives of $\mathcal{L}(\omega, b, \alpha)$ with respect to all the α vanish. The Karush-Kuhn-Tucker (KKT) conditions establish the requirements that need to be satisfied by an optimum solution to a general optimization problem. Given the optimization problem in Eq. 2-5, KKT conditions state that the conditions for optimality are given by:

$$\frac{\partial}{\partial \omega} \mathcal{L}(\omega, b, \alpha) = 0 \rightarrow \omega = \sum_{i=1}^N \alpha_i y_i \varphi(x_i) \quad (2-6)$$

$$\frac{\partial}{\partial b} \mathcal{L}(\omega, b, \alpha) = 0 \rightarrow \sum_{i=1}^N \alpha_i y_i = 0 \quad (2-7)$$

Substituting Eq. 2-6 and 2-7 into 2-5 results the formulation:

$$\begin{aligned} \max_{\alpha} \mathcal{L} &= \sum_{i=1}^N \alpha_i - \frac{1}{2} \sum_{i=1, j=1}^N \alpha_i \alpha_j y_i y_j \varphi(x_i) \varphi(x_j) \\ \text{s.t. } \sum_{i=1}^N \alpha_i y_i &= 0, \text{ and } \alpha_i \geq 0 \end{aligned} \quad (2-8)$$

As the optimization problem depends on the dot product of the sample vectors, by employing kernel function $K(x_i, x_j) = \varphi(x_i) \varphi(x_j)$ that corresponds to a dot product in some expanded feature space, the problem of transformation to feature space can be simplified to find a kernel function $K(x_i, x_j)$. A summary of common kernel functions is presented in Table 2-III data points with $\alpha_i > 0$ are called “support vectors” and they lie on either of the solid lines belonging to class 1 or 2, shown in Figure 2-7.

Substituting Eq. 2-6 into the decision function Eq. 2-3, the resulting SVM model is as following:

$$\hat{y} = \text{sgn}(\sum_{i=1}^N \alpha_i y_i K(x_i, x_j) + b) \quad (2-9)$$

Table 2-III: Commonly used kernel functions [76].

Kernels	Formula
Linear	$K(x, x_j) = \langle x, x_j \rangle$
Polynomial	$K(x, x_j) = (c + (x, x_j))^a$
Radial basis function	$K(x, x_j) = \exp\left(-\frac{\ x - x_j\ ^2}{2\sigma^2}\right)$
Sigmoid	$K(x, x_j) = \tanh(\eta(x, x_j) + \vartheta)$
Fourier series	$K(x, x_j) = \frac{\sin(a + \frac{1}{2})(x - x_j)}{\sin(\frac{1}{2}(x - x_j))}$
Additive	$K(x, x_j) = \sum_i K_i(x, x_j)$

Kheirandish et al. [39] proposed a fuel cell model using a SVM. They proposed a method of using SVM to predict the performance of PEMFC system for commercial electric bicycles. Because these units are nonlinear, multi variable system is difficult to model with the traditional method, so the SVM method is applicable to nonlinear condition. Bressel et al. [77] proposed a fuel cell model using a SVM. They suggested a method for predicting the performance of PEFC systems using a SVM for commercial electric bicycles. Since such units are non-linear, multivariable systems are hard to model by traditional methods, so the SVM method is suitable for nonlinear conditions. As mentioned above, the key issue of the model based approach is how to model the system. And as the dynamic changing of the system, the model should be created to be intelligent. The future direction of the model based approach would be more intelligent and combine with other methods.

Li et al. [78] employed the support vector machine (SVM) to detect and isolate possible faults for PEFCs in real time. An offline SVM model was first trained on the basis of historical data, with different operating states categorized. With this diagnosis model, the real-time information was well-organized and the operating state determined.

2.2.4 Least-squares support vector machine

The least squares support vector machine (LSSVM) approach is a machine learning technique which is based on the statistical learning theory and structural risk minimization principle. The LSSVM was derived from the SVM, and proposed by Suykens and Vandewalle [40,79]. As a least squares version of SVM, LSSVM inherits the superior generalization performance of SVM; while only solve a set of linear, rather than quadratic, equation programming problems. Although its precision is slightly lower than that of SVM, LSSVM significantly reduces computation time [80]. LSSVM is thus regarded as a powerful tool for modeling complex nonlinear systems and its accuracy and efficiency have been proven in many research and application fields [81]. The LSSVM can be expressed as follows [82]:

$$y = \omega^T \varphi(x) + b \quad (2-10)$$

where $x \in \mathbb{R}^n$, $y \in \mathbb{R}$, $\varphi(\cdot): \mathbb{R}^n \rightarrow \mathbb{R}^{n_h}$ is a nonlinear function that maps the input space into a higher dimension feature space. By utilizing training data $\{(x_i, y_i), i = 1, 2, \dots, N\}$, the optimization problem of the LSSVM method is as follows [40]:

$$\min_{\omega, b, e} J(\omega, e) = \frac{1}{2} \omega^T \omega + \frac{\gamma}{2} \sum_{i=1}^N e_i, \gamma > 0 \quad (2-11)$$

$$\text{s.t. } y_i = \omega^T \varphi(x_i) + b + e_i$$

where γ is the regularization term that marks a tradeoff between the model's accuracy and its capacity for generalization. In order to solve this optimization function, a Lagrangian parameter α_i is defined. The conditions for optimality are as follows:

$$\mathcal{L}(\omega, b, e; \alpha) = J(\omega, e) - \sum_{i=1}^N \alpha_i \{\omega^T \varphi(x_i) + b + e_i - y_i\} \quad (2-12)$$

with Lagrangian parameter α_i , the conditions for this optimization are as follows:

$$\begin{cases} \frac{\partial}{\partial \omega} \mathcal{L} = 0 \rightarrow \omega = \sum_{i=1}^N \alpha_i \varphi(x_i) \\ \frac{\partial}{\partial b} \mathcal{L} = 0 \rightarrow \sum_{i=1}^N \alpha_i = 0 \\ \frac{\partial}{\partial e_i} \mathcal{L} = 0 \rightarrow \alpha_i = \gamma e_i \\ \frac{\partial}{\partial \alpha_i} \mathcal{L} = 0 \rightarrow \omega^T \varphi(x_i) + b + e_i - y_i = 0 \end{cases} \quad (2-13)$$

After eliminating e_i and ω , the solution for α and b is given by a set of linear equations:

$$\begin{bmatrix} 0 & \vec{1}^T \\ \vec{1} & \Omega + \gamma^{-1} I \end{bmatrix} \begin{bmatrix} b \\ \alpha \end{bmatrix} = \begin{bmatrix} 0 \\ y \end{bmatrix}$$

where $y = [y_1; \dots; y_N]$, $\vec{1} = [1; \dots; 1]$, $\alpha = [\alpha_1; \dots; \alpha_N]$, while from the Mercer condition we get the following [83]:

$$\Omega = \varphi(x) \varphi(x_i) = K(x, x_i)$$

here $K(x, x_i)$ is the kernel function, for which a variety of functions can also be used, see Table 2-III.

Then, the result for the LSSVM method is as follows:

$$y = \sum_{i=1}^L \alpha_i K(x(t), x(t_i)) + b \quad (2-14)$$

where α_k and b are the solutions of Eq. (2-13).

Based on the framework of statistical learning theory and structural risk minimization, LSSVM is regarded as an effective tool for establishing nonlinear models and is applied to various engineering problems. It can be used for both steady-state and dynamic modeling. Huo et al. [84] used the least squares support vector machine to establish a steady-state model of solid oxide fuel cells (SOFCs), in which the fuel utilization and cell current were selected as the model input and the cell voltage as the output. Wu et al. [85] used a least squares support vector machine classifier to establish a fault diagnosis model, by which the faults of the solid oxidant fuel cell could be identified and the remaining lifetime predicted. Zou et al. [86] successfully predicted the distributed temperature throughout the HT-PEFC on the basis of the LSSVM.

2.3 Gray-box models: parameter estimation methods

Gray-box models are regarded as combination of white-box models and black-box models, and inherit the physical significance of the white-box models and generalization capabilities of the black-box models. Gray-box models are suitable for the system, whose partial processes are known only a small part of the process is difficult to be conduct from analysis. Thus, it depends on not only the prior knowledge about the system but also the experimental data. To establish a gray-box model normally contains the following steps: to construct the physical-based model; to implement experiments and collect data; to adjust the model; to validate the model, as shown in Figure 2-8.

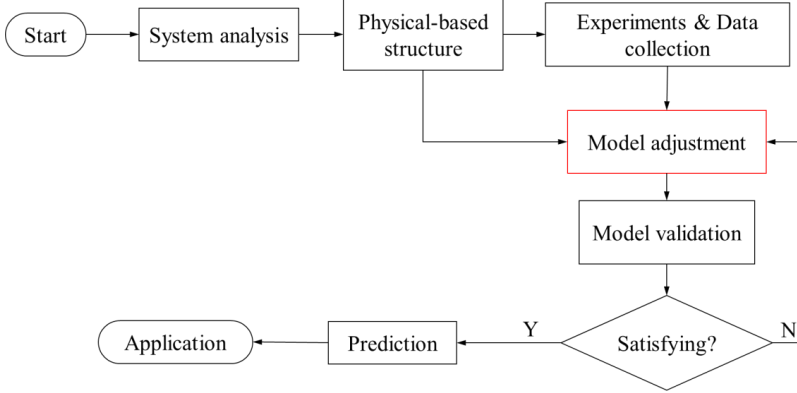


Figure 2-8: General processing procedure of gray-box modeling.

2.3.1 N-order polynomial regression

The n-order polynomial is an efficient modeling method to fit experimental data and predict mechanical properties. The standard polynomial form is [87]:

$$y = f(x, A) = a_0 + a_1x + \dots + a_nx^n \quad (2-15)$$

where $A = [a_0, a_1, \dots, a_n]^T$ is the polynomial coefficient vector, x the sampled data, y the output, and n the order of the model. In order to obtain the polynomial coefficients in Eq. 2-70, the optimization objective is:

$$J = \min\{\sum_{i=0}^m e_i^2\} = \min\left\{\sum_{i=0}^m (a_0 + a_1x_{(i)} + \dots + a_nx_{(i)}^n - y)^2\right\} \quad (2-16)$$

where, m is the number of calculations.

The optimization problem above can be solved when satisfied:

$$\frac{\partial J}{\partial a_j} = 2 \sum_{i=0}^m x_{(i)}^j (a_0 + a_1x_{(i)} + \dots + a_nx_{(i)}^n - y) = 0 \quad (2-17)$$

Linear and quadratic polynomials are commonly used to estimate system parameters and approximate the system process. Chavan et al. [88] presented an electrical circuit equivalent model of PEFCs in MATLAB. Least square optimization fitting algorithm was used to find parameters of equivalent circuit. Validation of simulation and practical results also presented. This model is most suitable to describe terminal behavior of the PEFCs. First- and second-order models were developed to identify which input factors affect the response variables significantly, in which current, hydrogen flow rate, operating temperature, and internal capacitance are discussed [89].

2.3.2 Genetic algorithm

Genetic algorithm (GA) is based on Darwin's theory of natural selection, where the fitter individuals are likely to survive in a competing environment. The theory of natural selection includes the following three aspects: inheritance, variation, and survival struggle [90]. The basic procedures of the GA are shown in Figure 2-9. The parameters that need to be identified

are grouped together as a parameter set that is regarded as an individual in the population. Many such parameter sets (individuals) make up the first population, which is called as initialization of the population. Chromosome coding translates the parameter set into gene sequence which could be binary, real value or integer. Fitness function is used to label each individual in the population. The individual who has better performance in fitness function will be given higher credit, and is more likely to be selected to generate offspring. Crossover is how the population generating the offspring, where genes of two selected individual are exchanged. After crossover, bits of the gene sequence could be facing mutation that happens stochastically. Mutation maintains the genetic diversity of current generation to the next one.

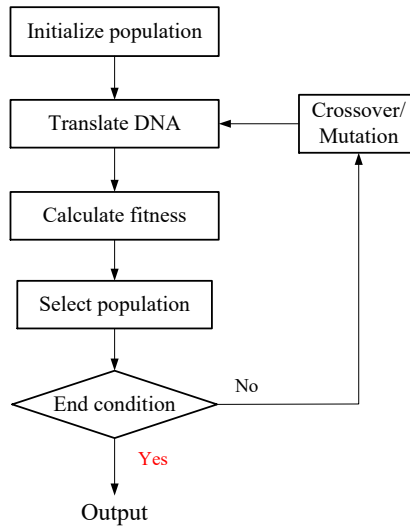


Figure 2-9: General procedures of the genetic algorithm.

Mohamed et al. [91] first applied genetic algorithm to optimize a PEFC stack design by finding the best configuration in terms of number of series, parallel cells and cell surface. It starts with generating the target parameters randomly between upper and lower limits provided by designer. And calculate the fitness value of each individual. The fitness was calculated as the difference between the fuel cell mathematical model and the experimental one. Those how closer to the experimental data ranked higher meaning more likely to be used to generate offspring. After several generations, the optimal model parameters were obtained. Li et al. [92] developed a novel genetic algorithm to optimize the parameter of thermal-model-oriented control law for PEFC stack. The thermal transfer coefficients were estimated by their algorithm, of which the searching time was reduced by improving the global and local searching ability. Nejad et al. [93] employed genetic algorithm to obtain the optimal control parameters of a PEFC, which overcame the improper efficiency of primary parameters in studied problem. The control parameters were adjusted for minimization of the voltage deviations, and then the adjusted

parameters were applied to the operating PEFC. Their model realized an online optimization, decreases the voltage deviation and improved the dynamic response in the fuel cell system.

Kang et al. [94] used a genetic algorithm to identify the hyperparameters of the LSSVM that used to establish a dynamic temperature model for a SOFC. This model is able to capture the temperature dynamics of the SOFC with good accuracy, which benefits from the automatically tuning process of the hyperparameters of the LSSVM and the modeling method itself.

2.3.3 Artificial neural networks

In addition to establishing a black-box model, the artificial neural networks (ANNs) could also be used in parameter estimation. Hatti et al. [95] performed an ANN based static modeling of PEFC, where its critical parameters under different stoichiometric condition at different operating conditions is estimated. Puranik [96] et al. developed a nonlinear auto aggressive model of the PEFC with external inputs based on the neural networks. A recurrent feedback strategy was implemented to yield accurate results. More importantly, polarization curves obtained at different temperature has matched exactly to the real fuel cell characteristics reducing the error substantially. Although the PEFC model developed based on ANN controllers has improved the performance, the immense complexity involved critically questions its suitability and implementation.

2.4 Conclusions and ideas

An overview on advances in the dynamic modeling for the PEFCs was presented in this chapter. The underlying fundamental ideas, general applications, and their strength and weakness are also presented. Different modeling methods have been categorized into three groups according to their methodology, namely white-box models, gray-box models, and black-box models. The differences among the three types of models are listed in Table 2-IV. White-box models provide a deep understanding of the fuel cell system, and can be used beforehand to analysis the fuel cell system. Complex mathematical calculation is often required, and assumptions are made to simplify the models' complexity. Gray-box models are suitable for the system that only small parts of the system remain unknown or few parameters need to be identified. Black-box models are independent to the system priori knowledge with high computation speed. In general, with sufficient data being provided to the black-box model, a high approximation is obtained. The high computational speed characteristic of the black-box models has practical advantages in on-line process control cases.

Table 2-IV: Different modeling methods and their properties [97].

Attribute	Modeling methods		
	White-box	Gray-box	Black-box
Knowledge of process	High	Medium	Low
Computational burden	High	Medium	Low
Data demand	Low	Medium	High
Extrapolation capabilities	High	Medium	Low

The fuel cell's performance in operation is not only affected by its manufacturing and assembling process, but also closely related to its operating conditions and load changes. An accurate and reliable model which has fast response to the various changes during operation and can fast predicting the fuel cell dynamics is necessary. Since the PEFCs system is complex, multivariate and strongly coupled, modeling its characteristic and predicting its performance is difficult. The black-box models simply consider functional relationships between system inputs and system outputs and do not have any physical significance to physical process parameters. The fuel cell dynamic model is built from abstracted parameters. But no knowledge of the process and highly rely on the data are also the disadvantages of black box models compared to white-box models. However, when the requirement is only to capture the dynamics and nonlinearity of the system, then the black box modeling approach is very attractive.

The black-box models introduced in section 2.2 are summarized and compared in Table 2-V.

Table 2-V: Comparison among different black-box modeling methods.

Methods	Characteristics	Pros (•) and cons (◦)
ANNs	Nonlinearity; High flexibility; Weighted connections;	<ul style="list-style-type: none"> • Parallel processing capability; • Represent complex non-linear behavior; • Having fault tolerance; ◦ Unexplained behavior of the network; ◦ Determination of proper network structure; ◦ Local minimum and over-fitting problems
Fuzzy logic	Flexible and easy to implement; Mimic the logic of human thought;	<ul style="list-style-type: none"> • Systems is easy and understandable; • Mostly robust when no precise inputs required; • Deal with the uncertainty in engineering ◦ Not always accurate; ◦ Incapable in pattern recognition; ◦ Setting up is quite a difficult task
SVM	Structure risk minimization; Maximum margin hyperplane; Kernels; Non-linear separable problems; Inequality constraints; Quadratic programming	<ul style="list-style-type: none"> • Tolerance to noise; • Accurate in high dimensional spaces; • Effective when the number of features are larger than training samples; ◦ Larger dataset accompanies with longer computation time; ◦ Poor performance in case of overlapped classes
LSSVM	Structure risk minimization; Statistical learning theorem; Equality constraints; Linear programming	<ul style="list-style-type: none"> • Superior generalization ability; • Computational attractiveness; ◦ Lack of sparseness;

The least squares support vector machine (LSSVM), due to its excellent ability to approximate any nonlinear system is regarded as a solution for nonlinear complex system modeling like the PEFCs. Only a set of linear equations need to be solved in the LSSVM, the training time is largely reduced. The model structure is simple, which is ideal candidate for nonlinear complex system modeling like fuel cells.

Thus, a LSSVM model for fuel cell voltage is established in chapter 3. However, for numerical implementation and applications, the model accuracy, suitability and credibility are always the priority. Then the suitability of the transient model under various working conditions is evaluated in chapter 4, where ideal case is considered. Based on this, the more practical conditions are taken into consideration in chapter 5, in which the oscillation on the cell voltage is included. In order to reach high model accuracy, an optimized transient model, which is based on LSSVM model, is established in chapter 6.

3 A LSSVM model for PEFCs dynamics

This chapter focuses on the dynamic response estimation for the polymer electrolyte fuel cells (PEFCs), which can be used for predicting fuel cell transient voltage output. To overcome the complex nonlinearity, multi-physics coupled and time-varying properties, a transient voltage model is established, which is based on the least squares support vector machine. This chapter is organized as follows: Section 3.1 describes voltage behavior. Section 3.2 introduces basic structure of the least squares support vector machine. The experiments setup is presented in section 3.3. The LSSVM modeling procedures and the model performance are presented in section 3.4 and 3.5, respectively. Section 3.6 draws conclusions.

3.1 Time-varying voltage behavior

Voltage is easy to be measured in the operating PEFCs. Load changes [98], a broken balance inside the fuel cell [99], and fuel cell failures [100] will lead to a change in voltage, which makes the cell voltage an effective tool to measure the performance of the fuel cell. Thus, in order to well monitor the performance of operating fuel cell then achieve good performance, a real-time assessment of the cell voltage, and the establishment of an efficient and reliable model that can predict the PEFCs system output in real-time are necessary.

The transient voltage collected in our test rig is shown in Figure 3-1, where the brown is the current density and the black represents the cell voltage. The current density was increased stepwise from 0.1 A cm^{-2} to its limited current density value 1.2 A cm^{-2} with a step of 0.2 A cm^{-2} . At each current density level, holds on for 180 s. After reach the limited current density value, the current density was decreased stepwise from 1.2 A cm^{-2} to 0.1 A cm^{-2} by 0.2 A cm^{-2} . The change in current density occurs instantly. The experiment ran 2340 s. Despite determined current density is applied to the fuel cell, still, oscillations are caught on the cell voltage, and the oscillated amplitudes vary from different current densities. At low current densities, the oscillations on the cell voltage are minor, but at high current densities, the oscillations are severe. Oxygen starvation, superfluous heat, water accumulation in flow channel and membrane flooding may cause the oscillations in the cell voltage, but cannot fully explain the voltage-current characteristics. A more efficient modeling approach is necessary to address these complexities and contribute to a better solution to model the dynamic behavior of the PEFCs.

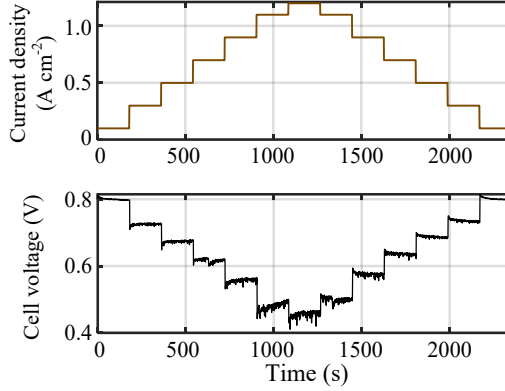


Figure 3-1: Dynamic voltage-current density profiles (Brown curve: current density; Black curve: cell voltage; Operating temperature: 343.15 K; $RH_{an}=100\%$; $RH_{ca} = 100\%$; Active area: 17.46 cm²; $\lambda_{an} = \lambda_{ca} = 2$).

3.2 Least squares support vector machine

The least squares support vector machine (LSSVM) is a black-box model for approximation and can transform the statistical learning theory into practical applications. It constructs the connection between the input and output instead of analyzing the physical phenomenon using analytical methods [101]. LSSVM modeling method is widely applied in various engineering applications because of its high ability to approximate the complex input/output relationship and predict the performance of the system. It is a machine learning technique and based on the statistical learning theory and structural risk minimization principle. By mapping the input data in a primal space into a feature space, the nonlinear relationships in the primal space between the input data and output data are transformed into linear relationships in the feature space. By this method, the complexity of the model's calculation process is somewhat reduced, which is less time-consuming without a computational burden.

The LSSVM method has the following form [82]:

$$y = \omega^T \varphi(x) + b \quad (3-1)$$

where $x \in R^n, x \in R, \varphi(\cdot): R^n \rightarrow R^{n_h}$ is a nonlinear function that maps the input space into a higher dimension feature space. Details of the LSSVM modeling method can be found from Eq. 2-10 to 2-14. By utilizing training data $\{(x_i, y_i), i = 1, 2, \dots, N\}$, and introducing Lagrangian multiplier α_i , the result of the LSSVM method is as follows:

$$\hat{y} = \sum_{i=1}^N \alpha_i K(x, x_i) + b \quad (3-2)$$

$K(x, x_i)$ is the kernel function, and the commonly used kernel functions are listed in Table 2-III. There is no common conclusion for the selection of kernel function. However, the Gaussian radial basis function (RBF) is usually used due to following reasons [102–105]:

- In the absence of expert knowledge about data and domain, its performance is still very good. And only one hyper-parameter needs to be tuned during the training process;
- The value of RBF kernel decreases as the distance between the two feature vectors increase, and its value varies between 0 and 1. It is a similarity measurement representation and it has localized an finite response along the entire space;

The expression of the Gaussian RBF is as following:

$$K(x, x_i) = \exp\left(-\frac{\|x-x_i\|^2}{2\sigma^2}\right) \quad (3-3)$$

here, σ is called width parameter. Then, by using the RBF as kernel function in the LSSVM model, the model's performance highly depends on the regularization term γ and the RBF kernel parameter σ that controls the width of the kernel. The regularization term determines the trade-off between minimizing training errors and minimizing model complexity, is important to increase the generalization performance of LSSVM model. The kernel parameter σ influences directly the number of initial eigenvalues/eigenvectors. Small values of σ yield a large number of regressors, and eventually it can lead to over-fitting. On the other hand, a large value of σ can lead to a reduced number of regressors, making the model more parsimonious, but eventually not so accurate.

However, there are no guidelines for choosing the parameters, but they could be selected through cross-validation, sometimes called rotation estimation [79]. Cross-validation can assess the approximating ability of a statistical analysis to an unknown dataset. It is commonly used in the field, where the goal is prediction, and one wants to estimate the model's predicting ability.

3.2.1 Cross-validation

To establish a model, the dataset is divided into two parts, namely training set and testing set. Suppose X is the universe, and A is a non-void proper subset of X , then $X \setminus A$ is the complementary set of A in the universe X . Hence, dataset A is used in training process and $X \setminus A$ is used in testing process. A is then called as training set and $X \setminus A$ is called as testing set. One should note that only the training set can be used in the training process, and the testing set can only be used to validate the model's performance after the model training process is completed.

There are two forms of cross-validation: exhaustive cross-validation and non-exhaustive cross-validation. Exhaustive cross-validation methods go through all the non-void proper subset A of the universe X . If there are n elements in the universe X , then the selection rule for subset A is $2^n - 2$. The complexity of this method is exponential. In contrast, non-exhaustive cross-validation methods do not consider all possibilities of splitting the universe X .

Leave- p -out cross-validation is an exhaustive cross-validation method. p elements in the universe X are selected in testing set, and the rest $n-p$ elements are included in training set.

According to mathematical theorem, there are $\frac{n!}{(n-p)!p!}$ ways to choose p elements. Based on this, the time complexity of leaving leave- p -out cross-validation is very high. When $p = 1$, it is called as leave-one-out cross-validation, which does not suffer from the intensive computation, as the time complexity is n .

Hold-out method randomly divided into the universe X into two subsets A and $X \setminus A$. A is regarded as training set and $X \setminus A$ as testing set. The size of training set and testing set is arbitrary but the training set should larger than the testing set. The advantage of the hold-out method is that it is simple to carry out, only need to divide the original dataset into two parts. But it is not essentially a cross-validation method, and its accuracy of the validation is highly depended on the original dataset separation.

K-fold cross-validation is a non-exhaustive cross-validation method. The universe X is randomly divided into k subsets. Each subset is equal in size with $|A_1| = |A_2| = \dots = |A_k|$. Now the hold-out method is repeated k times, at each time, $X \setminus A_i$ ($i = 1, 2, \dots, k$) is regarded as training set and used to trained the model, and then A_i is used to test the model. The error estimation is averaged over all k trails to get total effectiveness of the model. As rule of thumb, $k = 5$ or 10 is generally preferred [106]. When $k = n$, it becomes to leave-one-out cross-validation.

3.3 Experimental setup

The LSSVM model's performance will be verified in the PEFCs test cell that was manufactured and assembled at the Forschungszentrum Jülich in Germany. The PEFC test cell has a power of 9 W and an active MEA area of 17.64 cm². It utilizes a Freudenberg gas diffusion layer (GDL), which was loaded with 5% PTFE and coated with an MPL. The flow field consists of three parallel serpentine channels. The end plate was fabricated from stainless steel type 1.4571 (316 Ti) [107,108]. Greenlight Technology's G40 test stand was used to monitor and control the fuel cell, as is shown in Figure 3-2. The test stand allows for the modification of a number of process variables and the collecting of a set of experimental data under different operating conditions. It is also able to change the operating conditions, for example, gas flow rate, temperature and relative humidity. The working environment of the fuel cell required by the user can be well satisfied. The fuel cell's current and voltage are collected by corresponding collectors. A manometer, on the cathode side, is used to measure the pressure drop by calculating the difference between the inlet/outlet pressures. The fuel cell is equipped with four gas flow rate sensors that are used for sensing the inlet and outlet flow rate on both sides during operation. The fuel cell is heated by two heaters inserted on the anode and cathode endplate, respectively. In the meantime, two thermocouples are inserted onto each side and are used to monitor the cell temperature and ensure it is kept at set temperature [107].

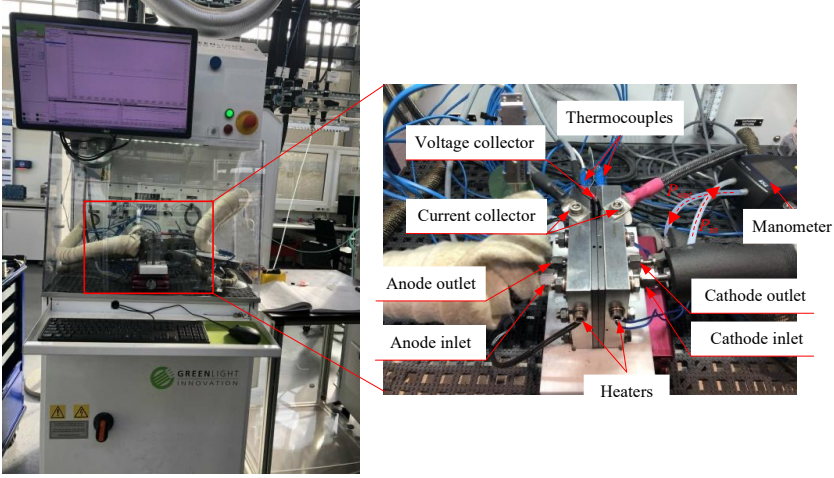


Figure 3-2: Greenlight Technology's G40 test stand and sensors layout.

The test procedures are as following: The starting point of the current density is set at 0.1 A cm^{-2} , and remains at this value for 180 s. Then, the current density is increased in increments of 0.1 A cm^{-2} and remains at the current value for 180 s. These steps are repeated until it attains the limited current density (1.2 A cm^{-2}). It is maintained at this limited value for 180 s, then, the current density is decreased at a rate of 0.1 A cm^{-2} by the current density measures 0.1 A cm^{-2} . Repeat this process and obtain the asymmetrical profile displayed in Figure 3-3. The experimental data were collected with a sampling interval of $\Delta t = 1 \text{ s}$, with the experiment carried out for 4525 seconds. Pure hydrogen is used as fuel and air used oxidant. During the operation, the cell operating temperature was set to 343.15 K and the reactant gases' relative humidity (RH) were set to 90%, and the stoichiometry of hydrogen (λ_{an}) and air (λ_{ca}) were set to 2.

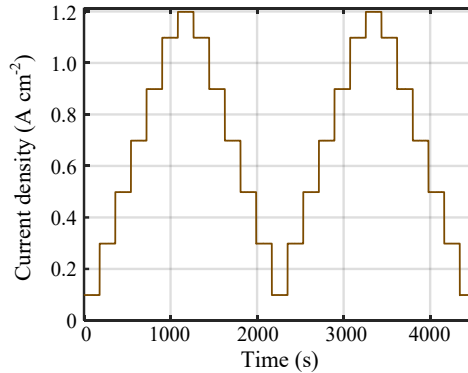


Figure 3-3: Current density profile. (Limited current density: 1.2 A cm^{-2} ; Ramp values: 0.1 A cm^{-2} ; Sampling interval $\Delta t = 1 \text{ s}$)

3.3.1 Dataset preparation

With the experimental data collected from the test rig, the LSSVM modeling method is used to determine the relationship between the inputs of the fuel cell system and the output voltage. The experimental data were collected with constant sampling interval (Δt). Inlet reactant gases pressure (p_{H_2} and p_{air}) and flow rate (\dot{n}_{H_2} and \dot{n}_{air}), cell current density (i) constitute the LSSVM model input, as $u(t) = [i, p_{H_2}, p_{air}, \dot{n}_{H_2}, \dot{n}_{air}]$. The cell voltage (v (V)) is the LSSVM model output, as $y(t) = v$ (V). The inlet pressures of both sides are shown in Figure 3-4 and Figure 3-5 respectively. Cell voltage is shown in Figure 3-6.

Considering the effects of the adjacent time points, the input of the LSSVM model consists not only of the present variables, but also includes previous data, which is expressed as follows:

$$U(t) = [u(t), u(t - \Delta t), \dots, u(t - \tau \Delta t)] \quad (3-4)$$

here, τ is the number of adjacent time point and in this work $\tau = 3$.

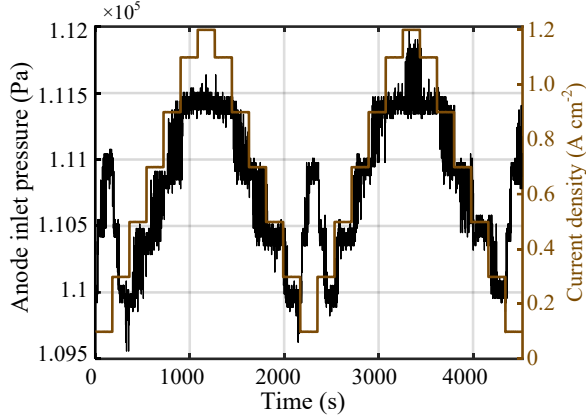


Figure 3-4: Anode inlet pressure: hydrogen is fueled into the anode side (Stoichiometry of both side is set as 2; Relative humidity of both sides is RH = 90%; Cell temperature is T = 343.15 K).

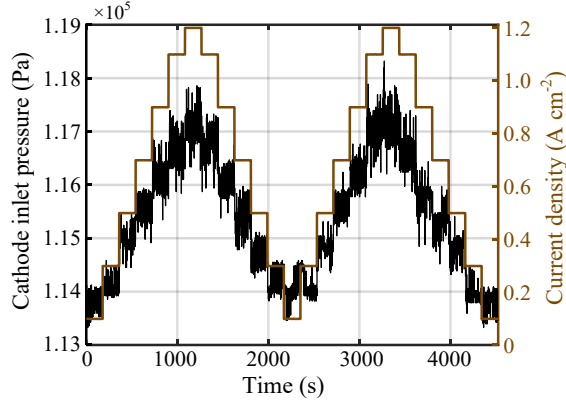


Figure 3-5: Cathode inlet pressure: air is delivered into the cathode side (Stoichiometry of both side is set as 2; Relative humidity of both sides is RH = 90%; Cell temperature is $T = 343.15$ K).

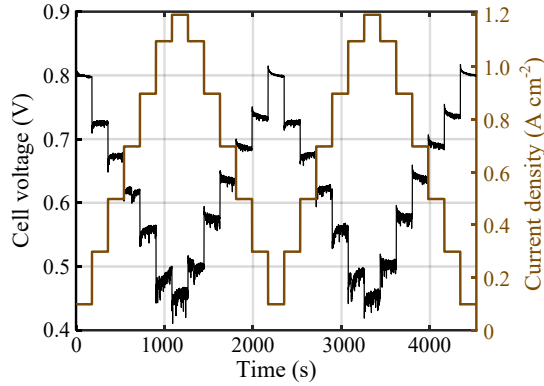


Figure 3-6: Output of the fuel cell: black line is the cell voltage profile and brown line is the current density profile (Stoichiometry of both side is set as 2; Relative humidity of both sides is RH = 90%; Cell temperature is $T = 343.15$ K).

Before the data are used to train the LSSVM model, each data point was normalized to the range $[0, 1]$. The goal of normalization is to change the values of different features in the input dataset to a common scale, without distorting differences in the ranges of values. If the scales of different features are widely varied, the feature with large varying range would have dominating influence on the result. And normalization can eliminate such influence. Min-max normalization is used to scale the input data, and its expression is as following:

$$x' = \frac{x - x_{min}}{x_{max} - x_{min}} \quad (3-5)$$

here, x is the target data, x_{min} and x_{max} the minimum and the maximum value of x , and x' is the normalized result with range $[0,1]$. In this case, $U(t)$ and $y(t)$ will be normalized, the normalized data then become $U'(t)$ and $y'(t)$.

The workflow of how to establish the LSSVM model is presented in Appendix A.1.

3.4 LSSVM model

The normalized data were randomly separated into training data and testing data at a ratio of 4:1, as shown in Figure 3-7. The black dots in the figure represent the training data $\{U'_{train}, y'_{train}\}$, and the red dots represent the testing data $\{U'_{test}, y'_{test}\}$. The training data are used to train and determine the model structure. Once the model has been trained, it is still not completely sure that the model is going to work well on data that has not been seen by the model before. In other words, whether the trained model has the desired accuracy and performance in real application remains unclear. Thus, the testing data unseen by the trained model are used to validate the LSSVM model's performance to confirm if the trained model is eligible for further application to modeling and predicting. The necessity of the testing step is: testing the model's performance with data that unseen by the trained model. A combination of the modeling results on both the training data and testing data is used to evaluate the overall performance of the LSSVM model. If the modeling error is small or is acceptable by the modeling requirements, then the LSSVM model is determined; otherwise, the model should be retrained.

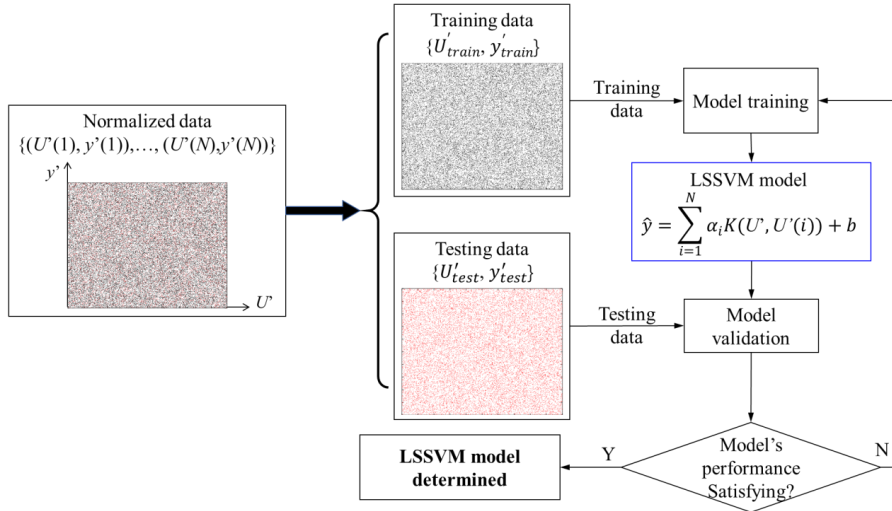


Figure 3-7: LSSVM determination with training and testing data (Black dots: the training data; Red dots: the testing data).

In this work, as RBF function was selected as kernel function, there are two internal parameters $\{\gamma, \sigma\}$ need to be pre-determined before training and testing the model. The hold-out method is repeated with different combination of the internal parameters that the regularization term γ ranges from $e^{0.1}$ to e^{10} , and the kernel parameter ranges from e^{-1} to e^2 .

The model's performance is measured by three indices:

$$e = |v - \hat{v}| \quad (3-6)$$

$$\text{RMSE} = \sqrt{\frac{1}{N} \sum_{i=1}^N (v(t_i) - \hat{v}(t_i))^2} \quad (3-7)$$

$$R^2 = 1 - \frac{\sum_{i=1}^N (v(t_i) - \hat{v}(t_i))^2}{\sum_{i=1}^N (v(t_i) - \bar{v}(t_i))^2} \quad (3-8)$$

where v is the collected cell voltage from the test rig and \hat{v} the LSSVM model output voltage, e the absolute error $e = [e_1, e_2, \dots, e_N]^T$ and N the number of the data points collected from the fuel cell system, RMSE the root mean square error, R^2 the coefficient of determination. RMSE measures how concentrated the predicted data are around the experimental data, while R^2 represents how many predicted data fall within the results and is a fraction that ranges from 0 to 1.

This is reported with respect to model performance later in this paper. Absolute error (e (V)), root mean square error (RMSE) and coefficient of determination (R^2) are used to measure the model performance. For the absolute error and RMSE, a smaller value indicates better model's performance, while for the coefficient of determination, a higher coefficient results in a better approximation of the model.

The overall modeling results, including training and testing results, of the LSSVM model with various combinations of the internal parameters are listed in Table 3-I, where the coefficient of determination is used. Higher value of the coefficient of determination means better modeling performance. From the table it can be found that the best parameters for the LSSVM model are $\{\gamma, \sigma\} = \{1, 403\}$, which results in a coefficient of determination of 0.9984.

Table 3-I: Results of cross-validation (hold-out method): Coefficient of determination is used to evaluate the results: higher value represents better results.

		Kernel parameter σ							
		e^{-1}	$e^{-0.1}$	$e^{-0.01}$	e^0	$e^{0.01}$	$e^{0.1}$	e^1	e^2
Regularization term γ	$e^{0.1}$	0.9924	0.9932	0.9929	0.9932	0.9932	0.9933	0.9886	0.0252
	e^1	0.9952	0.9958	0.9955	0.9954	0.9953	0.9956	0.9912	0.0609
	e^2	0.9964	0.9969	0.9965	0.9971	0.9971	0.9970	0.9942	0.1657
	e^3	0.9977	0.9978	0.9977	0.9977	0.9976	0.9977	0.9958	0.3408
	e^4	0.9977	0.9981	0.9981	0.9979	0.9979	0.9981	0.9967	0.6596
	e^5	0.9984	0.9982	0.9983	0.9982	0.9983	0.9982	0.9971	0.8108
	e^6	0.9982	0.9978	0.9981	0.9984	0.9983	0.9983	0.9975	0.9188
	e^7	0.9979	0.9981	0.9978	0.9981	0.9980	0.9980	0.9977	0.9599
	e^8	0.9975	0.9982	0.9974	0.9982	0.9978	0.9979	0.9979	0.9751
	e^9	0.9961	0.9971	0.9972	0.9973	0.9971	0.9971	0.9980	0.9804
	e^{10}	0.9940	0.9959	0.9954	0.9947	0.9968	0.9950	0.9981	0.9823

3.4.1 LSSVM performance

With the optimal internal parameters $\{\gamma, \sigma\} = \{1, 403\}$ determined in last section, the LSSVM model (Eq. 3-2) is established. The model's output and absolute error are shown in Figure 3-8, where the LSSVM model outcome \hat{v} (red line) of the fuel cell's voltage is compared against the measured data v (black line). The absolute error is the difference between these two datasets, and is also shown in Figure 3-8b. It can be seen that at high current density, which results in a low cell voltage, the error tends to be larger. At this current density level, the cell voltage behaves more unstably due to water accumulation inside the fuel cell, which introduces a high degree of nonlinearity to the system. The correlation between the model output and experimental data is shown in Figure 3-9. The black dots represent the voltages of the LSSVM model output against the experimental data, while the red line is the ideal level and where the black dots should be located. From Figure 3-1 can be found that lower current density results higher cell voltage. Then, it can be concluded from Figure 3-9 that the LSSVM model shows a satisfactory result at a low current density (high cell voltage), with most of the black dots falling on part of the red line (ideal case). However, at high current densities (near the left side of Figure 3-9), the black points deviate from the red line, which means poor model accuracy. This phenomenon corresponds to the result shown in Figure 3-8. RMSE of the modeling results is 0.0056, and coefficient of determination is 0.9974, which demonstrate an overall good model performance of the LSSVM model.

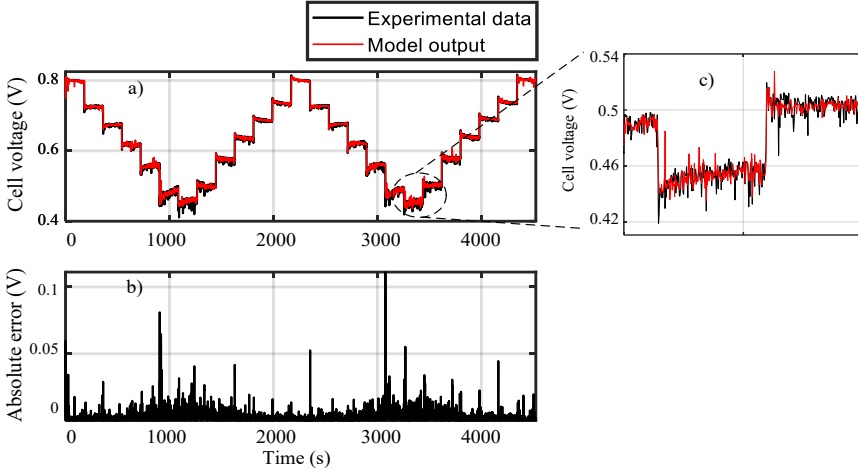


Figure 3-8: LSSVM model results: a) the model output against the experimental data; b) the absolute error; and c) zoomed region.

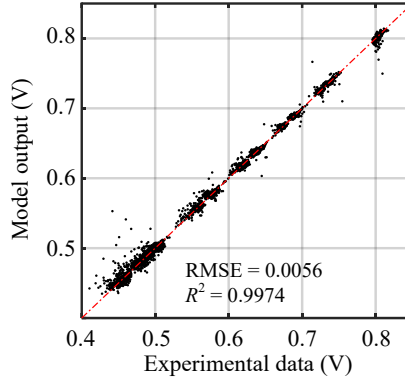


Figure 3-9: Correlation between the model's output and experimental data.

3.5 Conclusions

In this chapter, a transient voltage model was established for the voltage transient behaviors in PEFCs. The model is based on least squares support vector machine (LSSVM). The time-varying voltage was good estimated by the model. The LSSVM model's accuracy was validated by comparing with the experimental data collected in our fuel cell test rig.

A low root mean squares error ($RMSE = 0.0056$) and high coefficient of determination ($R^2 = 0.9974$) demonstrates that the LSSVM model successfully predicted the voltage dynamic behavior. However, when examining the prediction of the LSSVM model to the experimental data, the results showed that at low current densities the LSSVM model performs better compared to those of a high current density. It is because that at high current densities, the fuel cell system is more inclined to an unstable, as oxidant starvation and flooding is more likely to

occur in high current density levels, thus the voltage exhibits a more severe oscillation and abnormality. In addition, the model's performance at each current density ramp is less efficient than stable current densities, as sharp increases of absolute error in each ramp are always found.

Despite an overall good model accuracy was achieved by the LSSVM model, the difference of modeling performance at different loads is worthy of attention and needs to be clarified. Thus, the credibility of the LSSVM model under different load demand (various current density changes) will be further discussed.

4 Analysis of the suitability of the LSSVM model under ideal cases

Results in this chapter has been published in ‘Applied Energy’⁶. The efficiency of the least squares support vector machine (LSSVM) model in modeling transient behavior of the polymer electrolyte fuel cells has been proven in chapter 3. The idea of the next two chapters is to quantify the accuracy of the LSSVM model under different load changes, and explore the limitation of the LSSVM model. In this chapter, and ideal case is considered, in which an idealized white-box model is used to provide the data for the LSSVM model to carry out this research. The next chapter will introduce the oscillation on the cell voltage to the white-box model, in which the LSSVM performance under oscillated cases will be investigated. Methodology is introduced in section 4.1. Details of the idealized white-box model are explained in section 4.2. Artificial data are explained in section 4.3. Factors affecting the model’s performance are introduced in section 4.4. The discussion on the accuracy and limitation of the LSSVM model can be found in section 4.5. And section 4.6 draws the conclusions.

4.1 Methodology

Although the LSSVM model has been proven to be good at approximating the fuel cell dynamic behaviors, but different modeling accuracies are caught at different current density levels. Thus, the accuracy of the LSSVM model under different loads should be investigated.

To carry out this investigation, the LSSVM model should be examined and tested under various load changes. Constrained by the operating specifications of the test rig, load changes applied to the fuel cell system are restricted. Besides, experimental uncertainties, such as misoperation, will result in bad effects, for example, shortcut connections of the equipment that contributes to inaccurate collected information. Thus, an idealized white-box model that based on the mechanism of the fuel cell system is used, and generates data. These data are called as artificial data and used as alternative of the experimental data.

With the help of bringing in the idea of artificial data, the investigation on the LSSVM model includes following steps: various load changes are considered in a white-box model, and corresponding artificial data are generated; then the artificial data and their operating conditions are forwarded to the LSSVM model; in the LSSVM model, the fuel cell dynamics are modelled and predicted; the LSSVM model’s results under different operating conditions are integrated, analyzed and summarized in combination with load change behaviors; after that, the accuracy

⁶ Zou W, Froning D, Shi Y, Lehnert W. A least-squares support vector machine method for modeling transient voltage in polymer electrolyte fuel cells. Appl Energy 2020;271.

and limitation of the LSSVM model are further discussed. Framework of the methodology is shown in Figure 4-1 and corresponding workflow can be found in Appendix A.2.

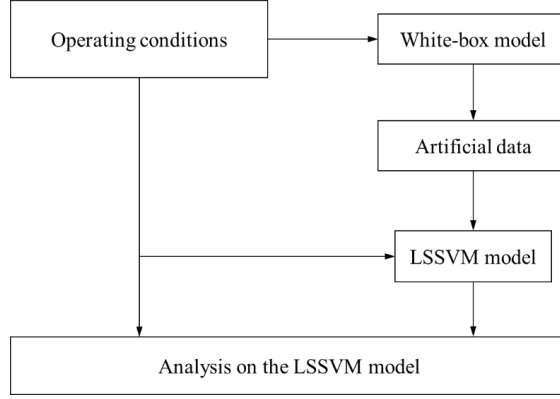


Figure 4-1: Framework of the methodology. (The LSSVM model in this chapter is the same as in the previous chapter).

4.2 White-box model

The establishment of an idealized white-box model is the first step to carry out the investigation on the accuracy of the LSSVM model, by which the artificial data are generated. A simplified nonlinear dynamic white-box model for PEFCs is developed with a set of assumptions:

- The system is isothermal and the temperature throughout the fuel cell is assumed to be constant;
- The relative humidity can be well controlled maintaining at set value, and liquid water is perfectly managed and the water-flooding effects are well controlled;
- A continuous supply of reactants is fed to the fuel cell to allow operation at a sufficiently high flow rate;
- Pure hydrogen (>99.99%) is fueled to anode side of the fuel cell. The air is uniformly mixed with oxygen and nitrogen by a ratio of 21:79 and fueled to the cathode side. The reactants are uniformly saturated with vapor;
- Ideal and uniformly distributed gases;
- Constant pressures in the fuel cell gas flow channels.

The modeling concept of the white-box model is shown in Figure 4-2, in which voltage, anode, cathode and membrane modules are included. The ideal gas law and mass balance law are used here. All of the gases are assumed as ideal gases, and the liquid water is assumed to not leave the cell. In Figure 4-2, \dot{m}_{H_2} and \dot{m}_{air} are the flow rates of hydrogen and air respectively ($g\ s^{-1}$); T_{an} and T_{ca} are the temperature of both sides (K); $I(t)$ is the current of the cell (A); $p_{an,in}$ and $p_{ca,in}$ are the inlet gas pressures of both sides (Pa); ϕ_{an} and ϕ_{ca} are the

relative humidity of anode and cathode respectively; $\dot{m}_{v,mem}$ is the water transport ratio through membrane (g s^{-1}) and the positive direction here is assumed from cathode to anode; $p_{v,an}$ and $p_{v,ca}$ are the partial pressure of water vapor of both sides (Pa); p_{H_2} and p_{O_2} are the partial pressure of hydrogen and oxygen respectively (Pa); $v(t)$ is the cell voltage (V).

Details of each module and relationship between each module are introduced in Appendix A.3 (page: 115).

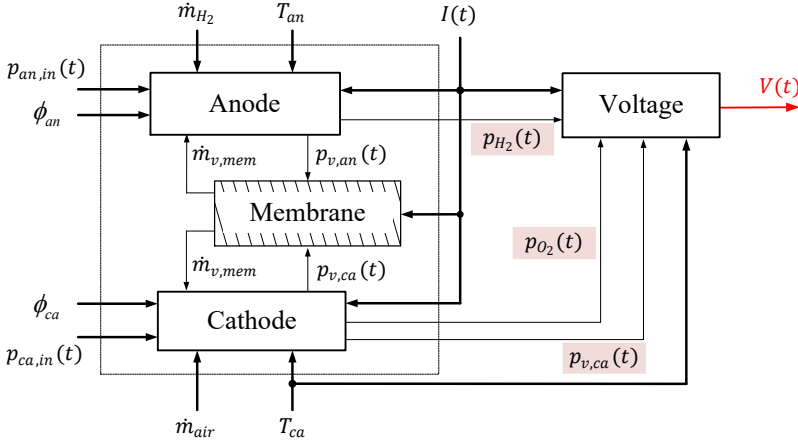


Figure 4-2: Configuration of the fuel cell system simulation (Four modules are included: voltage, anode, cathode and membrane module) [108].

By integrating the anode, cathode and membrane module, the white-box model for PEFCs dynamic is then constructed. The white-box model that followed the physical and electrochemical law of the fuel cell was simulated in a Matlab/Simulink environment, and the schematic of the white-box model is presented in Figure 4-3. The reactant gases are humidified and the relative humidity of both sides is 100%. The stoichiometry of anode and cathode side is set as 2. The flow rates of both sides are changing in the simulation as constant stoichiometry of both sides is used. The parameters used in the white-box model are listed in Table 4-I and the operating conditions are listed in Table 4-II. A Nafion membrane is considered [109] in this simulation.

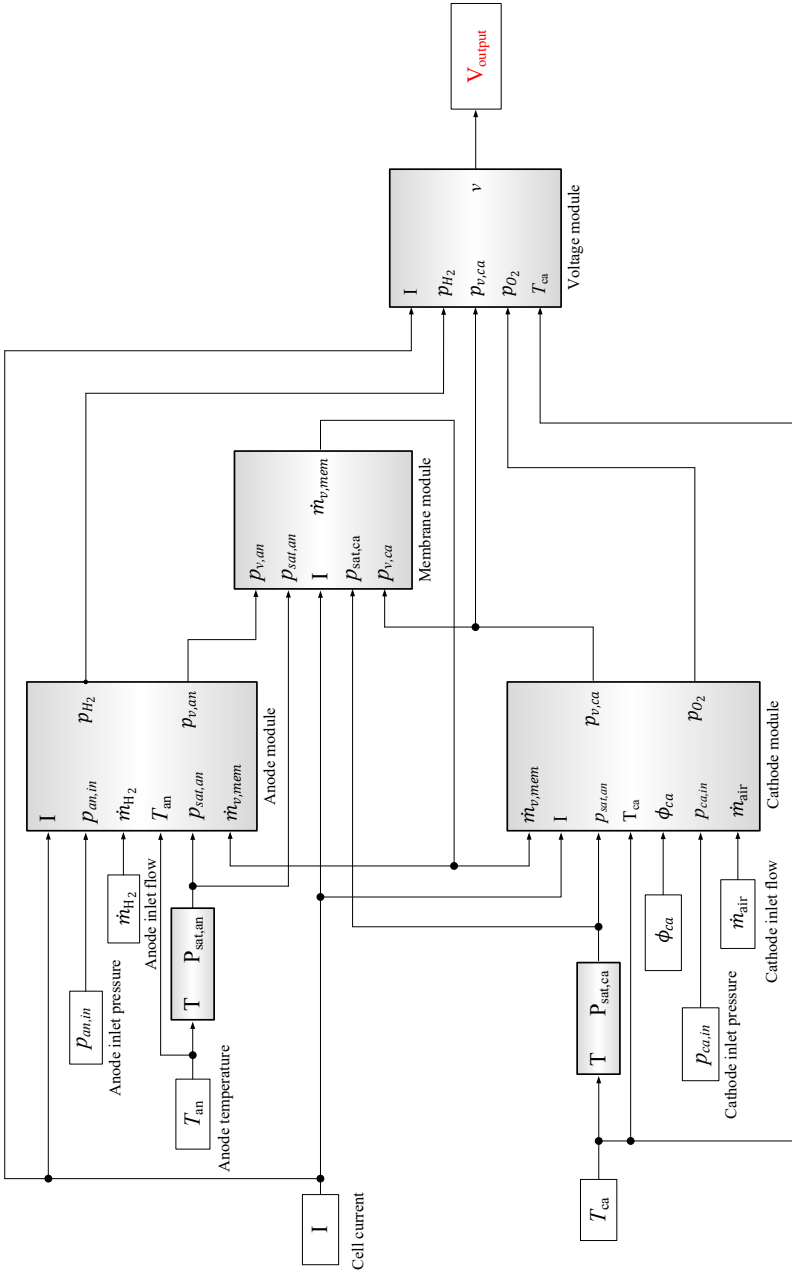


Figure 4-3: Schematic of a PEMFC system (Anode module: section A.3.2; Cathode module: section A.3.3; Membrane module: section A.3.4; Voltage module: A.3.1; Parameters are listed in Table 4-1 and Table 4-II) [108].

Table 4-I: Parameters used in the white-box model [107–109].

Parameter	Value
L (m)	178×10^{-6}
A (m ²)	1.746×10^{-3}
i_{max} (A cm ⁻²)	1.22
V_{an} (m ³)	10^{-6}
V_{ca} (m ³)	10^{-6}
$\rho_{m,dry}$ (kg m ⁻³)	20
$M_{m,dry}$ (kg mol ⁻¹)	1.1

Table 4-II: Operating conditions [108].

Anode	Anode reactant	Hydrogen
	λ_{an}	2.0
	Temperature (T_{an})	343.15 K
	Relative humidity	100%
Cathode	Cathode reactant	Air
	λ_{ca}	2.0
	Temperature (T_{ca})	343.15 K
	Relative humidity	100%

In order to validate the efficiency of the white-box model, a same operating condition was also applied in our test rig (Figure 3-2) to obtain the experimental data. The experiments were carried out in the fuel cell test rig that was manufactured and assembled at Forschungszentrum Jülich, details can be found in section 3.3.

The artificial cell voltage against the real cell voltage collected from the experiment is shown in Figure 4-4. The load change profile is shown at the top of Figure 4-4. With this load, the cell voltage collected from the test station is the black line in Figure 4-4, and the cell voltage calculated by the white-box model is marked as green line in Figure 4-4. Relative error is used here to validate the model's efficiency, as following:

$$\varepsilon = \frac{|v - \hat{v}|}{v} \times 100\% \quad (4-1)$$

here, v is the cell voltage (V) collected from the test station (black in Figure 4-4), \hat{v} is the white-box model output ((V), green line in Figure 4-4).

It can be seen from Figure 4-4 that the artificial data approximates the experimental data very well with small difference, which means the white-box model is able to catch the fuel cell dynamics. Also, the relative error in Figure 4-5 indicates a good model performance with the maximum absolute is lower than 10%. Thus, the artificial data is eligible to be used as an alternative to the experimental data.

4 Analysis of the suitability of the LSSVM model under ideal cases

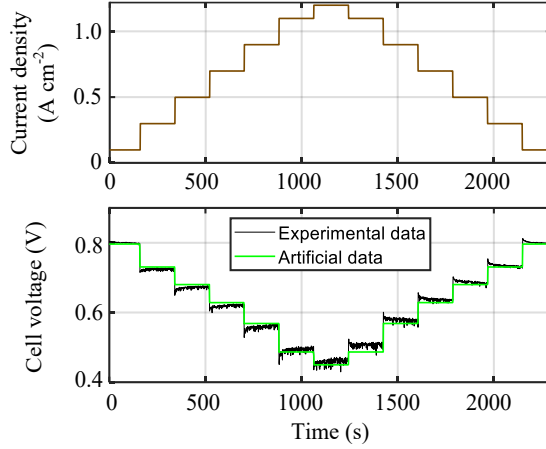


Figure 4-4: Artificial data approximates against the experimental data (Brown line: current density; Black line: voltage collected from the test station; Green line: cell voltage calculated by the white-box model). Details can be found in section A.3.

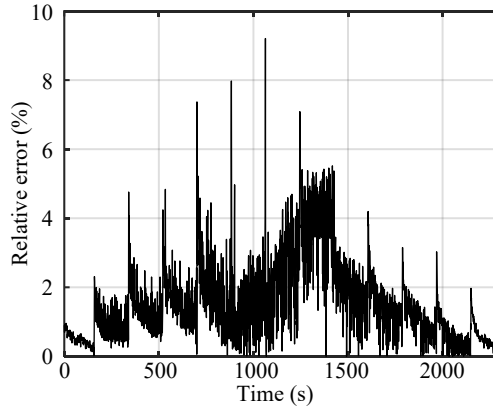


Figure 4-5: Relative error of the white-box model (Eq.4-1).

4.3 Artificial data

As an alternative to experimental data, artificial data is able to provide data of fuel cells under sharp and extreme load changes, which are prohibited by the fuel cells test rig and harmful to the fuel cells. Also, employing artificial data has an advantage over experimental data because it is timesaving. The load changes are constructed through load ramp time and ramp value. Ramp time indicates how fast the load is changing and ramp value represents the amplitude of the load change. Twelve ramp times are considered, namely $t_{in} = 1 \text{ s}, 5 \text{ s}, 10 \text{ s}, 20 \text{ s}, 30 \text{ s}, 60 \text{ s}, 90 \text{ s}, 120 \text{ s}, 150 \text{ s}, 180 \text{ s}, 210 \text{ s}$ and 240 s . Ten values of the ramp time Δt , also referred as current density change are employed and listed in Table 4-III [108]. Besides, considering the LSSVM model is a data-driven method which is highly rely on the data that used in the model,

four sampling intervals are chosen ($\Delta t = 1$ s, 3 s, 5 s and 8 s) in order to illustrate the system's setup on the performance of the LSSVM method.

Table 4-III: Ramp values: Amplitude of current density change.

Case	1	2	3	4	5	6	7	8	9	10
Δi (A cm ⁻²)	0.2	0.3	0.4	0.5	0.6	0.7	0.8	0.9	1.0	1.1

Sampling interval

Dynamic behavior and operating information of the operating fuel cell are collected and preserved by the fuel cell system with a pre-set sampling interval. The sampling interval should be adjusted according to different dynamic properties of the fuel cell during operation and different research purposes and accuracy. A high frequency sampling procedure provides detailed information on the system but always accompanies by storage issues, as a large storage space is required. Moreover, it also brings about a processing issue when analyzing the sizeable amount of data, as more computation time is required for the analysis, with a corresponding increase in the control system's price. Thus, the tradeoff between detailed system information and economics should be taken into account.

Using the white-box model to generate artificial data, one of the current density ramp profiles applied to the white-box model is shown in Figure 4-6. Initially, the current density is set to 0.1 A cm⁻² and remains for 180 s. The current density is then increased from 0.1 A cm⁻² to 0.5 A cm⁻² in 60 s. The ramp time t_{in} and ramp value Δi in Figure 4-6 remain constant ($t_{in} = 60$ s, $\Delta i = 0.4$ A cm⁻²). When the current density reaches its limited value (1.19 A cm⁻²), the current density is progressively decreased until it equals 0.1 A cm⁻². Increasing the current from 0.1 A cm⁻² to 1.19 A cm⁻² then decreasing it from 1.19 A cm⁻² to 0.1 A cm⁻² is called as one loop. Repeating the loop until the entire process covers a period of 5400 s.

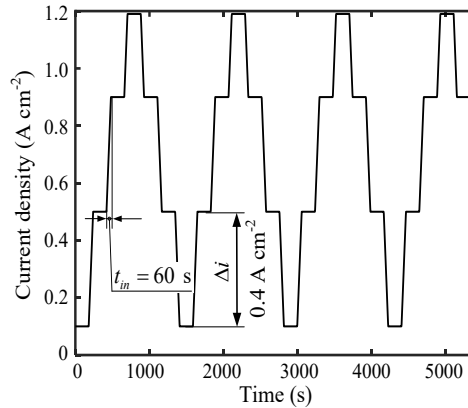


Figure 4-6: Current density profile with ramp value $\Delta i = 0.4$ A cm⁻², ramp time $t_{in} = 60$ s. The artificial data was collected with a sampling interval of $\Delta t = 1$ s (Operating condition is listed in Table 4-II).

4 Analysis of the suitability of the LSSVM model under ideal cases

An intensive sampling procedure provides detailed information on the system and enables a high degree of accuracy. However, it is always accompanied by storage and processing issues when dealing with the sizeable amounts of data, as a large storage space and more computation time are required. For example, if we use sampling interval $\Delta t = 1$ s to collect and store the data, we will obtain 5400 data points, while a sampling interval of $\Delta t = 5$ s to collect and store the data will result in 1080 data points. With a small value of sampling interval, large storage is required. Moreover, collecting data with small value of sampling interval also brings about a heavy computational burden when analyzing these data, as more time is required for the analysis, with a corresponding increase in the control system's price. Thus, the tradeoff between model accuracy and economics should be taken into account.

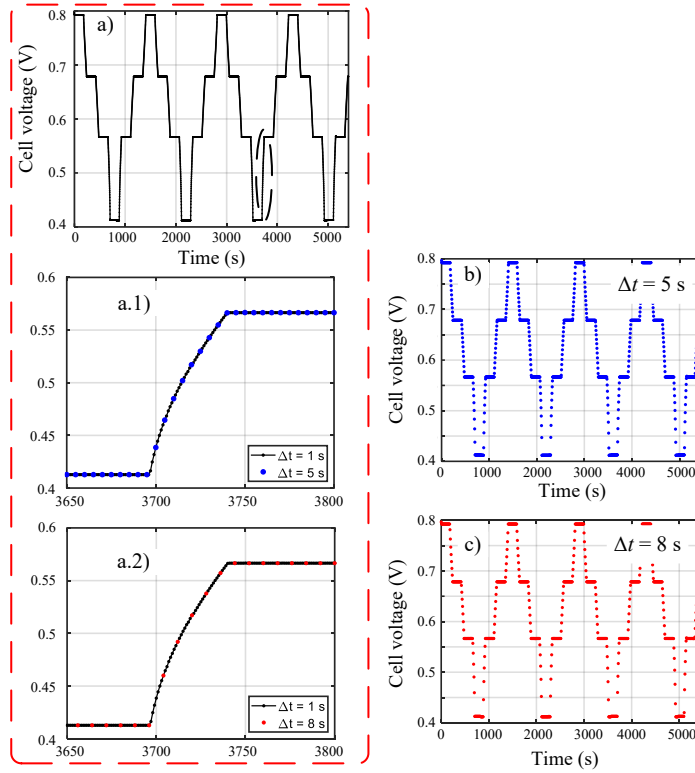


Figure 4-7: Artificial data collection with different intervals: a) $\Delta t = 1$ s with zoomed region marked; b) $\Delta t = 3$ s; and c) $\Delta t = 8$ s; a.1) zoomed region, 1 s and 3 s; a.2) zoomed region, 1 s and 8 s (Operating condition is listed in Table 4-II).

Figure 4-7 illustrates how data are collected with different sampling intervals. The black line in Figure 4-7a is the cell voltage generated by the white-box model with current density profile showed in Figure 4-6, in which the artificial data is preserved with the sampling interval $\Delta t = 1$

s. Another two intervals $\Delta t = 5$ s (blue dots in Figure 4-7b) and $\Delta t = 8$ s (red dots in Figure 4-7c) are selected to show the differences created by the sampling. In Figure 4-7a, a region spanning 3650 to 3800 s is marked and zoomed out in Figure 4-7a.1 and a.2. The blue dots (Figure 4-7a.1) and red dots (Figure 4-7a.2) represent the data collected at sampling intervals $\Delta t = 5$ s and $\Delta t = 8$ s, respectively. It should be noted that with large value of sampling interval, the amount of data is significantly reduced.

Ramp time

Two load change profiles with ramp time $t_{in} = 60$ s and $t_{in} = 180$ s and their corresponding output voltages are shown in Figure 4-8 and Figure 4-9, respectively. At the beginning of both processes, the current density was set to 0.1 A cm^{-2} and remained so for 180 s, at which point it was increased by $\Delta i = 0.2 \text{ A cm}^{-2}$. In Figure 4-8, the increase takes 60 s, and in Figure 4-9, the increase takes 180 s. This process was repeated until the current density reached to 1.19 A cm^{-2} . After that, the decrease in current density continued at the same decrement of $\Delta i = 0.2 \text{ A cm}^{-2}$ at 60 s in Figure 4-8 and at 180 s in Figure 4-9, step by step, until it reached 0.1 A cm^{-2} , with each process lasting 5400 s [125].

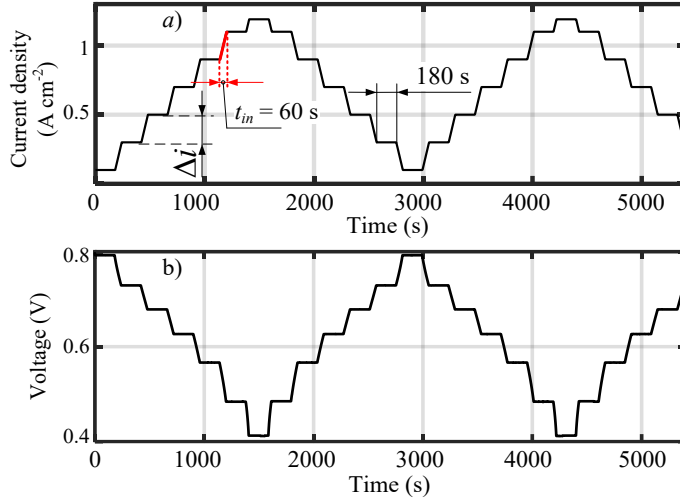


Figure 4-8: Artificial data with ramp value $\Delta i = 0.2 \text{ A cm}^{-2}$, ramp time $t_{in} = 60$ s: a. current density; b. cell voltage (Operating condition is listed in Table 4-II).

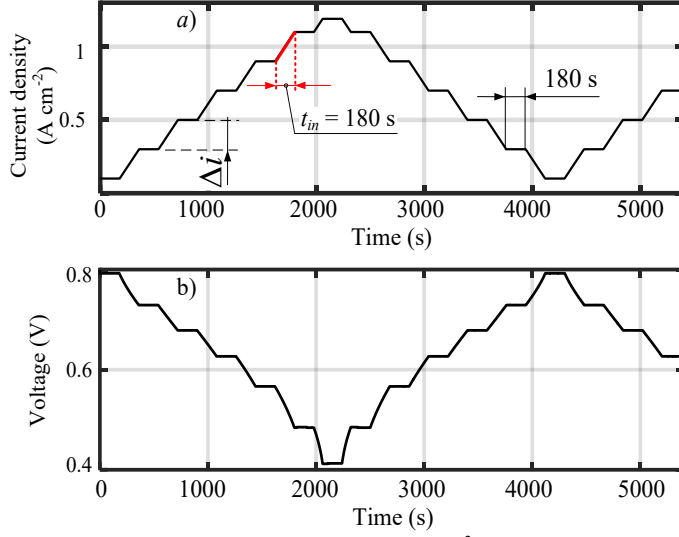


Figure 4-9: Artificial data with ramp value $\Delta i = 0.2$ A cm⁻², ramp time $t_{in} = 180$ s: a. current density; b. cell voltage (Operating condition is listed in Table 4-II).

Ramp value

Two load change profiles with ramp value $\Delta i = 0.3$ A cm⁻² and $\Delta i = 0.5$ A cm⁻² are shown in Figure 4-10 and Figure 4-11, respectively. The ramp time for both cases is $t_{in} = 60$ s. At the beginning of both processes, the current density was set to 0.1 A cm⁻² and remained so for 180 s, at which point it was increased by $\Delta i = 0.2$ A cm⁻² in Figure 4-10 and by $\Delta i = 0.5$ A cm⁻² in Figure 4-11. Both increases take 60 s. This process was repeated until the current density reached to 1.19 A cm⁻². After that, the decrease in current density continued at the same decrease time 60 s with decrement of $\Delta i = 0.2$ A cm⁻² in Figure 4-10 and of $\Delta i = 0.5$ A cm⁻² in Figure 4-11, step by step, until it reached 0.1 A cm⁻², with each process lasting 5400 s. The voltage profiles of both cases are also showed in Figure 4-10 and Figure 4-11, respectively.

As four sampling intervals, twelve ramp times and ten ramp values were considered, 480 sets of artificial data were then obtained.

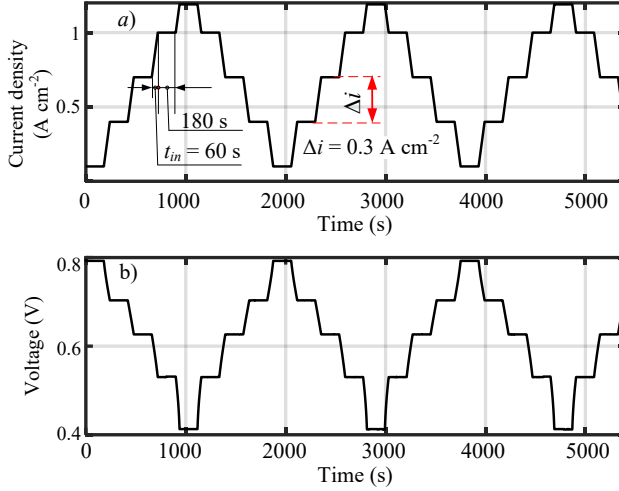


Figure 4-10: Artificial data with ramp value $\Delta i = 0.3$ A cm⁻², ramp time $t_{in} = 60$ s (a. current density; b. cell voltage).

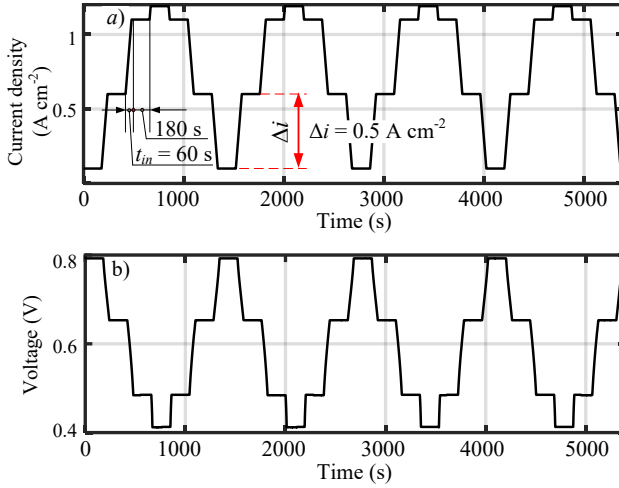


Figure 4-11: Artificial data with ramp value $\Delta i = 0.5$ A cm⁻², ramp time $t_{in} = 60$ s (a. current density; b. cell voltage).

4.4 The LSSVM model performance

The LSSVM model performances under different load changes with different sampling intervals are discussed. Details of the LSSVM model were introduced in section 3.4.

4.4.1 Sampling interval

Absolute error is used to compare the impacts of different sampling intervals on the LSSVM model's performance, four sampling intervals are considered ($\Delta t = 1$ s, 3 s, 5 s, 8 s). The modeling results at sampling intervals $\Delta t = 3$ s and $\Delta t = 8$ s are shown in Figure 4-12 and Figure

4 Analysis of the suitability of the LSSVM model under ideal cases

4-13 under load changes profiles ($t_{in} = 60$ s and $\Delta i = 0.4$ A cm⁻²), respectively. The black dots on the left-hand diagrams show the collected data at each sampling interval, while the red dots are the model output. At sampling interval $\Delta t = 3$ s, the maximum absolute error is around 0.08 V, with an average of 0.04 V, but with $\Delta t = 8$ s, this value is about 0.12 V at an average of 0.09 V. It is clear that the model's accuracy when using intensive sampling datasets is superior to that of a sparse sampling dataset.

In Figure 4-12 and Figure 4-13, it can be seen that the changes in voltage at high current density are larger than those at low current density. In both figures, the absolute error (top right in Figure 4-12 and Figure 4-13) increases sharply at each ramp. The absolute errors are also larger at high current density than at low current density (e.g., $i > 0.8$ A cm⁻²). At a low current density with high cell voltage, the absolute error is around 0.04 V, but at high current density it becomes 0.07-0.085 V. These behavior could be explained by the nature of the data-driven methods, of which dependence on the collected data makes the LSSVM model sensitive to data fluctuation, as the collected data, when high current density is applied, is obviously sparser than that of at low current density; see Figure 4-12 and Figure 4-13. In addition, at high current density, i.e. that which exceeds 0.8 A cm⁻², the absolute error at the up-ramp (the red diamonds in Figure 4-12 and Figure 4-13) is larger than that at the down-ramp (blue diamonds in Figure 4-12 and Figure 4-13). When comparing the up-ramp with the down-ramp in the load range, the data from the up-ramp is first processed by the model, followed by the down-ramp process. This means that the collected data in the up-ramp changes are new to the model, and during the up-ramp this kind of data has been well-processed by the model; then, at the near down-ramp change, the model can effectively deal with the collected data, as this kind of data had already been incorporated into it. After the current density reaches the minimum value, another round of changing the current density process commences. When the fuel cell system reaches a high current density the second time, the absolute error is still large. This is because if the online property of the model is used, only a subset of recent data is processed in it.

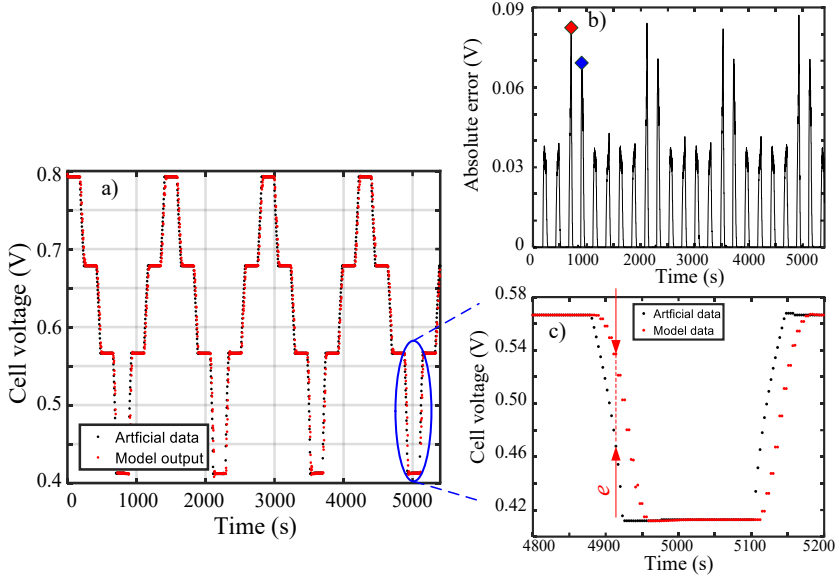


Figure 4-12: The LSSVM model performance with data preserved with sampling interval $\Delta t = 3$ s: a) Model output approximated against artificial data; b) absolute error (Eq. 3-6); c) zoomed region [108].

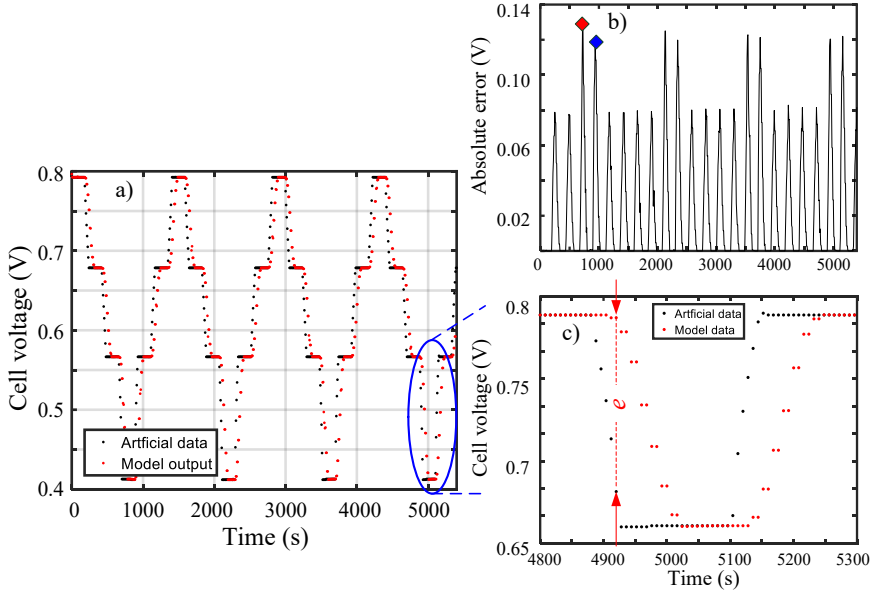


Figure 4-13: The LSSVM model performance with data preserved with sampling interval $\Delta t = 3$ s: a) Model output approximated against artificial data; b) absolute error (Eq. 3-6); c) zoomed region [108].

The integrated error (V s) and the coefficient of determination (Eq. 3-8) are used to compare the LSSVM model's performance. The integrated error is defined as:

$$E = \sum_{i=1}^N e(t_i) \cdot \Delta t \quad (4-2)$$

where e is the absolute error (V) (Eq. 3-6), Δt is the value of its sampling interval, N the number of data point used. This is reported with respect to model performance later in this thesis. For the integrated error, a smaller value indicates better model performance.

The integrated error and R^2 of each dataset from four different sampling intervals is presented in Figure 4-14 ($t_{in} = 60$ s, $\Delta i = 0.4$ A cm⁻²). From this, it can be seen that a sparser sampling procedure results in poorer performance, as the integrated error increases with a larger sampling interval. With sampling intervals increasing from 1 s to 8 s, the integrated error grows steadily and the coefficient of determination drops, meaning that the predicted cell voltage deviates from the experimental data with a larger sampling interval.

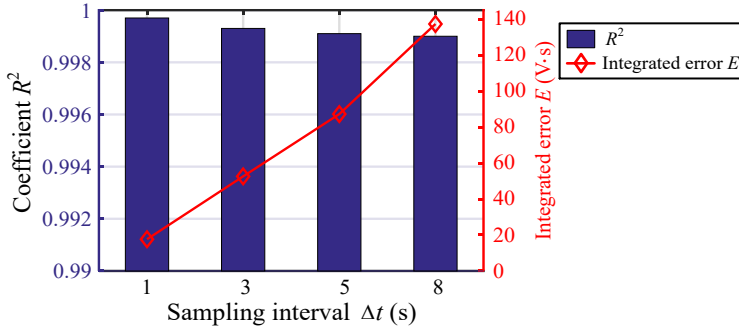


Figure 4-14: Performance comparison at different sampling intervals ($\Delta t = 1, 3, 5, 8$ s) [108].

To summarize, intensive sampling results in better model performance. When the experiment was carried out with a specific sampling interval, the changes in the operating condition, as well as the amplitude of the data variation in the system, exerted apparent effects on the model's performance and the effect of the ramp value on the model's performance being smaller at low current densities than that at the higher one.

4.4.2 Ramp value

The absolute error (V) (Eq. 3-6) is used to compare the impact of ramp value on the LSSVM model performance. Two ramp values, namely $\Delta i = 0.2$ A cm⁻² (Case 1) and $\Delta i = 0.5$ A cm⁻² (Case 4) are considered. The ramp time of both cases is $t_{in} = 60$ s. The current density profiles of the two cases are shown in Figure 4-15. The LSSVM model's results under these two cases are provided in Figure 4-16 and Figure 4-17, respectively. The maximum absolute error of Case 1 is approximately 0.04 V, but that of Case 4 is 0.07 V. Furthermore, a lower root mean square error ($RMSE = 9.47 \times 10^{-5}$) and higher coefficient ($R^2 = 0.9916$) in Case 1 confirm that the LSSVM model performs better with smaller load changes. Many sharp increases in the absolute

error can be found in Figure 4-16 and Figure 4-17, which share a similar pattern to the results in Figure 4-12 and Figure 4-13. However, when comparing this with the absolute error of the two model results, it can be seen that in Figure 4-16, at a high current density, the absolute error in the up-ramp is larger than that in the down-ramp. However, in Figure 4-17, no similar trends were observed, as there was no noticeable difference between the up-ramp and down-ramp at a high current density. This is because in this region, the changes in current density are smaller than the anticipated ramp value of 0.5 A cm^{-2} , as the maximum current density value is set as 1.19 A cm^{-2} in the white-box model.

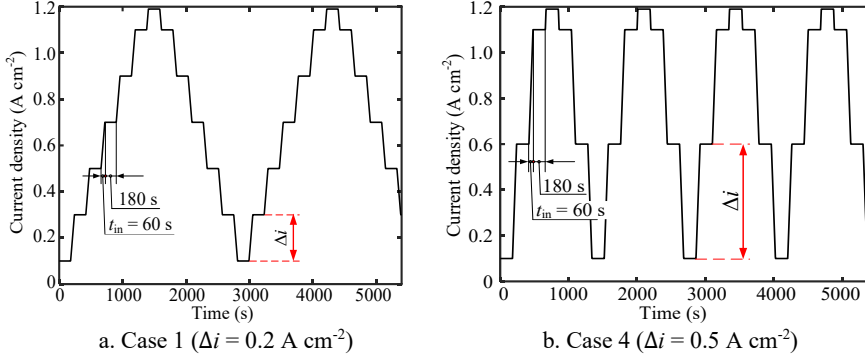


Figure 4-15: Current density with ramp time $t_{in} = 60 \text{ s}$ (Operating condition is listed in Table 4-II).

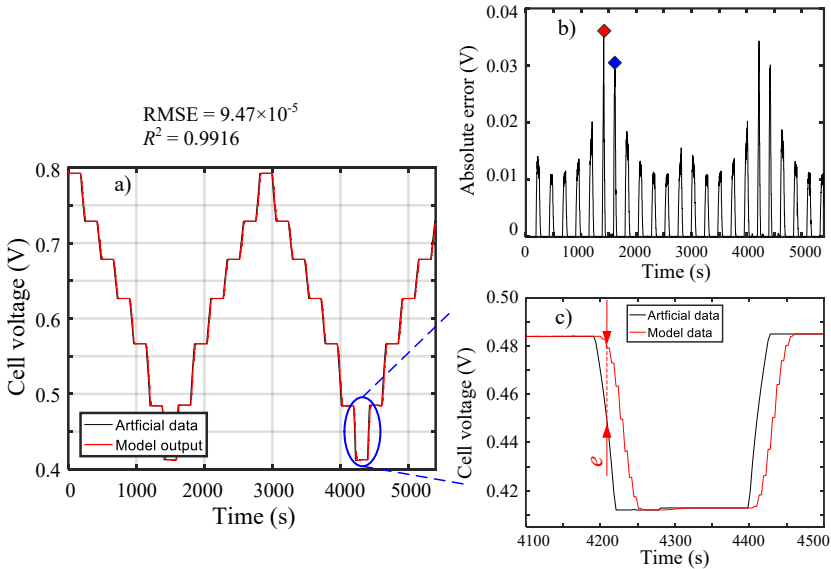


Figure 4-16: LSSVM model performance – Case 1 ($\Delta i = 0.2 \text{ A cm}^{-2}$): a) Model output approximated to artificial data; b) absolute error; c) zoomed region [108].

4 Analysis of the suitability of the LSSVM model under ideal cases

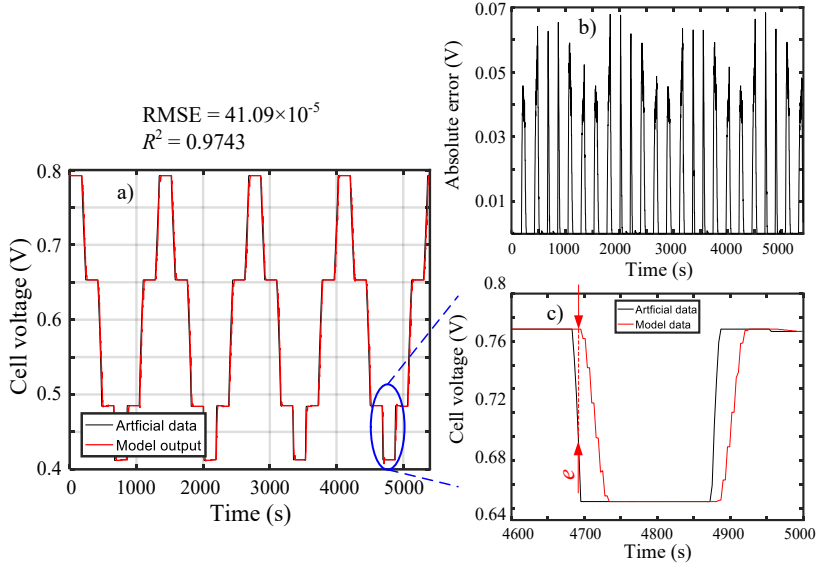


Figure 4-17: Model performance – Case 4 ($\Delta i = 0.5 \text{ A cm}^{-2}$): a) Model output approximated to artificial data; b) absolute error; c) zoomed region [108].

The integrated error and coefficient of determination are employed to discuss the impacts of the ramp value on the LSSVM model's performance. The modeling results of the LSSVM model under 10 cases (listed in Table 4-III) are shown in Figure 4-18. It can be found from this figure that as the ramp value increases, the integrated error increases correspondingly, but the coefficient of the determination decreases. This indicates that a smaller change in the current density brings about more satisfactory model results. At large ramp values resulting in an even larger change in voltage, the LSSVM model perform less accurate compared with the model's results when small ramp values were loaded.

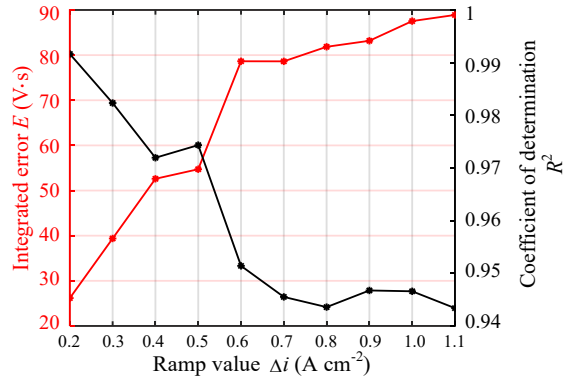


Figure 4-18: Effects of ramp value on the LSSVM model performance [108].

4.4.3 Ramp time

The impacts of the ramp time on the LSSVM model's performance are investigated here. All of the numerical experiments were carried out at a constant sampling interval of $\Delta t = 3$ s and ramp value $\Delta i = 0.2$ A cm⁻². The LSSVM model's results of both processes are also presented in Figure 4-19 and Figure 4-20, respectively. The middle column of both figures shows the predicted cell voltage (red line) against the artificial data (black line). A small difference is found between these two lines, which indicate a good modeling performance of the LSSVM model. But a small horizontal shift is observed. The shift in Figure 4-19 is slightly larger than that of in Figure 4-20 meaning that the fuel cell system is more likely to be characterized by the LSSVM model, when the load change has a longer ramp time. The absolute error of the LSSVM model at the ramp times $t_{in} = 60$ s and $t_{in} = 180$ s are also provided in the bottom column of Figure 4-19 and Figure 4-20, respectively. As is presented in the figures, the longer ramp time ($t_{in} = 180$ s) results in a smaller absolute error. In Figure 4-20, with $t_{in} = 180$ s, the maximum absolute error is lower than 0.02 V, but in Figure 4-19 with $t_{in} = 60$ s, the value almost triples to reach 0.06 V. Abrupt increases in the absolute error were observed in every ramp period. Furthermore, at a high current density, the absolute error at the up-ramp is larger than that at the down-ramp, which is consistent with the conclusions in the sampling interval and ramp value sections. In addition, the smaller RMSE and larger R^2 in Figure 4-20 compared to Figure 4-19 shows that the LSSVM model output is more likely to approximate the correct voltages with a longer ramp time.

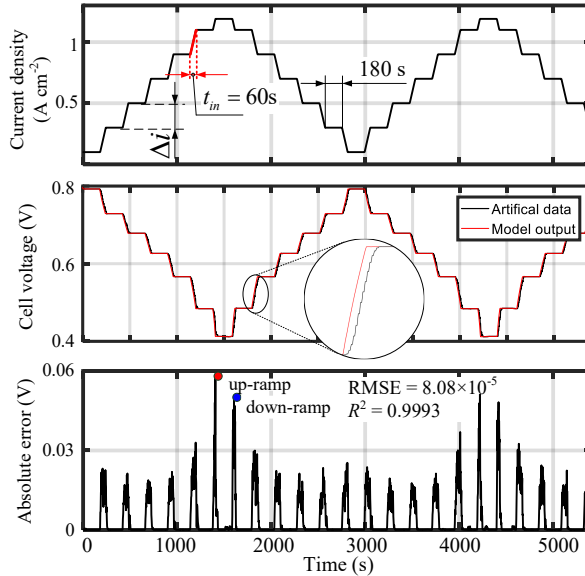


Figure 4-19: Performance analysis of the LSSVM model: $t_{in} = 60$ s (Top row: current density profile; Middle row: the black line is an artificial voltage and the red line is the LSSVM model's output; Bottom row: the absolute error of the model) [108].

4 Analysis of the suitability of the LSSVM model under ideal cases

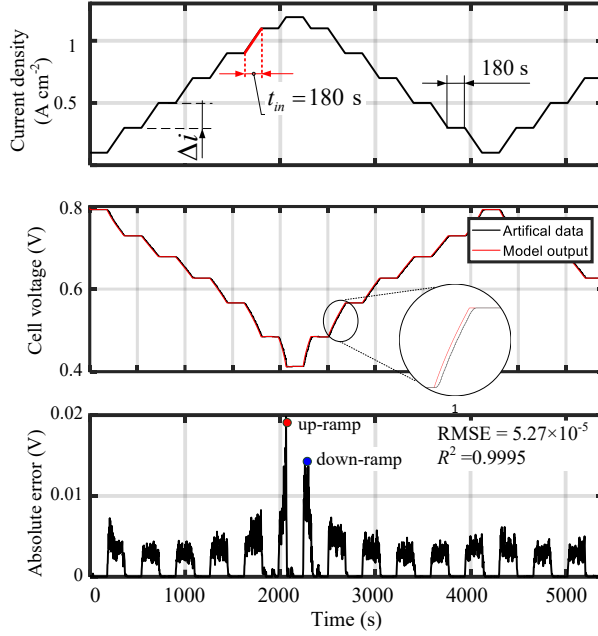


Figure 4-20: Performance analysis of the LSSVM model: $t_{in} = 180$ s (Top row: current density profile; Middle row: the black line is an artificial voltage and the red line is the LSSVM model's output; Bottom row: the absolute error of the model) [108].

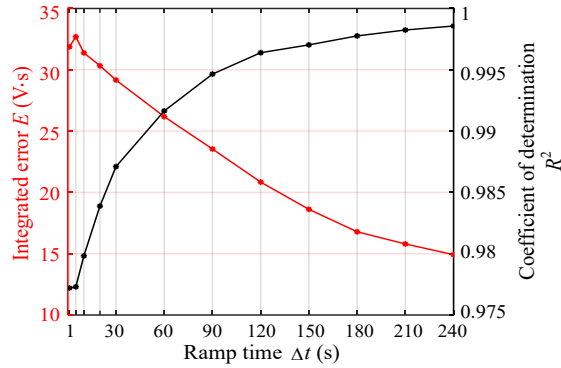


Figure 4-21: Effect of the ramp time on the LSSVM model's performance [108].

By implementing the LSSVM model under 12 processes, each with its corresponding ramp time $t_{in} = 1$ s, 5 s, 10 s, 20 s, 30 s, 60 s, 90 s, 120 s, 150 s, 180 s, 210 s, and 240 s, respectively, the effects of the ramp time on the LSSVM model's performance are summarized, as shown in Figure 4-21. The integrated error and coefficient of determination are used. As the ramp time becomes longer, the integrated error decreases accordingly, but the coefficient of the determination increases. This means that a longer time for the changing of the current density

brings about more satisfactory model results. In particular, when the ramp time is short, i.e., less than 30 s, a small change in the ramp time will lead to a significant improvement in the model's performance.

4.5 Analysis on the LSSVM model

Sampling interval

In Figure 4-22, the coefficient of determination (Eq. 3-8), amongst all sampling intervals, ramp times and ramp values, are summarized. First, with an intensive sampling interval such as $\Delta t = 1$ s (Figure 4-22a), the coefficients of the determinations are more likely to approximate a value of one, which means a better model performance compared to the other three sampling intervals (Figure 4-22b, Figure 4-22c, and Figure 4-22d). Moreover, with a sparser sampling interval, increasing the ramp time has less of an impact on the model's performance when the ramp value is small. As can be seen in each sub-figure in Figure 4-22, when the ramp value is less than 0.5 A cm^{-2} (three lines at the top of each sub-figure), ramp time increases, while the changes in R^2 are not as obvious as with large ramp values ($\Delta i \geq 0.6 \text{ A cm}^{-2}$).

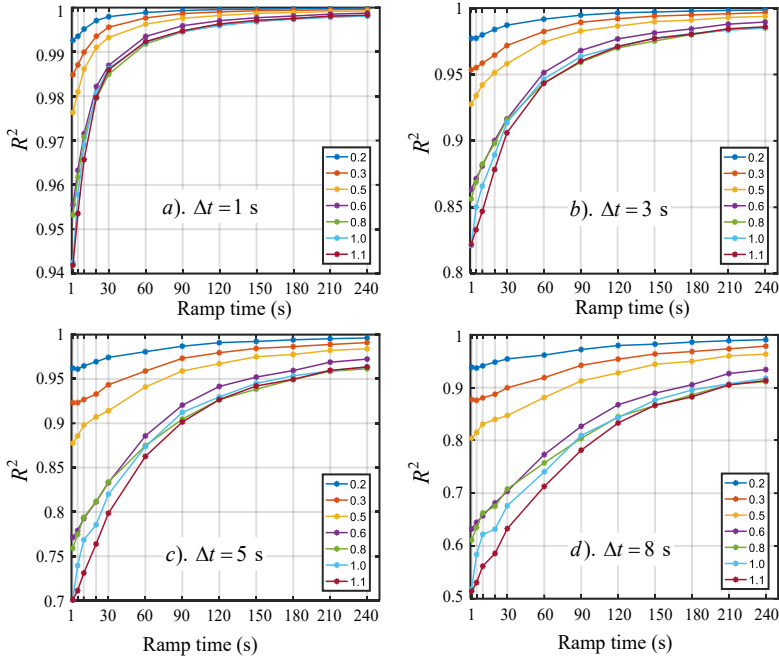


Figure 4-22: The coefficient of determination(R^2) among three effect factors: sampling interval (from Figure 4-22a to Figure 4-22d), ramp time (x-axis) and ramp value: A cm^{-2} (different colored lines). Higher R^2 represents better model's performance [108].

4 Analysis of the suitability of the LSSVM model under ideal cases

As mentioned above, with sampling interval $\Delta t = 3$ s, the model not only performs well, but is also economical. Following the discussion, the numerical experiments were carried out at $\Delta t = 3$ s.

Here, we defined the minimum, maximum and average R^2 as a function of the ramp time and ramp value as follows:

interval: $\mathbf{a} = [1, 3, 5, 8]$, $\mathbf{a} \in \mathbb{R}^{1 \times 4}$, $j = 1, \dots, 4$; $a_j \in \mathbf{a}$ in (s)

ramp value: $\mathbf{b} = [0.2, 0.3, 0.4, 0.5, 0.6, 0.7, 0.8, 0.9, 1.0, 1.1]$, $\mathbf{b} \in \mathbb{R}^{1 \times 10}$, $k = 1, \dots, 10$, $b_k \in \mathbf{b}$ in (A cm^{-2});

ramp time: $\mathbf{c} = [1, 3, 5, 10, 30, 60, 90, 120, 150, 180, 210, 240]$, $\mathbf{c} \in \mathbb{R}^{1 \times 12}$, $l = 1, \dots, 12$, $c_l \in \mathbf{c}$ in (s);

Ramp value

In order to discuss the impacts of the ramp value on the model performance, minimum, maximum and average coefficient of determination R^2 (Eq. 3-8) for each ramp value:

$$R^2_{\min}^b = \min\{R^2_l^b\}, l = 1, \dots, 12 \quad (4-3)$$

$$R^2_{\max}^b = \max\{R^2_l^b\}, l = 1, \dots, 12 \quad (4-4)$$

$$R^2_{\text{avg}}^b = \frac{1}{12} \sum_{l=1}^{12} R^2_l^b \quad (4-5)$$

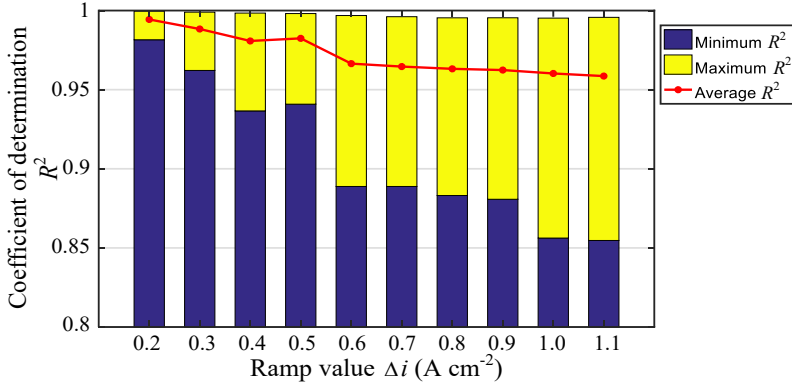


Figure 4-23: Performance comparison with different ramp values [108].

In Figure 4-23, the bar chart shows the coefficient of the determination of R^2 (Eq. 3-8) of each voltage modeled from Case 1 to Case 10 (see Table 4-III) with the ramp value moving from 0.2 A cm^{-2} to 1.1 A cm^{-2} by 0.1 A cm^{-2} . The blue bar represents the minimum R^2 (Eq. 4-3), the yellow bar represent the maximum R^2 (Eq. 4-4) and the red line is the average R^2 (Eq. 4-5). With the increase in the ramp value, the LSSVM model's performance is reduced. When compared with the maximum of each ramp value, only a slight difference is observed, as the

entire maximum R^2 is close to 1. However, a large difference can be found when comparing the minimum R^2 amongst the other results (the dark blue part in Figure 4-23). It can be noticed that with the ramp value of $\Delta i = 0.6 \text{ A cm}^{-2}$, the minimum R^2 drops sharply when compared with the model result under the ramp value $\Delta i = 0.5 \text{ A cm}^{-2}$. When the ramp value exceeds 0.6 A cm^{-2} , a further increase in it has less of an effect on the model's performance.

Ramp time

In order to discuss the impacts of the ramp time on the model performance, defines minimum, maximum and average R^2 of each ramp time as following:

$$R^2_{\min}^c = \min \{R_k^c\}, k = 1, \dots, 10 \quad (4-6)$$

$$R^2_{\max}^c = \max \{R_k^c\}, k = 1, \dots, 10 \quad (4-7)$$

$$R^2_{\text{avg}}^c = \frac{1}{10} \sum_{k=1}^{10} R_k^c \quad (4-8)$$

In Figure 4-24, the bar chart shows the coefficient of determination R^2 (Eq. 3-8) of each voltage model with the ramp time increasing from 1 s to 240 s. The blue bar represents the minimum R^2 (Eq. 4-6), the yellow bar represent the maximum R^2 (Eq. 4-7) and the red line is the average R^2 (Eq. 4-8). It can be seen that a longer ramp time brings about a larger R^2 ; in other words, a better model performance. Moreover, with the increase in the current density in a short time period, such as $t_{\text{in}} \leq 30 \text{ s}$, the differences between the maximum R^2 and minimum R^2 are large (the yellow part of each bar). This means that with a short ramp time, the ramp value has a large impact on the model's performance. In addition, it can be seen in Figure 4-24 that once the ramp time exceeds 90 s ($t_{\text{in}} \geq 90 \text{ s}$), a further increase in the ramp time has less of an impact on the model's performance, as the variation of maximum, minimum and average R^2 tends to be small. When applying the LSSVM method in the real application, if the load change step is severe or the working zone of the current density is wide, a longer ramp time should be considered to ensure the model's efficiency.

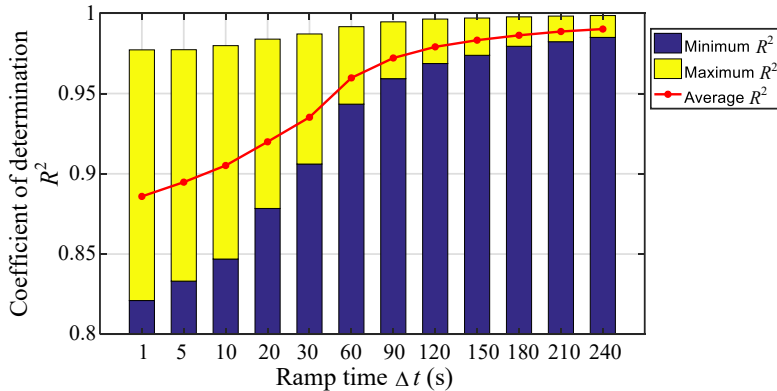


Figure 4-24: Performance comparison with different ramp times [108].

4.6 Conclusions

The accuracy of the LSSVM model was evaluated in this chapter. The idea of introducing artificial data eliminates the experimental uncertainties. A protocol of 480 numerical tests was implemented to evaluate the impacts of the system's setup and load changes on the LSSVM model. Four sampling intervals, ten ramp values, and twelve ramp times were considered, while the absolute error, root mean square error, coefficient of determination and integrated error were employed to define and compare the model's performance. The results show that the low frequency sampling results in poor model performance. With a determined sampling interval, the effect of the ramp value on model performance is smaller at a low current density than at a high one. Moreover, the changes in the current density have a noticeable impact on the model's performance. A small step in the ramp value brings about satisfactory model results and a longer time for the changing of the current density results in satisfactory model performance. In addition, the effect of the ramp value on the model's performance is larger than the influence of the ramp time change.

5 Credibility of the LSSVM model under oscillation cases

Results in this chapter have been submitted to the journal ‘Applied Energy’, and accepted by the journal. The focus of this chapter is the analysis on the LSSVM model’s credibility and definition of its reliable working zone regarding to various load changes. Although the effects of the system’s setup and exterior load change on the LSSVM model’s performance have been discussed in chapter 4, but conclusions drawn from chapter 4 was derived from the analysis of the ideal cases, which means it is not enough to characterize the real state of the fuel cells’ operating conditions. Thus, a more accurate definition of the working domain of the transient voltage model under more practical operating condition are presented in this chapter, including the following parts: Section 5.1 introduces the data preparing process, oscillation on cell voltage is analyzed; impacts of system’s setup and load changes on the LSSVM model’s performance are illustrated in Section 5.2; the working zone which regulates the impact factors to the LSSVM model can be found in Section 5.3; and Section 5.4 draws the conclusions.

5.1 Artificial data preparation

A wide range of operating conditions should be considered when discussing the suitability of the transient voltage model, which means a large number of data should be provided. Significant efforts are required when sufficient and comprehensive experiments are carried out to cover almost all possible operating conditions. However, running this bunch of experiments is time consuming and there are some limitations of the test rig, for example, extreme operating conditions should be avoided to protect the fuel cell, which contributes to data-missing. Thus, a simulation based on physical and electrochemical law was run in Simulink to generate artificial data.

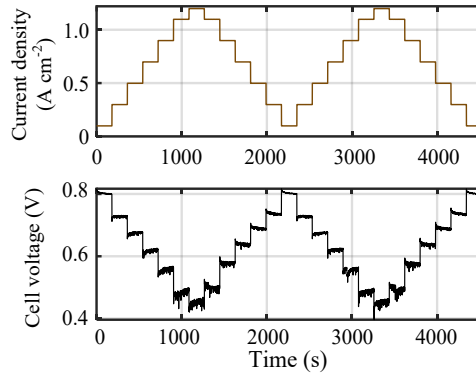


Figure 5-1: Voltage-current density profiles: collected from test rig (Brown line: current density; black line: cell voltage; operating temperature: 343.15 K; $\lambda_{an} = 2.0$, $\lambda_{ca} = 2.0$; $RH_{an} = 90\%$, $RH_{ca} = 90\%$).

In section 4.3, the white-box model was carried out to generate a deterministic voltage to a given current density, in which only idealized state was considered. However, in real operating fuel cells, an oscillated voltage is always observed, as shown in Figure 5-1. In order to make the artificial data able to reflect the practical oscillation on voltage, statistical analysis on the practical cell voltage is carried out and added on the artificial data generated in section 4.3. The workflow of how to process the data and carry out the analysis is presented in Appendix. It includes the following main ideas:

- A set of experiments are carried out, and the practical cell voltages are collected;
- A Fourier transform is applied to the cell voltage, and the voltage is decomposed into its constituent frequencies. High frequencies are selected, and considered as the oscillation that are caused by fuel cell system abnormality;
- The Inverse Fourier transform is applied to the high frequencies information, and the results are the amplitude of the oscillation on the cell voltage;
- These oscillation values are classified according to their corresponding current density and voltage properties.

5.1.1 Experiments

The experiments are running in our test rig, details can be found in section 3.3, and the operating conditions are listed in Table 5-I. Twelve experiments are implemented to the statistical analysis, with different current density profiles, as listed in Table 5-II. Three current density ramp value ($i = 0.2 \text{ A cm}^{-2}$, 0.5 A cm^{-2} , and 0.8 A cm^{-2}), and four ramp time ($t_{in} = 1 \text{ s}$, 20 s , 30 s , and 120 s) are chosen.

Table 5-I: Operating conditions.

Anode	Anode reactant	Hydrogen
	λ_{anode}	2.0
	Temperature	343.15 K
	Relative humidity	90%
Cathode	Cathode reactant	Air
	$\lambda_{cathode}$	2.0
	Temperature	343.15 K
	Relative humidity	90%

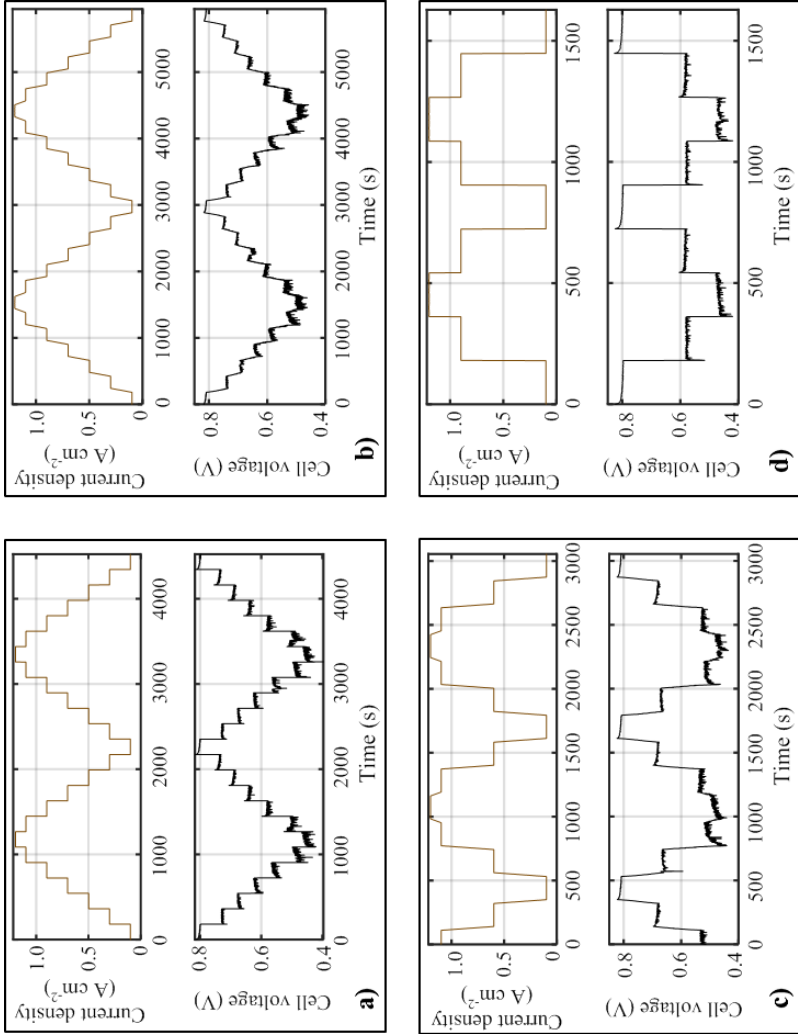
Table 5-II: Properties of current density profiles in test rig.

Experiments No.	1	2	3	4	5	6	7	8	9	10	11	12
Ramp value (A cm^{-2})	0.2	0.2	0.2	0.2	0.5	0.5	0.5	0.5	0.8	0.8	0.8	0.8
Ramp time (s)	1	20	30	120	1	20	30	120	1	20	30	120

The starting current density is always 0.1 A cm^{-2} and remains for 180 s, then the load ramps in a specific ramp value with given time, and remains at the current value for 180 s. These steps

are repeated until the limited current density (1.2 A cm^{-2}) is reached. Maintaining at the limited value for 180 s, then, the current density is decreased at a rate of the specific ramp value with given time, until the current density measures 0.1 A cm^{-2} . Two cycles are applied in each experiment. The experimental voltage and current density profiles of No. 3, No. 6, and No. 9 are shown in Figure 5-2a, b, c, and d respectively. It can be found in the figure that the oscillation amplitude on the cell voltage varies by different current densities. At low current densities level, a slight oscillation can be found on voltage, while at high current densities, a more severe oscillation is observed. As sharp increase in current density is applied in experiments No. 1 and No.9, a more severe overshoot and undershoot are found in Figure 5-2a and Figure 5-2d when comparing with Figure 5-2b and Figure 5-2c.

Figure 5-2 : Voltage-current density profiles collected from test rig: a) experiments No. 1; b) experiments No.3; c) experiments No. 6; d) experiments No. 9 (Black line: cell voltage; brown line: current density; operating temperature: 343.15 K; $\lambda_{dm} = 2.0$, $\lambda_{ca} = 2.0$; $RH_{dm} = 90\%$, $RH_{ca} = 90\%$).



5.1.2 Oscillation analysis

In theory, for a given current density, the voltage should be stable without oscillation. There are many reasons for voltage oscillation, such as oxygen starvation, superfluous heat, water droplet accumulation in flow channel, membrane flooding, etc. [110,111]. The impacts of these factors on the cell voltage are regarded as noise or disturbance affecting the fuel cell system. And the cell voltage with oscillation is regarded as signal requiring denoising. In order to extract this kind of noise from the cell voltage, Fourier transform is first applied to the cell voltage, which is a mathematical transform which turns a function of time into a function of frequency. After the Fourier transform, frequency spectrum of the cell voltage is obtained. A low-pass filter that passes signals with a frequency lower than a selected cutoff frequency and eliminates all frequencies above the cutoff frequency is applied. As only low frequencies can pass through the filter, the oscillations in the cell voltage are eliminated and smooth cell voltage is obtained.

Fourier transforms:

$$F(\zeta) = \int_{-\infty}^{\infty} f(t)e^{-2\pi i\zeta t} dt \quad (5-1)$$

Inverse Fourier transforms:

$$f(t) = \int_{-\infty}^{\infty} F(\zeta)e^{2\pi i\zeta t} d\zeta \quad (5-2)$$

here, t represents time, and $f(t)$ a function of time, here is the cell voltage of the fuel cell; $\zeta \in \mathbb{R}$ represents frequency in units of Hz, and i is the imaginary number, $i^2 = -1$.

Fourier transform to cell voltage:

$$V(\zeta) = \int_{-\infty}^{\infty} v(t)e^{-2\pi i\zeta t} dt \quad (5-3)$$

Inverse Fourier transform with high frequencies are removed:

$$\hat{v}(t) = \int_{-\infty}^{20} V(\zeta)e^{2\pi i\zeta t} d\zeta \quad (5-4)$$

here, $v(t)$ is the experimental cell voltage, $V(\zeta)$ is the frequency spectrum of cell voltage, the cutoff frequency is set as 20 Hz, and $\hat{v}(t)$ the smooth cell voltage after removing high frequency spectrum of cell voltage.

The filtering results of two cell voltages, experiment No.1 and No.5 in Table 5-II, are shown from Figure 5-3 to Figure 5-6. The ramp times of both experiments are 1 s while the ramp value is different. The ramp value of No.1 is 0.2 A cm⁻², and No.5 is 0.5 A cm⁻². The blue lines in Figure 5-3 and Figure 5-5 are the smooth cell voltages after filter high frequencies in experimental cell voltage. The value of extracted noises from the experimental voltage of No.1 and No.5 (Table 5-II) are shown in Figure 5-4 and Figure 5-6, respectively. It can be found in these two figures that the noise at high current densities is larger than that of at low current densities. The sudden changes in current density bring about overshoot and undershoot in cell voltage, and consequently result in large noise values.

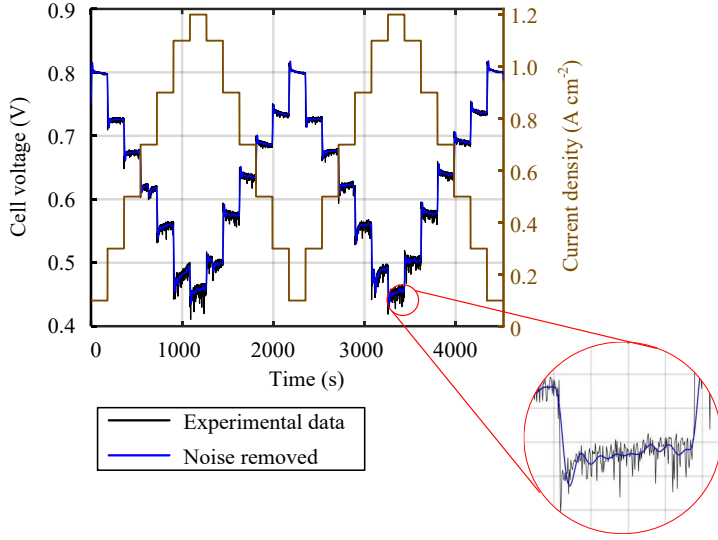


Figure 5-3: Filtering results of cell voltage, experiment No.1 in Table 5-II (Brown line: current density, black line: cell voltage collected from the test rig, blue line: smooth cell voltage removed oscillation).

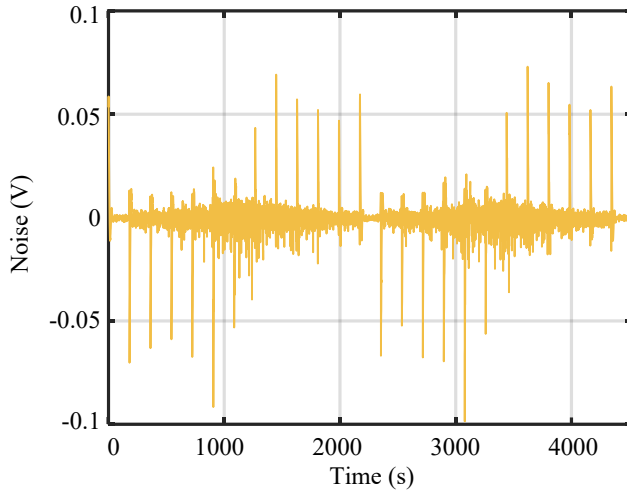


Figure 5-4: Extracted noise from cell voltage, experiment No.1 in Table 5-II.

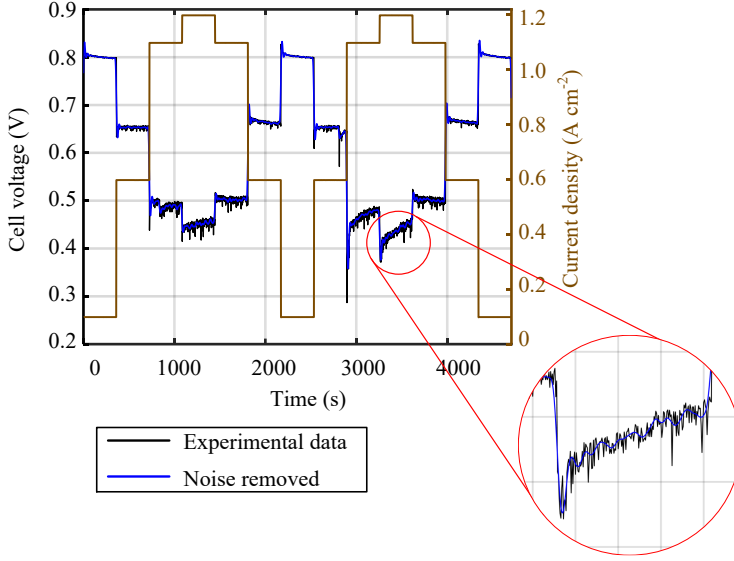


Figure 5-5: Filtering results of cell voltage, experiment No.5 in Table 5-II (Brown line: current density, black line: cell voltage collected from the test rig, blue line: smooth cell voltage removed oscillation).

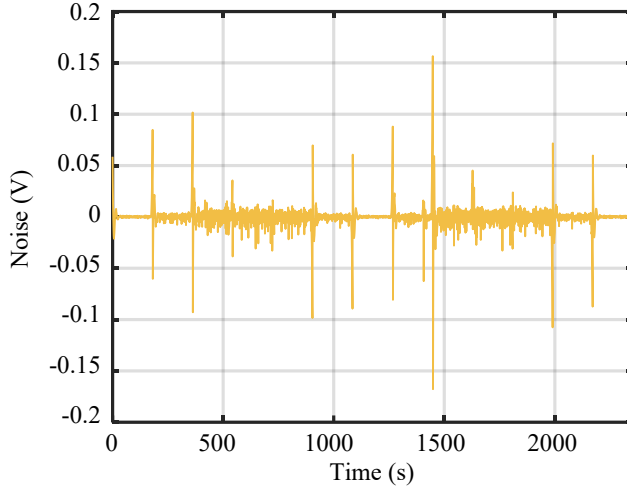


Figure 5-6: Extracted noise from cell voltage, experiment No.5 in Table 5-II.

5.1.3 Artificial data validation

After the extracted noises of the 9 experiments are calculated, analysis on these noises is carried out, in order to find a pattern of voltage oscillation relating current density value and current density changes. The noise is assumed to be white noise. The amplitude of the noises at each current density is calculated, and the correlation between the ramp value and amplitude

is considered. The analyzed results are listed in Table 5-III. The analyzed noises are added to the deterministic voltage generated by Simulink simulation in section 4.2 to get artificial results realistic oscillations as observed in the experiment. The artificial data against experimental data is shown in Figure 5-7, in which the experiment No.1 is employed. The current density profile is marked in brown, and the experimental cell voltage is black. The green line represents the artificial data including voltage oscillation. The zoomed in region in Figure 5-7 shows that the artificial data approximates the real experimental data very well as the difference between these two profiles are very small. The absolute error between the experimental and artificial data is presented in Figure 5-8 where the maximum value is smaller than 0.08 V and most absolute error is smaller than 0.03 V. And considering the voltage varying between 0.4 and 0.85 V, such error is within the acceptable range, which means that the artificial data can be used as alternative to experimental data.

Table 5-III: Analyzed noises amplitude at different current densities [112].

Current density (A cm^{-2})	Noise amplitude (mV)
0.1	[-3.2, 3.2]
0.3	[-4.5, 4.5]
0.5	[-7.9, 7.9]
0.7	[-8.9, 8.9]
0.9	[-10.5, 10.5]
1.1	[-13, 13]
1.2	[-15.1, 15.1]

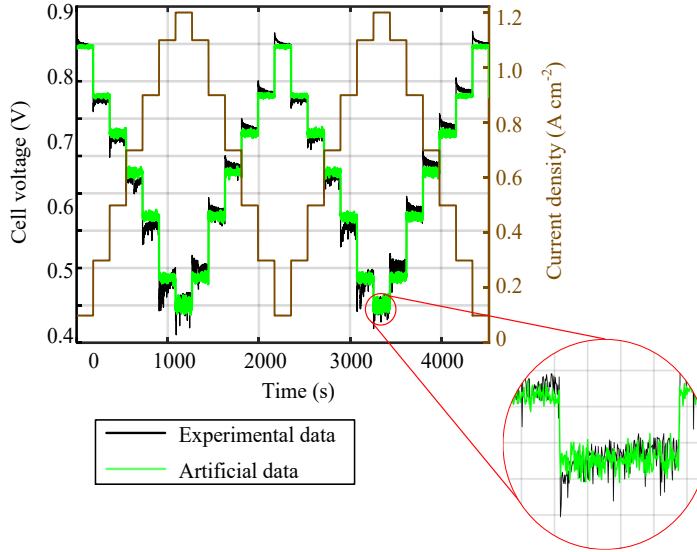


Figure 5-7: Artificial data against experimental data, experiments No.1 in Table 5-II (Brown line: current density; Black line: cell voltage collected from the test rig; Green line: artificial data with oscillation).

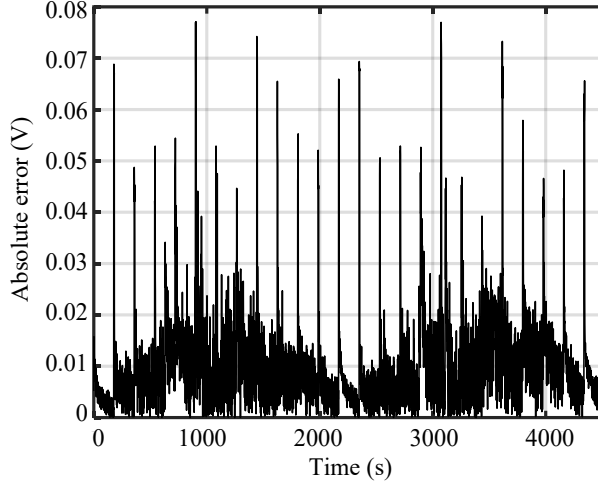


Figure 5-8: Absolute error between experimental data and artificial data.

5.2 Impacts of factors on the LSSVM model

With sufficient artificial data, the accuracy of the LSSVM model under various load changes is evaluated and the limitation of the model is explored. Sampling intervals and load changes are employed as impact factors. Here, four sampling intervals, nine ramp values and twelve ramp times are considered. In total a protocol of 432 numerical tests was conducted.

5.2.1 System's setup

In the test station, sampling interval should be pre-determined before running the experiments, by which the parameters' state are collected, analyzed and controlled by the fuel cell system. When a high degree of accuracy of the system is required, an intensive sampling should be considered so that more information on the system is provided. But in this case, a large storage space is demand and always brings out heavy-computation burden. Thus, due to different properties and requirements on the experiments, the sampling interval could be different. For a fast-dynamic system, intensive sampling interval should be used to catch its transient behaviors. And a sparse sampling interval could be taken into consideration when it is an inertial system. Considering the oscillation on the cell voltage are mainly caused by the water transportation in the fuel cell, and the transport lag in fuel cells to be about 10 s [113], then, four sampling intervals are chosen to discuss their effect on the LSSVM model performance, which are 1 s, 3 s, 5 s, 8 s. Figure 5-9 illustrates how sampling intervals affects the collected data. The current density and voltage profiles preserved with sampling interval $\Delta t = 1$ s are shown in Figure 5-9a and Figure 5-9b respectively. The preserving processes with intervals $\Delta t = 3$ s and $\Delta t = 8$ s are shown in Figure 5-9c and Figure 5-9d. The results information from the data preserving processes under two sampling intervals ($\Delta t = 3$ s and $\Delta t = 8$ s) can be found in Figure 5-9e and Figure 5-9f, respectively, and the red line is the artificial data with Δt

= 3 s and the blue line with $\Delta t = 8$ s. From Figure 5-9, it can be found that sparse sampling interval will cause the information of the system missing and the artificial data are partially incomplete.

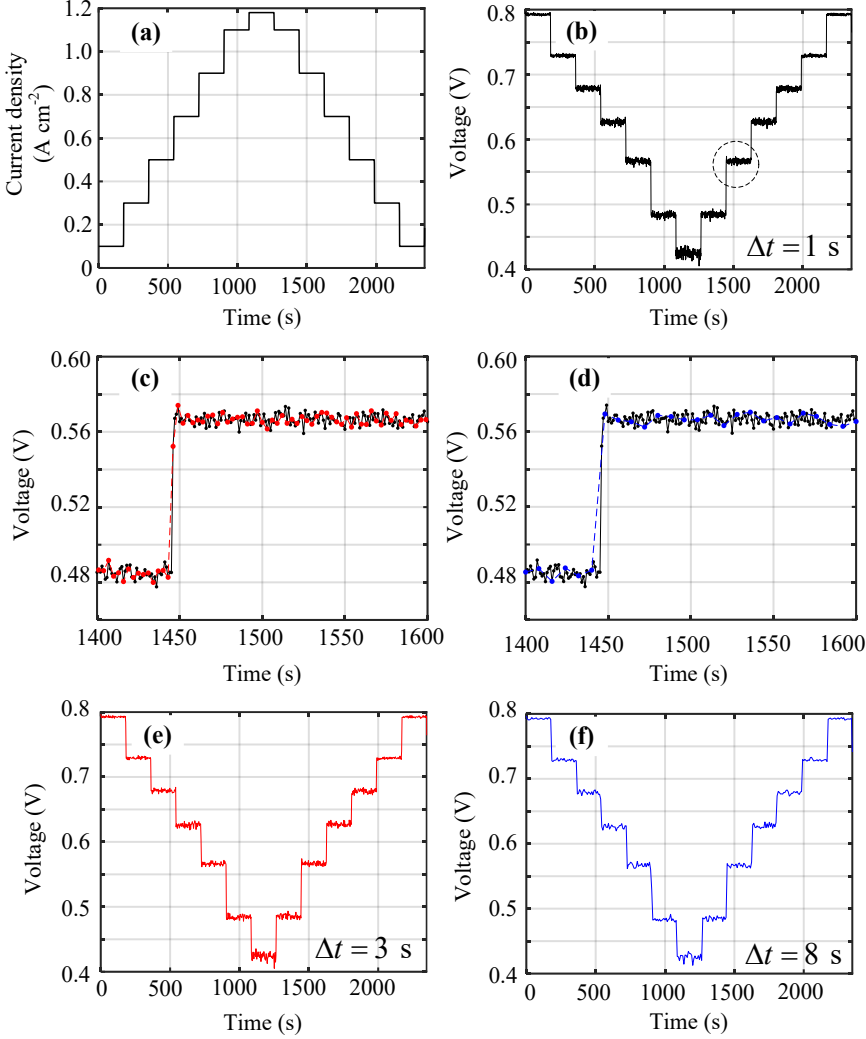


Figure 5-9: Data collecting with different intervals : (a) current density; (b) cell voltage with $\Delta t = 1$ s; (c) zoomed region, 3 s; (d) zoomed region, 8 s; (e) cell voltage with $\Delta t = 3$ s; (f) cell voltage with $\Delta t = 8$ s ($T_{an} = 343.15$ K, $T_{ca} = 343.13$ K, $\lambda_{an} = \lambda_{ca} = 2$, $RH_{an}=100\%$ and $RH_{ca} = 100\%$).

The cell voltage predicted by the LSSVM model against the artificial data is shown in Figure 5-10, in which the sampling interval is 3 s. The black line in Figure 5-10 is the artificial data and the red line is the predicted cell voltage by LSSVM model. The zoomed region illustrates

that the LSSVM model smooths the artificial data, but the sharp peak of the artificial cell voltage after the load change is not resolved. The model results against the artificial with interval 8 s are shown in Figure 5-11, in which the black line is the artificial data and the blue line is the model output. In contrast to the data in Figure 3-8, the zoom into a ramp region shows a larger deviation between the input data (experimental or artificial) and the modeled data when the sampling interval was increased in Figures 5-10 and 5-11. When comparing the two black lines Figure 5-10 and Figure 5-11, it can be found that the artificial data in Figure 5-11 is smoother than in Figure 5-10. In the zoomed region of Figure 5-11, no sharp peak is caught from the black line, indicating that the large sampling interval will result in missing system information. In Figure 5-10, it takes a certain time of red curve to reach the same level of black line, but it takes even longer for blue line in Figure 5-11 to reach the level of black curve. This time is caused by the missing information of the fuel cell voltage when large sampling interval is employed, and is positively related to the sampling interval. Also, when comparing approximation performance of the model output in Figure 5-10 (red line) and Figure 5-11 (blue line), it is clear that the model's prediction ability in dealing with data preserved by interval $\Delta t = 3$ s shows better consistency with the artificial data (black line) than that of data preserved by interval $\Delta t = 8$ s.

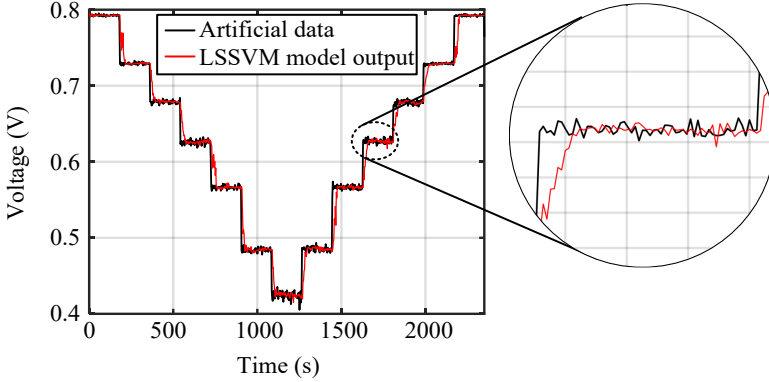


Figure 5-10: Model performance under sampling interval $\Delta t = 3$ s.

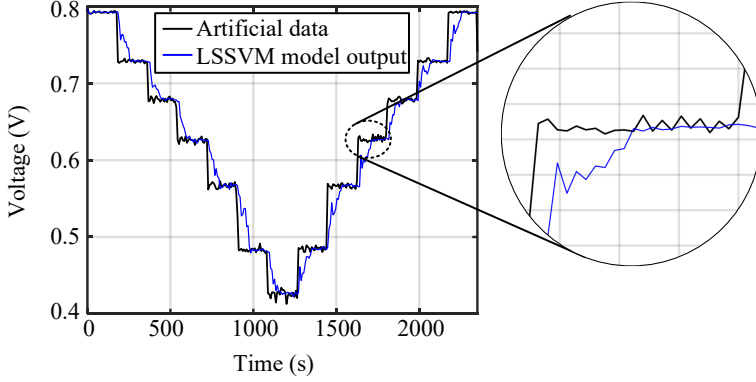
Figure 5-11: Model performance under sampling interval $\Delta t = 8$ s.

Table 5-IV: Indices for the model by four sampling intervals.

Δt	1 s	3 s	5 s	8 s
Integrated error (Vs)	21.75	36.68	50.55	72.69
RMSE (10^{-4})	0.943	2.190	3.254	5.105
R^2	0.9919	0.9811	0.9720	0.9558

The integrated error, root mean square error (RMSE) and coefficient of determination (R^2) of model results of four sampling intervals ($\Delta t = 1, 3, 5, 8$ s) are listed in Table 5-IV. A smaller integrated error and RMSE represent better model performance, but a larger R^2 value represents better model performance. From Table 5-IV it can be concluded that a sparser sampling procedure results in poorer performance, because the highest integrated error and RMSE and lowest coefficient of determination are found in the results from sampling interval $\Delta t = 8$ s.

5.2.2 Load changes

As the effect of the sampling intervals of the system on the LSSVM model performance has been clarified, considering the tradeoff between the cost of storage and model error, sampling interval $\Delta t = 3$ s is chosen for the analysis of system dynamics. How the load change affects the model's performance is discussed on two factors: the ramp value and ramp time.

5.2.2.1 Ramp value

A protocol of artificial data with 9 different ramp values was conducted. Each process begins with the current density at 0.1 A cm^{-2} and runs for 5400 s. The constant values of current density change (i) of each case are listed in Table 5-V. The time used for the current density change is set constant here, which is $t_{in} = 30$ s for each test (Case 1-9).

Table 5-V: Ramp value in current density.

Case	1	2	3	4	5	6	7	8	9
(A cm^{-2})	0.2	0.3	0.4	0.5	0.6	0.7	0.8	0.9	1.0

The current density profile and model results from two cases (Case 1 and Case 3) are shown in Figure 5-12 and Figure 5-13 respectively. The maximum absolute error when modeling Case 1 is about 0.07 V, but the maximum value in Case 3 model result is around 0.11 V. In addition, at each current density change process, the absolute errors become larger than that of at constant current density operating conditions. Meanwhile, when comparing the absolute error of the two cases with each load changes, it can be found that the value of Case 1 is smaller than the value of Case 3. In the zoomed regions of Figure 5-12 and Figure 5-13, the oscillations of the artificial voltage are in the same order of magnitude as the oscillations of the LSSVM model. The sharp peak of the cell voltage after a ramp change cannot be resolved completely by the LSSVM model.

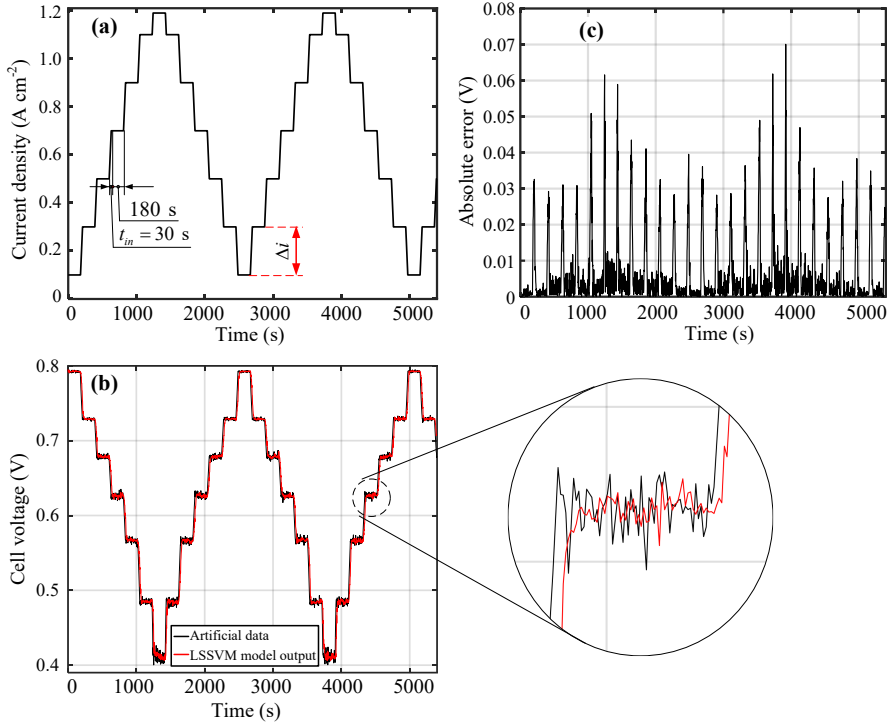


Figure 5-12: Model performance Case 1, ramp value $\Delta i = 0.2 \text{ A cm}^{-2}$: (a) current density; (b) model output against the artificial voltage; (c) absolute error of the modeling results [112].

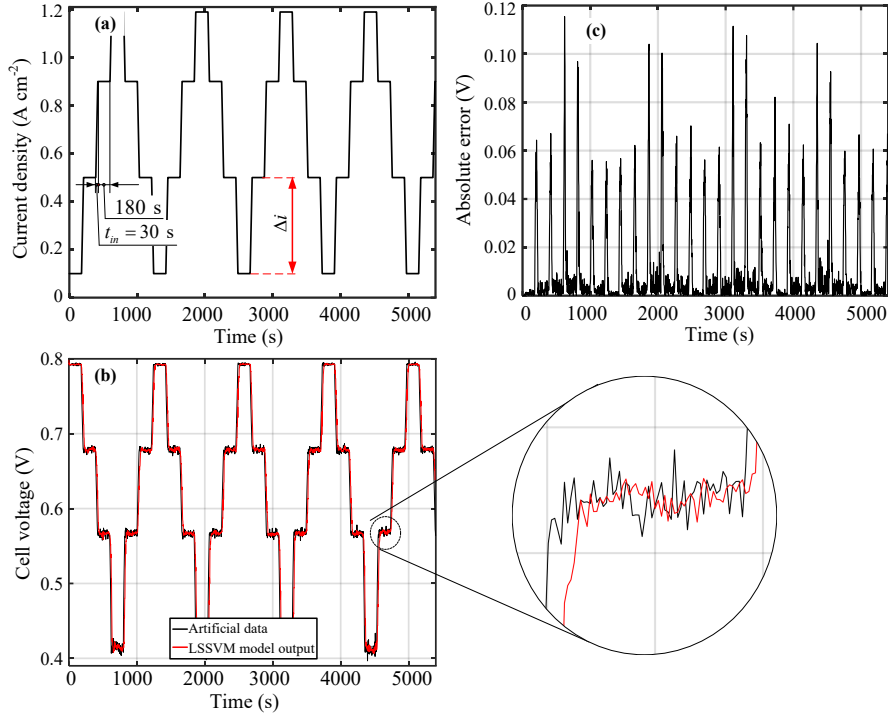


Figure 5-13: Model performance Case 3, ramp value $\Delta i = 0.4 \text{ A cm}^{-2}$: (a) current density; (b) model output against the real voltage; (c) absolute error of the modeling results [112].

Then, the integrated error and coefficient of determination are used to compare the model performance when dealing with different load change values. The results obtained by nine cases are listed in Figure 5-14. As smaller integrated error and larger R^2 represent a better model performance, it can be found from Figure 5-14 that the LSSVM model can predict the cell voltage more precisely when smooth load change is applied. The worst performance happened in dealing with severe load change, with $i = 1.0 \text{ A cm}^{-2}$, but the coefficient of determination is 0.930, which still shows a good approximation ability of the LSSVM to catch the cell voltage transient behavior when large current density changes are loaded.

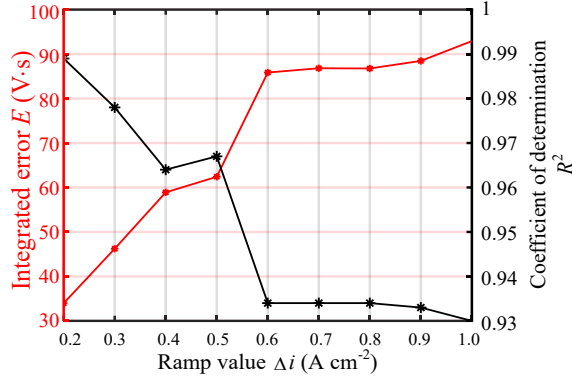


Figure 5-14: Model results of nine cases.

5.2.2.2 Ramp time

A protocol of artificial data with 12 different ramp values was conducted, as listed in Table 5-VI. Each process begins with current density at 0.1 A cm^{-2} and runs for 5400 s, and were carried out under constant sampling interval $t = 3 \text{ s}$ and ramp value $\Delta i = 0.2 \text{ A cm}^{-2}$.

Table 5-VI: Ramp times.

Case	1	2	3	4	5	6	7	8	9	10	11	12
(s)	1	3	5	10	30	60	90	120	150	180	210	240

Two model results with ramp time $t_{in} = 30 \text{ s}$ and $t_{in} = 180 \text{ s}$ are shown in Figure 5-16 and Figure 5-16, respectively. In the top row of Figure 5-15 is the current density profile of the modeling processes with ramp time $t_{in} = 30 \text{ s}$, and the process begins with current density at 0.1 A cm^{-2} and increased stepwise to 1.2 A cm^{-2} by a step of 0.2 A cm^{-2} , after each increase the current density hold at this value for 180 s. Until the current density reach its limited value 1.2 A cm^{-2} , the current desnity was decreased stepwise to 0.1 A cm^{-2} by 0.2 A cm^{-2} . The whole process runs for 5400 s. The middle row of Figure 5-15 shows the model predicted voltage (red line) against the real voltage value (black line). The cell voltage of both processes are well predicted by the model as the difference between these two lines are relatively small. The zoomed regions share similar oscillation in the real voltage and the output of the transient mdoel. But a small horizontal shift is observed. In the top row of Figure 5-16 is the current density profile of the modeling processes with ramp time $t_{in} = 180 \text{ s}$. The current density increased stepwise from 0.1 A cm^{-2} to 1.2 A cm^{-2} by a step of 0.2 A cm^{-2} , and each increase takes 180 s. When the limited current density is reached, then decrease the current density symmetrically. The whole process runs for 5400 s. The middle row of Figure 5-16 shows the model predicted voltage (red line) against the real voltage value (black line). The cell voltage of both processes are well predicted by the model as the difference between these two lines are relatively small.

The zoomed regions share similar oscillation in the real voltage and the output of the transient model. Still, a small horizontal shift is observed [112].

When comparing the absolute error of the two modeling results, bottom column in Figure 5-15 and Figure 5-16, it can be found that the absolute errors in Figure 5-16 are smaller than the error in Figure 5-15 in general. In brief, the slower the load changes, the better the model performance.

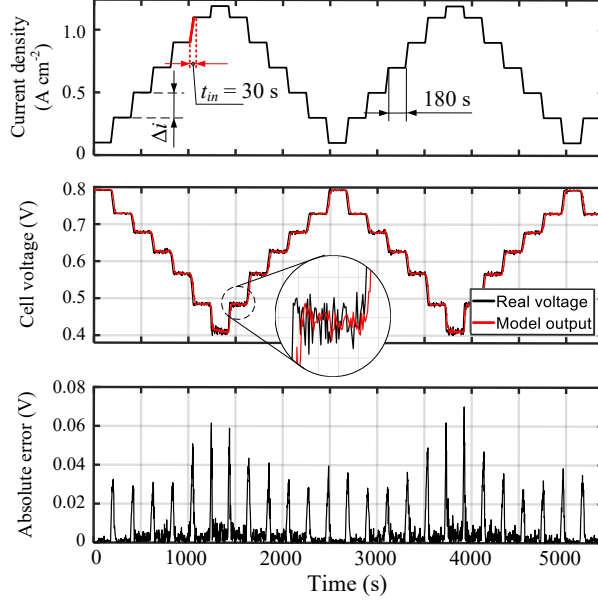


Figure 5-15: Performance analysis of the LSSVM model: $t_{in} = 30$ s (Top row: current density profile; Middle row: black line is artificial voltage and red line is LSSVM model output; Bottom row: the absolute error of the model) [112].

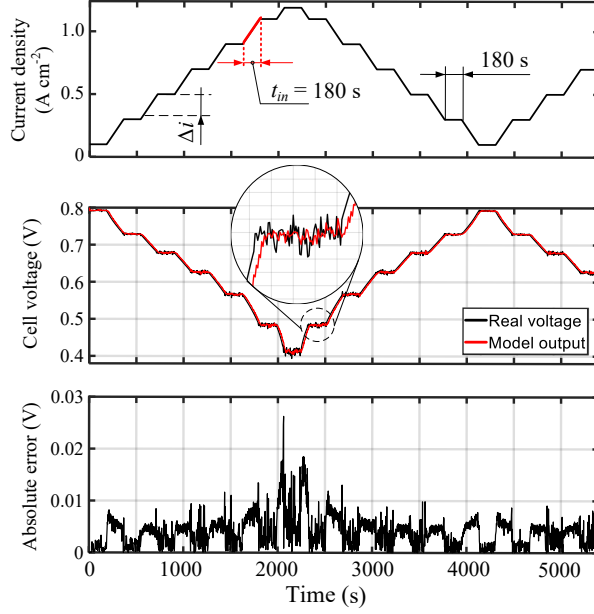


Figure 5-16: Performance analysis of the LSSVM model: $t_{in} = 180$ s (Top row: current density profile; Middle row: black line is artificial voltage and red line is LSSVM model output; Bottom row: the absolute error of the model) [112].

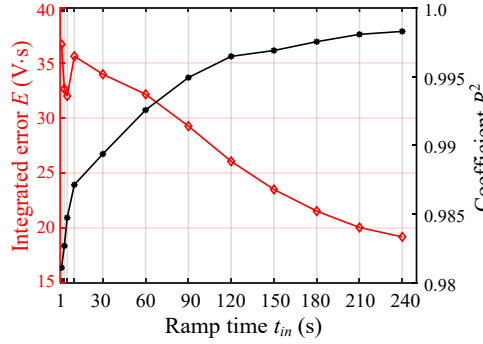


Figure 5-17: Effect of ramp time on LSSVM model performance [112].

Figure 5-17 shows the integrated error and the coefficient of determination of each voltage model with the ramp time changing from 1 s to 240 s. As the ramp time becomes longer, the coefficient of determination increases correspondently, from 0.981 to 0.998, meanwhile, the integrated error decreases from 36.7 V s to 19.2 V s. This also proves that a longer time for the changing of the current density brings about more satisfactory model results. In particular, when the ramp time is short, such as less than 20 s, a small increase in the ramp time will improve the model's performance significantly.

5.3 Working zone for the LSSVM model

The combined effects of the sampling interval, ramp value and ramp time are discussed detailed here. The coefficient of determination, maximum absolute error and average absolute error of each modeling process are shown in Figure 5-18, Figure 5-19, and Figure 5-20, respectively. x -axis is the sampling interval, y -axis the ramp time and the colored lines represent ramp values. It should be noted that, for better visibility, the sampling interval has different direction in Figure 5-18 compared to Figure 5-19 and Figure 5-20.

z -axis in Figure 5-18 is the coefficient of determination R^2 . Comparing the coefficient of determination (R^2) in x -axis direction, it can be found that larger sampling interval (e.g. $\Delta t = 8$ s) results in lower value of R^2 when comparing the corresponding value from sampling interval 1 s, 3 s and 5 s. With $\Delta t = 1$ s, the lowest value of yellow line is about 0.94, but with $\Delta t = 8$ s, this value drops to 0.65. Moreover, by analyzing the R^2 in y -axis direction and among four sampling intervals, it is clear that when the sampling interval is large, extending the ramp time can largely improve the model accuracy. Because the R^2 increases more obviously with increased ramp time in sampling interval $\Delta t = 8$ s than sampling interval $\Delta t = 1$ s. From this figure, the load change behavior can be classified into two types, smooth ramp change and sharp ramp change. The ramp values ($\Delta i = 0.6 \text{ A cm}^{-2}$) above the green dash line are called smooth change and below the green dash line are called sharp change. When the fuel cell ramp value Δi exceeds 0.6 A cm^{-2} , the effect of ramp value on model performance becomes insignificant, as R^2 value of those processes are almost the same.

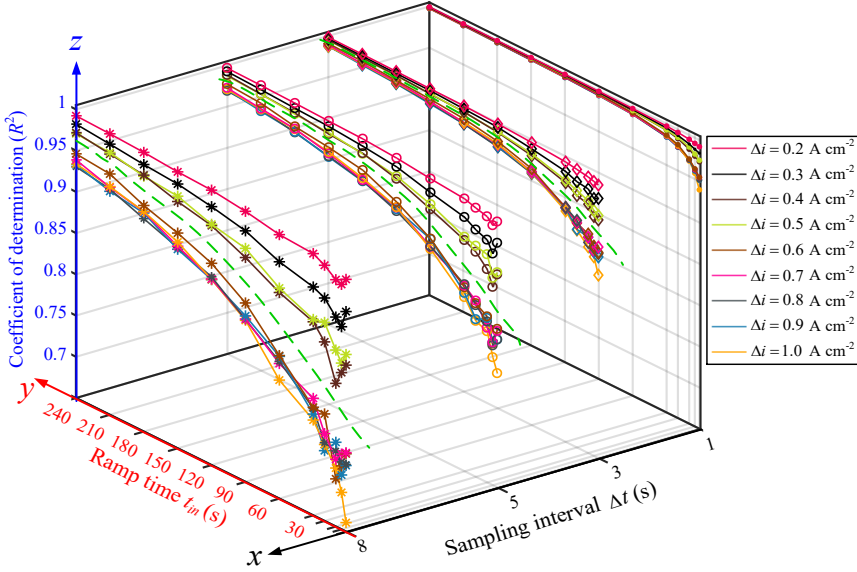


Figure 5-18: The value of coefficient of determination (R^2) among three effect factors: sampling interval (x-axis, positive direction: from right to left), ramp time (y-axis: positive direction: from outside to inside) and ramp value (different colored lines). Higher R^2 represents better model's performance [112].

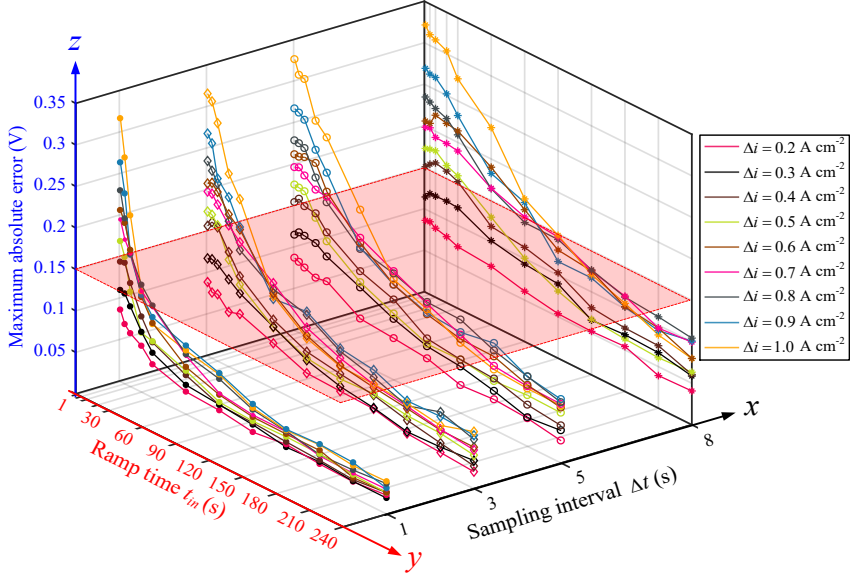


Figure 5-19: The value of maximum absolute error among three effect factors: sampling interval (x -axis, positive direction: from left to right), ramp time (y -axis: positive direction: from inside to outside) and ramp value (different colored lines). Lower maximum absolute error represents better model's performance. (The red plane shows the expected maximum absolute of 0.15 V; the possible cases are under this plane) [112].

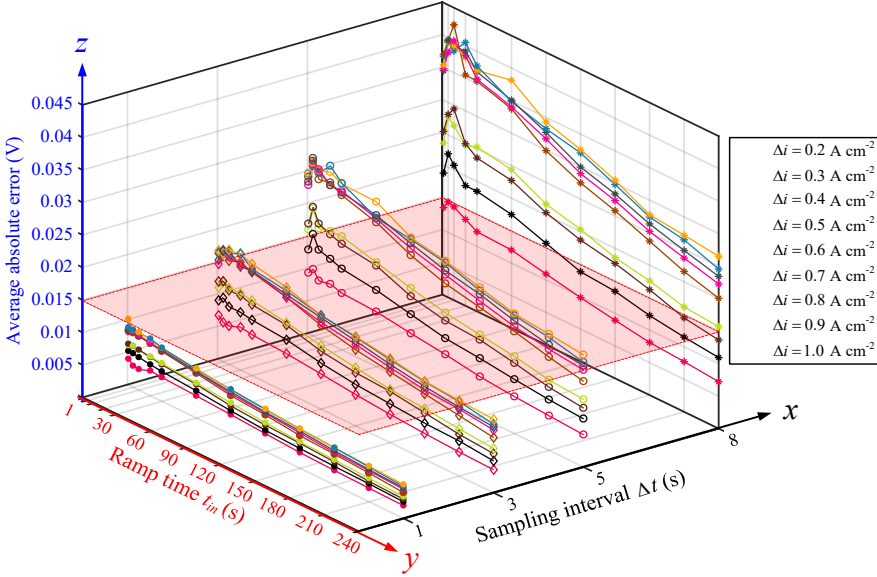


Figure 5-20: The value of average absolute error among three effect factors: sampling interval (x-axis, positive direction: from right to left), ramp time (y-axis: positive direction: from inside to outside) and ramp value (different colored lines). (The red plane shows an example of expected average absolute error of 0.015 V; Possible cases are under this red plane) [112].

z-axis in Figure 5-19 is the maximum absolute error. It is clear that the change in sampling interval has less effect on the reduction of the maximum absolute error. But the increasing in ramp time largely helps to reduce the maximum value especially in short ramp time, which is more obviously when intensive sampling interval is used. When large sampling interval is used (e.g. $\Delta t = 3$ s, 5 s, 8 s), the effect of ramp value on maximum absolute error begins to become larger.

Figure 5-20 shows the average absolute error from each model result. From this point of view, the effect of sampling interval is very clear. With the increase in sampling interval, the average error increases significantly. All the errors in sampling interval $\Delta t = 1$ s are lower than 0.01 V, but the most of errors in sampling interval $\Delta t = 8$ s are larger than 0.01 V. Moreover, the effect of ramp value on model performance is more important than ramp time. In four sampling intervals, the increasing in ramp value (different colored lines) always accompanies with an increase in error but the increasing in ramp time is less significantly.

To make sure that the model satisfies different model accuracy requirements under various load changes, a guideline for applying the LSSVM model to fuel cell transient voltage modeling is given by Figure 5-19 and Figure 5-20. If the modeling process only has the requirement on

the maximum absolute error, for example maximum absolute error is set as 0.15 V, then the possible combinations of sampling interval, ramp time and ramp value are located under the red plane in Figure 5-19. Or if the modeling process only has a requirement on the average absolute error, for example the average absolute should be smaller than 0.015 V, then the possible combinations of sampling interval, ramp time and ramp value are located under the red plane in Figure 5-20. When both maximum absolute error and average absolute error are required by the modeling process, for example the maximum absolute error of the modeling process should be smaller than 0.15 V and the accepted average absolute error is set as 0.015 V, the possible combinations of sampling interval, ramp time and ramp value should be under the red plane in Figure 5-19 and Figure 5-20 at the same time.

5.4 Conclusions

A comprehensive investigation of the credibility of the LSSVM model in dealing with a variety of load changes was carried out in this chapter, and the effects of fuel cell system's setup (sampling interval) and exterior loads' properties (ramp time and ramp value) were presented. The artificial data were generated on the basis of the white-box model proposed in chapter 4 while combined statistical analysis results on the cell voltage oscillation.

A protocol of 432 numerical tests was implemented to evaluate the impacts of the system's setup and load changes on the LSSVM model in this chapter, as four sampling interval, nine ramp values and twelve ramp times were considered. The modeling results, when a sampling interval of 1 s is employed, are better than that of under other sampling values ($\Delta t = 3 \text{ s}, 5 \text{ s}, 8 \text{ s}$). Thus, system with strong dynamic properties should consider small sampling interval in order to acquire detailed information and obtain desirable modeling and performance. When same sampling interval is selected, the model performs well when a smooth load changes are applied, which means smaller ramp value and longer ramp time bring about better model performance. In addition, the results also found that the model performance is more sensitive to the load change when high current density is loaded. Moreover, the effect of the changes of ramp value on the model's performance is larger than the influence of the ramp time.

A working zone that regulates the choice of sampling interval and the variation of the ramp time and ramp value was presented, and a suggestion to find the working zone was given. Two criteria can be used to find the working zone, one is the maximum absolute error and the other is average absolute error. According to different modeling requirements, these two criteria can be used separately or simultaneously. Based on the acceptable error to the fuel cell system, a set of workable combinations of sampling interval, ramp time and ramp value can be found from the guidance, which can be used to instruct the future application of the LSSVM model when dealing with different load changes of the fuel cells are applied.

6 An online adaptive model for nonlinear dynamics of fuel cell

Results in this chapter have been submitted to the journal ‘Applied Energy’. An online adaptive model is proposed in this chapter, which is based on least squares support vector machine. Parameters involved in the LSSVM method itself is initialized by a genetic algorithm, then, the parameters are updated online by gradient method. The genetic algorithm can effectively avoid the initial parameters falling into local minimum, and the online updating for the parameters makes the proposed model more adaptive to the real-time changes of the fuel cell system. The methodology of the proposed model is introduced in section 6.2. Section 6.3 illustrates the online adaptive model. Section 6.4 gives the model performance analysis. And section 6.5 draws the conclusions.

6.1 Problem description

Voltage is easy to be measured, which makes it one of the candidates to indicate the performance of the fuel cell. Majority failures of the fuel cell lead to a drop or abnormality in voltage [114]. For a long-term running fuel cell, degradation in power output is evitable, which is caused by many factors, as shown in Figure 6-1. Water content has strong impact on the cell performance, which causes specific losses [115]. It has significant effects on catalyst and membrane degradation, which causes mechanical stress leading membrane failure and reactant starvation inducing catalyst support inactivity [110,116]. In addition, dynamic load change also impact the fuel cell performance, as the cell voltage loss is much better at constant current density than that of at varying current [117].

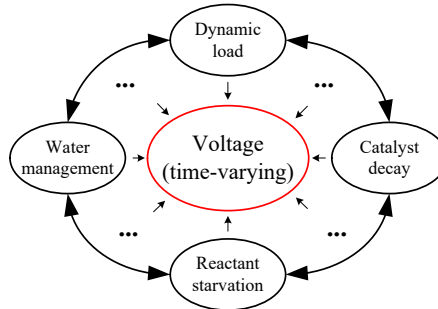


Figure 6-1: Factors affecting the fuel cell performance [118].

As the output of the PEFC fuel cell, voltage should be well modeled, predicted and controlled to provide a stable power output. But modeling and predicting the PEFC voltage are very challenging due to:

- Fuel cell mechanism is too complex and difficult to be online modeled and predicted;
- Complex systems with multiple components are coupled;

- Strong nonlinearity dynamics;
- Time-varying properties due to degradation, water flooding and electrochemical reaction etc.;
- Impacts of load changes, for example, current density ramp value and ramp time.

In chapter 3, the LSSVM model was established to model the cell voltage. Despite a good model accuracy was achieved by the LSSVM model, it has a disadvantage in dealing with various load changes, as different model's accuracy is found at different current densities. In addition, the selection of the parameters of the LSSVM model itself is also a problem. Trial-and-error method is widely used but is inefficient. Therefore, the selection process for the internal parameters, and the LSSVM model established in chapter 3 needs to be optimized in order to find optimal internal parameters and adapt various load changes.

6.2 Methodology

Despite the LSSVM method has a good approximation ability to the fuel cell voltage, which has been proven in previous 3 chapters, still, the performance of the LSSVM method depends highly on the selection of the LSSVM model's internal parameters [119]. In general, trivial grid search methods are used to find feasible parameters of the LSSVM by minimizing the cross-validation prediction value. This trial-and-error method is indeed workable but not a practical solution, because the limited resolution of the grid doesn't provide a way of finding optimal parameters from various possible combinations of the parameter. In addition, due to the data-driven property of the LSSVM method, its performance depends highly on the data used in the model training process. However, the strong nonlinearity and complex mechanism of the PEFC bring great challenging in the modeling process, when the LSSVM method is used. Historical information from the fuel cell cannot well reflect current transient behavior, as long-term operating causes ageing process that is detrimental to fuel cells and changes fuel cell behaviors, making the previous selection of the LSSVM parameters itself less efficient. Thus, an online updating for the LSSVM internal parameters is necessary [118].

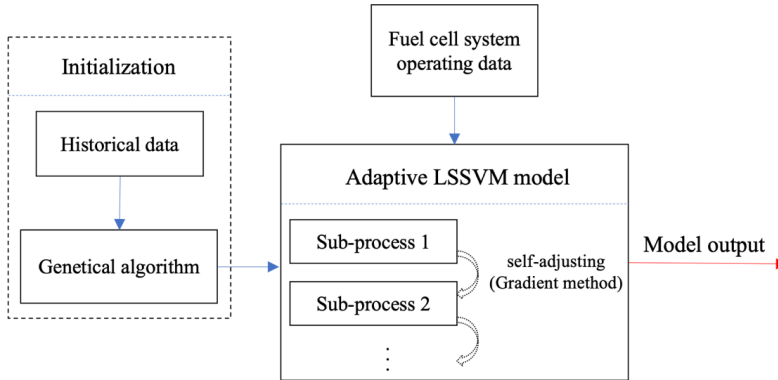


Figure 6-2: Procedure of the developed adaptive LSSVM method.

Accordingly, an adaptive online model that can self-adjust the model's internal parameters and deal with nonlinear dynamics is proposed, as shown in Figure 6-2. Thus, the modeling procedure is as following:

- Initialization: Genetic algorithm is used to determine the initial value of the online model's internal parameters, and pre-existing data are used to learn the initial parameters;
- Model establishment: LSSVM method is then used to learn the time-varying nonlinearity of the system. The modeling process is divided into several sub-processes. In each sub-process, the internal parameters will be updated adaptively by gradient method;
- Adaptability: Gradient method is employed to update the internal parameters of each sub-process with online data.

The LSSVM method has the following form [82]:

$$y = \omega^T \varphi(x) + b \quad (6-1)$$

where $x \in R^n, \varphi(\cdot): R^n \rightarrow R^{n_h}$ is a nonlinear function that maps the input space into a higher dimension feature space. By utilizing training data $\{(x_i, y_i), i = 1, 2, \dots, N\}$, and introducing Lagrangian multiplier α_i , the result of the LSSVM method, details can be found in section 2.2.4, is as follows:

$$\hat{y} = \sum_{i=1}^N \alpha_i K(x, x_i) + b \quad (6-2)$$

where x_i is the model input, \hat{y} the model output, $K(x, x_i)$ the kernel function. α_i and b is the solution of the LSSVM method. Considering the superior properties in handling nonlinearity and complexity [102–104], Gaussian RBF kernel function is chosen $K(x, x_i) = \exp\left(-\frac{\|x-x_i\|^2}{2\sigma^2}\right)$. Then, two internal parameters, namely regularization term γ and width parameter σ , need to be determined.

6.2.1 Genetic algorithm

Selection of a proper parameter set $\{\gamma, \sigma\}$ is the key to achieve an accurate LSSVM model and good performance. But currently no efficient guidelines have been published in finding the optimal parameters. And the manual adjustment of the parameters takes a lot of time and often misses the optimal parameter set [80,120]. Therefore, genetic algorithm (GA) is used here to find the global optimal internal parameters of the LSSVM model. The parameters of genetic algorithm itself need to be set, as shown in Table 6-I. The diagram of the GA is shown in Figure 6-3 with following steps [118]:

1. Initialization population: population size is set to 80. For each individual in the population, it has its own DNA, and the DNA is a sequence of only 1's and 0's. These 80 sequences compose the initial population;

2. Translation DNA: the DNA was decoded and translated into the parameter set $\{\gamma, \sigma\}$. At first, the DNA sequence is decoded following the law of binary to decimal conversion and two decimal digital are obtained consequently. Then, these two decimal digital are scale up or down linear within the range of γ and σ respectively. After the translation, the internal parameters are forwarded to next process;
3. Calculate fitness: fitness is used to score the behavior of individual parameter set $\{\gamma, \sigma\}$. After each $\{\gamma, \sigma\}$ has been used to train the LSSVM model, model error is used to grade the parameter set $\{\gamma, \sigma\}$ (individual DNA), and one with lower model error are labeled higher fitness;
4. Selection population: selection is based on the fitness of each DNA. The goal is to minimize the model error, so the DNA with higher fitness is more likely to be selected into new population;
5. End of condition: 100 generations are used here to judge the end of genetic algorithm, if the GA process has been ran for 100 generations, jump to step 7, otherwise, move to next step;
6. Crossover and mutation: as shown in crossover is used to combine the DNA of two randomly selected individual then generates an offspring. Crossover rate is set 0.3, which means for the selected individual 1, 30% of its DNA will be replaced by the DNA from the selected individual 2; mutation is used to preserve and introduce diversity of the population. Mutation possibility is set 0.01, which means for each individual, it has 1% chance that mutation will happen. When mutation happens, one position in the DNA sequence will be replaced by its opposite, for example 0 is replaced by 1 or 1 replaced by 0. After the new population is generated, back to step 2;
7. Export the results: the DNA of individual with highest fitness in the final population is exported as the initial parameter set of the online adaptive method.

Table 6-I: Parameters of GA.

Parameter	Value
Population size	80
Number of generation	100
Crossover rate	0.3
Mutation possibility	0.01
Range of γ	[1,10000]
Range of σ	[0.01,10]

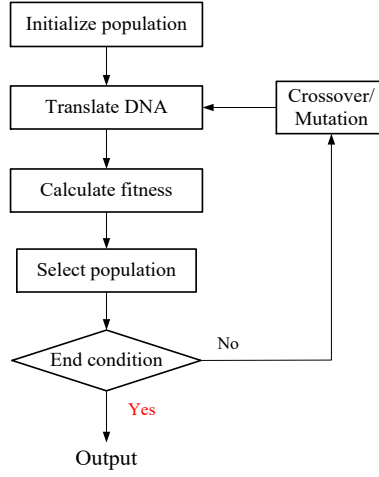


Figure 6-3: Procedures of the genetic algorithm.

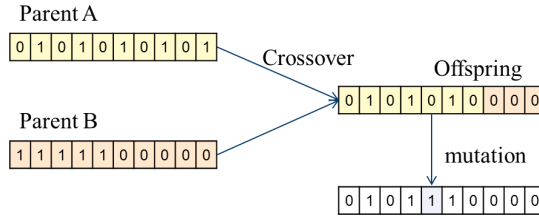


Figure 6-4: Schematic diagram of crossover and mutation in the genetic algorithm.

6.2.2 Gradient method

With the initial parameters of the adaptive model were obtained by the genetic algorithm, the first sub-model is then established. Loss function is used to evaluate the model performance, which is defined as:

$$J(\gamma, \sigma) = \frac{1}{2} [\hat{y} - y]^2 \quad (6-3)$$

where \hat{y} is the LSSVM model output and y is the real value from experiment.

Updating the internal parameters in each sub-model is then achieved by

$$\gamma^{(k+1)} = \gamma^{(k)} - \eta \Delta \gamma^{(k)} \quad (6-4)$$

$$\sigma^{(k+1)} = \sigma^{(k)} - \eta \Delta \sigma^{(k)} \quad (6-5)$$

where k is the number of iteration and η is step size that indicates how fast the parameters change. 10 iterations are used and step size is set as 0.5. And $\Delta \gamma^k = \frac{\partial J}{\partial \gamma}$, $\Delta \sigma^k = \frac{\partial J}{\partial \sigma}$, with $\frac{\partial J}{\partial \gamma} =$

$$e\left(\sum_{i=1}^N e_i K(x, x_i)\right), \frac{\partial J}{\partial \sigma} = 2e\left(\sum_{i=1}^N \alpha_i \cdot \exp\left(-\frac{(x-x_i)^2}{\sigma^2}\right) \cdot \frac{(x-x_i)^2}{\sigma^3}\right)$$

6.3 Online adaptive model

With gradient method, once the internal parameters are updated in current sub-model, for example sub-model s , they are immediately employed in next sub-model (sub-model $s+1$). The configuration of the online adaptive LSSVM model is described in Figure 6-5, which has following steps [118]:

Data collection: two types of data are collected. One is pre-existing data from chapter 3 and 5 that are used to initialize the online adaptive model. The other one is the real-time data that is used in online modeling and updating process. Current and voltage collectors, gas flow rate sensors, pressure sensors and relative humidity sensors are located surround the fuel cell to collect the real-time data at a regular sampling interval. Input parameters are organized as $u(t)$ and output is $y(t)$;

GA Initialization: pre-existing data are learned and processed by GA to find the initial parameters $\{\gamma_0, \sigma_0\}$. The parameter set $\{\gamma_0, \sigma_0\}$ is used to establish the first sub-LSSVM model;

Online updating: after the sub-model was established, gradient method is used to update the internal parameters (Eq. 6-4 and 6-5). The updated internal parameters $\{\gamma_1, \sigma_1\}$ will be used in sub-LSSVM model 2;

Sub-LSSVM models: only the most recent data is used in each sub-LSSVM model, which eliminates the effects of irrelevant information that has less impact on the fuel cell at present. The data used in two adjacent models will partially overlap. In each sub-LSSVM model, the internal parameters have been updated by previous sub-model.

The workflow of how to establish the online adaptive model for nonlinear dynamics of the PEFCs is presented in Appendix.

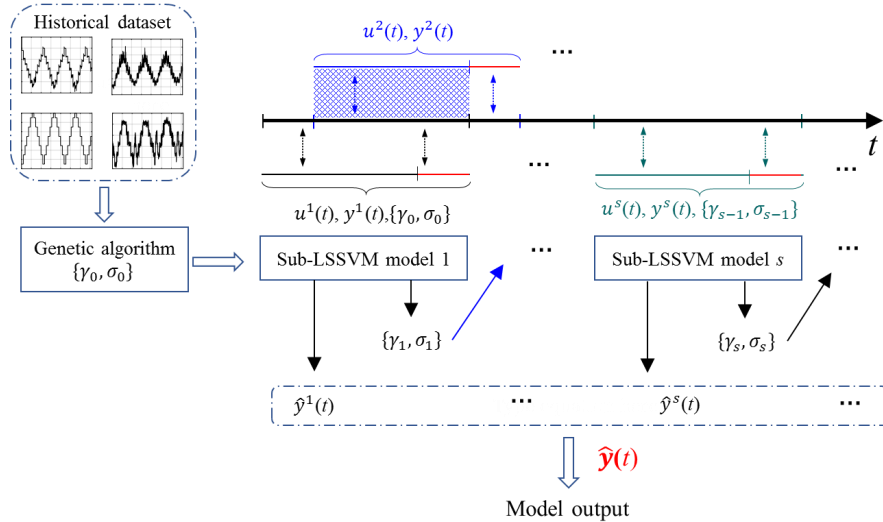


Figure 6-5: Configuration of the proposed method [118].

6.4 Model validation

6.4.1 Validation based on experimental data

In this section, the PEFC test cell which was assembled at the Forschungszentrum Jülich in Germany is used to verify the proposed model performance, details can be found in section 3.3. Greenlight Technology's G40 test rig is used to monitor the fuel cell, as shown in Figure 3-2. In the operating test fuel cell, the current and voltage is collected by corresponding collector. Four gas flow rate sensors are used to collect the inlet and outlet gas flow rate of both anode and cathode side. Two heaters are inserted into anode and cathode sides respectively in order to keep the fuel cell at a desirable working temperature. The operating conditions are listed in Table 6-II.

In the operating fuel cell, the current density is used as exterior load change, as shown in Figure 6-6. In this figure, the blue line is the current density and the black line is the corresponding cell voltage. The measured data are acquired in the measured process with sampling interval $\Delta t = 3$ s, and 2400 samples are collected in the experiment and the experiment last for 2 hours. The starting current density is 0.1 A cm^{-2} , and holds at this value for 180 s. Then, the current density was increased to 0.3 A cm^{-2} by a step of 0.2 A cm^{-2} . Holding the current density for 180 s, and then increase the current density stepwise to its limited value by a step of $\Delta i = 0.2 \text{ A cm}^{-2}$. After the current density reach its limited value, decrease the current density stepwise with same ramp value until the current density becomes 0.1 A cm^{-2} .

Table 6-II: The fuel cell's operating condition.

Anode	Reactant gas	Hydrogen
	λ_{an}	1.2
	Relative humidity	90%
	Temperature	343.15 K
Cathode	Reactant gas	Air
	λ_{ca}	2.5
	Relative humidity	90%
	Temperature	343.15 K

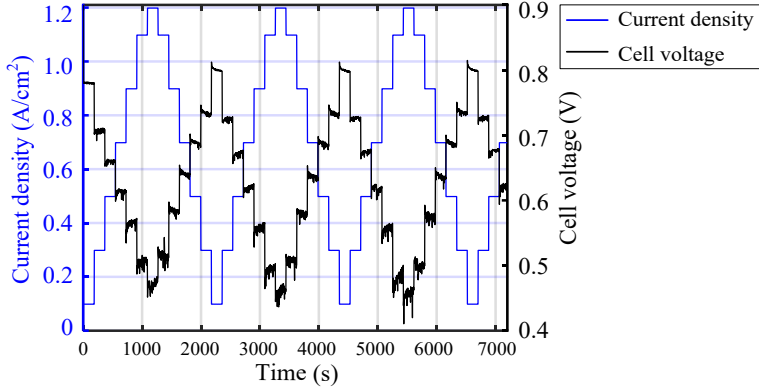


Figure 6-6: Current density profile and corresponding cell output voltage (Operating condition: Table 6-II) [118].

The relative error is employed to evaluate the proposed model's performance of each generation, which is defined as:

$$\varepsilon = \frac{|y_i - \hat{y}_i|}{y_i} \times 100\% \quad (6-6)$$

here \hat{y} is the model output, y the experimental data. A lower value represents a better model performance.

The genetic algorithm is used to find the global optimal parameters for the LSSVM method, and the results (Eq.6-6) of each generation are shown in Figure 6-7. Despite the well-known fact that an infinite number of generations bring about a perfect solution, but it can be seen in Figure 6-7 that after 25 generations, the relative error levels off. Thus, in our case, the 100 generations are enough to obtain global optimal solution. After the initial parameters were found by genetic algorithm, it is forwarded to the proposed online adaptive model. The computation time to initialize parameters under different generations is listed in Table 6-III, and the simulation processes are running on Matlab. The computation time of the process with 25 generations has been defined as basis computation time as T . It can be concluded from Table 6-III that the number of generation and its corresponding computation time are linearly related.

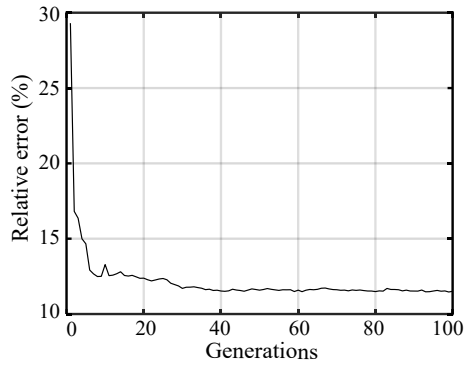


Figure 6-7: Relative error of each generation (Genetic algorithm) [118].

Table 6-III: Computation time of generations (Calculation was implemented using Matlab on a desktop computer with a 3.40 GHz Intel® Core™ i7-2600 CPU and with 16GB RAM) [118].

Number of generation	Computation time (s)	
25	75.02	T
50	150.24	2T
75	233.10	3.1T
100	302.21	4T

As the entire process is decomposed by time into several sub-processes, the LSSVM model to characterize sub-process's voltage can effectively enhance the accuracy of the model. The overall online adaptive voltage model is obtained by integrating every sub-model. In our case, 50 data points are used to establish the sub-LSSVM model, after the sub-model was trained; it is used to predict the fuel cell voltage at the next 12 data points. Then, parameters have been updated after each sub-LSSVM model using the gradient method and these newly calculated parameters are used in the next sub-LSSVM model. The updating parameters γ and σ at each GA generation after each updating process are shown in Figure 6-8 and Figure 6-9, respectively. Calculation time of the updating process for sub-LSSVM model is shown in Figure 6-10, and it can be found from the figure that the calculation time of the parameter updating (γ and σ) is relatively small and lower than 9 millisecond. As each sub-LSSVM model lasts for 162 seconds, the time-consumption of updating process for model's parameters is negligible relative to the sub-model simulation [118].

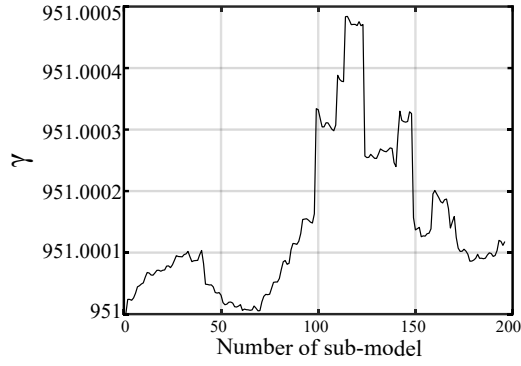


Figure 6-8: Updating process of γ (Eq. 6-4) [118].

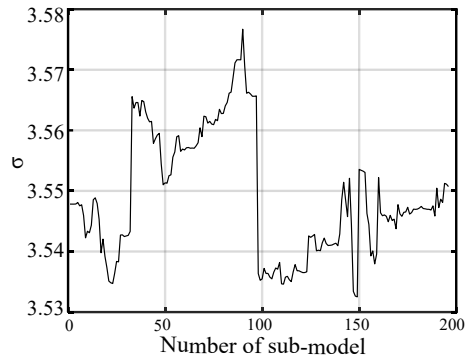


Figure 6-9: Updating process of σ (Eq. 6-5) [118].

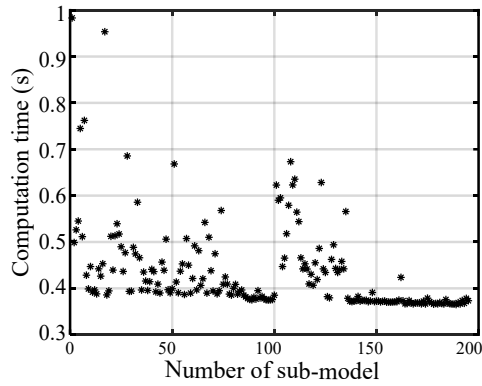


Figure 6-10: Calculation time of each updating process (Calculation was implemented using Matlab on a desktop computer with a 3.40 GHz Intel® Core™ i7-2600 CPU and with 16GB RAM) [118].

The model output against experimental data is shown in Figure 6-11 and the relative error is shown in Figure 6-12, respectively. The red line in Figure 6-11 is the predicted cell voltage from the proposed model and the black line is the measured data from experiment. It can be seen that at low cell voltage, the relative error tends to be larger, as the cell voltage at this low level presents more oscillations due to water management insufficient inside the fuel cell.

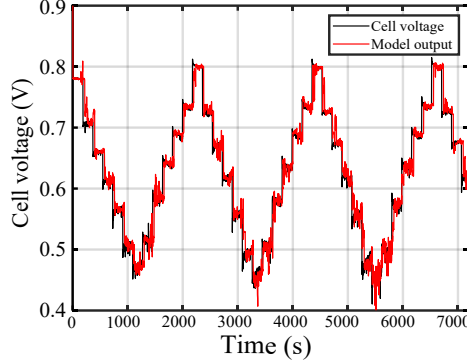


Figure 6-11: Model performance: prediction by the model against the real experimental data [118].

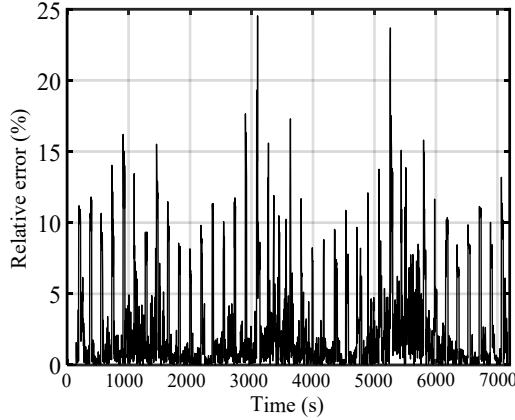


Figure 6-12: Relative error of the modeling results (Eq. 6-6) [118].

More load behaviors were implemented to test and compare the model's adaptability to different load changes, then four cases are used and their current density properties are listed in Table IV. Here we defined that the current density profile in Figure 6-6 as case 1, with ramp value 0.2 A cm^{-2} , and ramp time 1 s. Then, the ramp value in case 2 is 1 A cm^{-2} and ramp time is 60 s, as shown in Figure 6-13. Case 3 has the ramp value 0.5 A cm^{-2} and ramp time is the same as case 1, as shown in Figure 6-14. In case 4, the ramp time is setting as 0.5 A cm^{-2} and ramp time is 60 s, as shown in Figure 6-15.

Table 6-IV: Current density change characteristic of four cases.

	Ramp time t_{in} (s)	Ramp value Δi (A/cm^2)
Case 1	1	0.2
Case 2	60	0.2
Case 3	1	0.5
Case 4	60	0.5

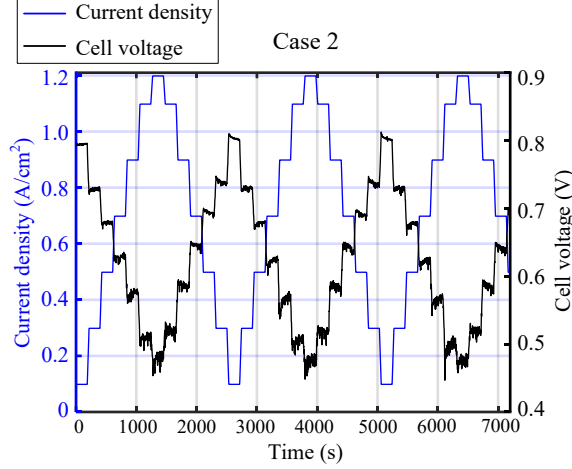


Figure 6-13: Case 2, ramp value $\Delta i = 0.2 A/cm^2$ and ramp time $t_{in} = 60 s$ (Blue line: current density profile; Black line: cell voltage collected from experiment; Operating condition: Table 6-II) [118].

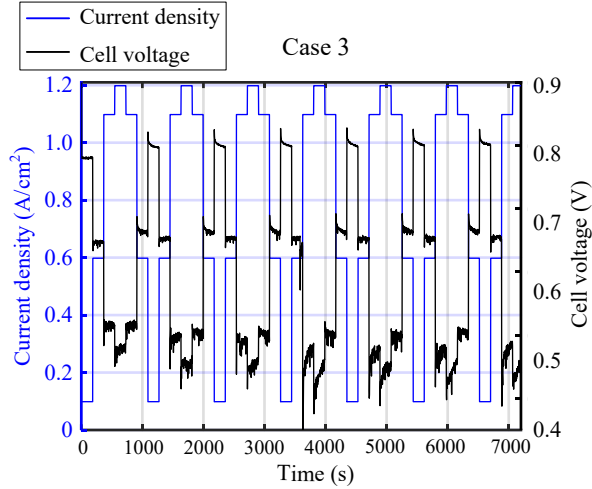


Figure 6-14: Case 3, ramp value $\Delta i = 0.5 A/cm^2$ and ramp time $t_{in} = 1 s$ (Blue line: current density profile; Black line: cell voltage collected from experiment; Operating condition: Table 6-II) [118].

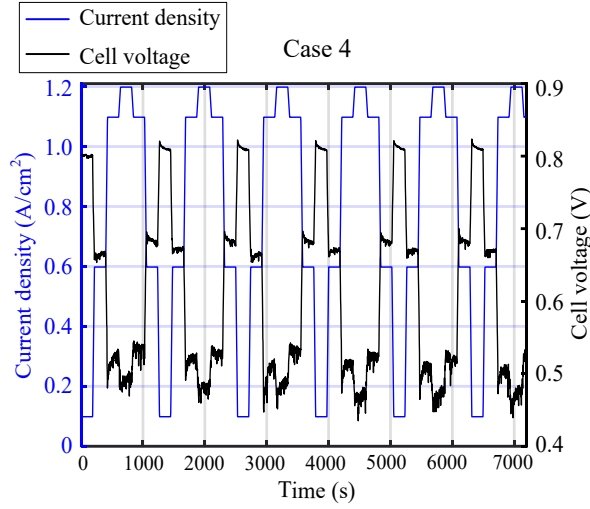


Figure 6-15: Case 4, ramp value $\Delta i = 0.5 \text{ A cm}^{-2}$ and ramp time $t_{in} = 60 \text{ s}$ (Blue line: current density profile; Black line: cell voltage collected from experiment; Operating condition: Table 6-II) [118].

The online adaptive model performance is then compared with other modeling methods that two references models are used. Reference model 1 is also called GA initialization model, which used genetic algorithm to find the initial parameters $\{\gamma_0, \sigma_0\}$, but skip the online updating process for the internal parameters. As the parameters in the GA initialization model are fixed, it could be used to verify the advantage of the online updating process for parameters $\{\gamma, \sigma\}$. Reference model 2 is called online updating model, in which the initial parameters $\{\gamma_0, \sigma_0\}$ are tuned manually based on cross validation instead of automatically by GA. After the initial parameters $\{\gamma_0, \sigma_0\}$ has been tuned manually, online updating process is employed to update these parameters $\{\gamma, \sigma\}$. As GA initialization has been skipped in the online updating model, it could be used to discuss the efficiency of finding a good start point for LSSVM method. The difference between the online adaptive model and the reference models are listed in Table 6-V.

Table 6-V: Properties of reference models in comparison with the proposed model.

	Genetic algorithm (GA)	Parameters updating $\{\gamma, \sigma\}$
Adaptive online model	√	√
GA initialization model	√	×
Online updating model	×	√

The coefficient of determination (R^2) and the mean absolute percentage error (MAPE) are employed as indexes to evaluate and compare the models' performance, which is defined as:

$$R^2 = 1 - \frac{\sum_{i=1}^N (y_i - \hat{y}_i)^2}{\sum_{i=1}^N (y_i - \bar{y}_i)^2} \quad (6-7)$$

$$\text{MAPE} = \frac{1}{N} \sum_{i=1}^N \frac{|y_i - \hat{y}_i|}{y_i} \times 100\% \quad (6-8)$$

\bar{y}_i is the average value of the experimental data, N the number of data point, here is 2400. R^2 ranges from 0 to 1, and a higher R^2 means a better model performance, and a lower MAPE represent a better model performance.

The coefficient of determination and MAPE of the adaptive online model, the GA initialization model and the online updating mode on four current profiles (Case 1, 2, 3, 4) are shown in Figure 6-16 and 6-17, respectively. Overall, the adaptive online model has better model performance than other models in four cases. When comparing the performance of the adaptive online model with the GA initialization model, it can be seen that the difference between red bar and blue bar is quite small in case 2 and 4, but obvious in case 1 and 3. It indicates that the online updating for the internal parameters increases the model's performance and is especially necessary when load changes are large. When comparing the performance of the adaptive online model and the online updating model, it can be found a large difference between red bar and black bar in all four cases, which indicates the searching of a good start point for the LSSVM method largely improves its model performance [118].

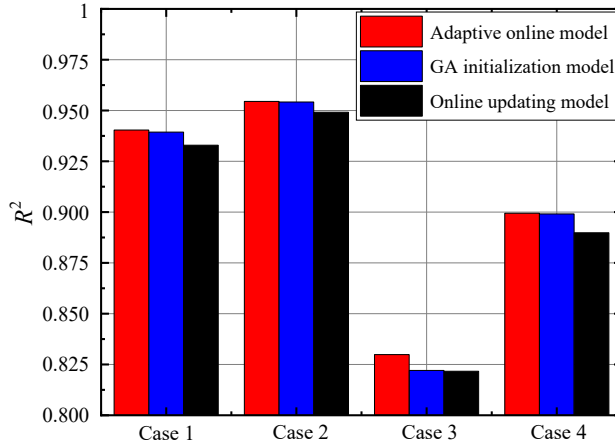


Figure 6-16: Coefficient of determination (R^2): higher value represents better model performance (Case 1: $t_{in} = 1$ s, $\Delta i = 0.2$ A cm⁻²; Case 2: $t_{in} = 60$ s, $\Delta i = 0.2$ A cm⁻²; Case 3: $t_{in} = 1$ s, $\Delta i = 0.5$ A cm⁻²; Case 4: $t_{in} = 60$ s, $\Delta i = 0.5$ A cm⁻²) [118].

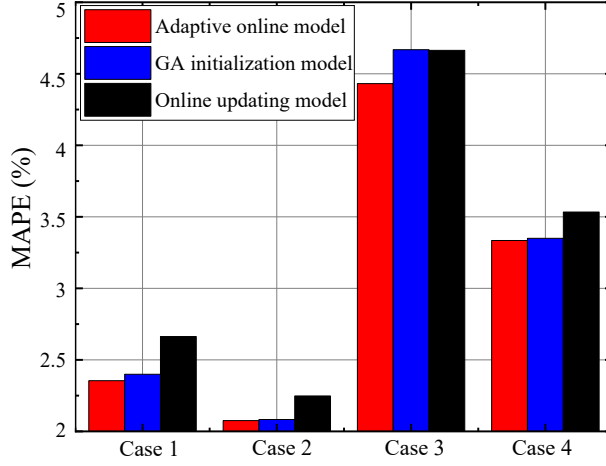


Figure 6-17: Mean absolute percentage error (MAPE): higher value represents poorer model performance (Case 1: $t_{in} = 1$ s, $\Delta i = 0.2$ A cm⁻²; Case 2: $t_{in} = 60$ s, $\Delta i = 0.2$ A cm⁻²; Case 3: $t_{in} = 1$ s, $\Delta i = 0.5$ A cm⁻²; Case 4: $t_{in} = 60$ s, $\Delta i = 0.5$ A cm⁻²) [118].

6.4.2 Validation based on artificial data

In this section, the artificial data generated in Chapter 5 is used to verify the online adaptive LSSVM model. Details of the artificial data can be found in section 5.1. 108 sets of artificial data are considered, including nine ramp values (listed in Table 5-V) and twelve ramp times (listed in Table 5-VI). The artificial data of each process were collected with sampling interval $\Delta t = 3$ s.

The online adaptive LSSVM is compared with the LSSVM model with the help of coefficient of determination (Eq. 6-7), as shown in Figure 6-18 and Figure 6-19 respectively. The colored lines in the figures represent different ramp values, the horizontal axis represents the ramp time, and the vertical axis represents the coefficient of determination. The improvement of the online adaptive LSSVM model to the LSSVM model is shown in Figure 6-20, which is obtained by the following equation:

$$\varpi = \frac{R_{online} - R_{original}}{1} \times 100\% \quad (6-9)$$

here, R_{online} is the modeling results (coefficient of determination in Figure 6-18) of the online adaptive model, $R_{original}$ is the modeling results (coefficient of determination in Figure 6-19) of the LSSVM model. 1 represents the maximum value of the coefficient of determination. A larger value in Figure 6-20 means a better improvement in model performance by using the online adaptive LSSVM model.

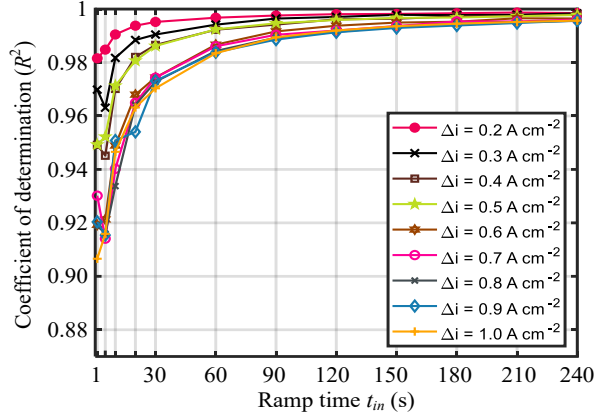


Figure 6-18: Coefficient of determination (R^2) of the online adaptive LSSVM model: with oscillated artificial data collected by sampling interval $\Delta t = 3$ s.

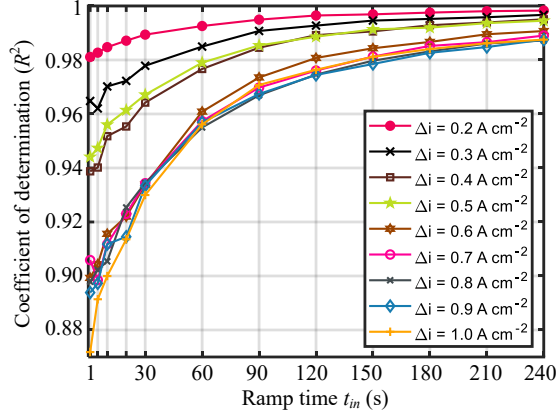


Figure 6-19: Coefficient of determination (R^2) of the LSSVM model: with oscillated artificial data collected by sampling interval $\Delta t = 3$ s.

It can be found that compared with the values in Figure 6-19, the values in Figure 6-18 are more likely to approximate a value of one, which indicates that the performance of the online adaptive model is better than LSSVM model. When the ramp time is small, for example $t_{in} \leq 30$ s, the modeling performance is significantly improved by using the online adaptive model, because the values in Figure 6-20 when $t_{in} \leq 30$ s are basically greater than the values when $t_{in} > 30$ s. In addition, it can be found that when the ramp time becomes large ($t_{in} > 180$ s), the improvement of the online adaptive online model becomes small, and seems like to be flat and no longer decrease. It indicates that with large ramp time that meaning smooth load change, using the online adaptive model will not greatly improve the modeling accuracy. This conclusion can be validated by the red-dot line in Figure 6-20, of which the ramp value is $\Delta i =$

0.2 A cm^{-2} . Small ramp value means smooth load change as well. It can be found that in Figure 6-20, the corresponding y -axis of the red-dot line is relatively small when compared with the rest lines.

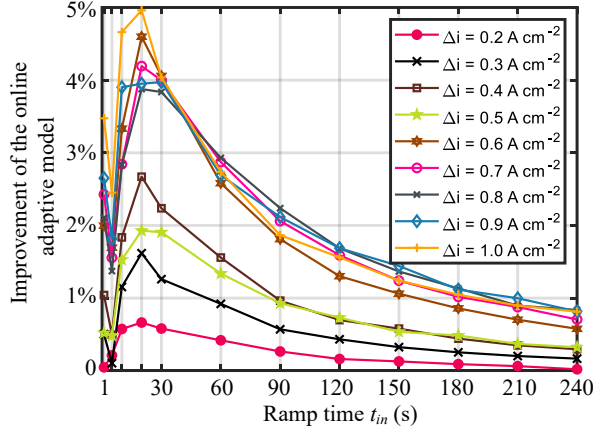


Figure 6-20: Improvement of the online adaptive model (Eq. 6-9).

There is an obvious gap in Figure 6-20. The colored lines at the top of Figure 6-20 can be grouped as high ramp value group (group 1: $\Delta i \geq 0.6 \text{ A cm}^{-2}$), and the colored lines at the bottom of Figure 6-20 are then grouped as low ramp value group (group 2: $\Delta i \leq 0.5 \text{ A cm}^{-2}$). Considering the value in group 1 is larger than that of in group 2, it can be concluded that the improvement in modeling accuracy is more obvious when dealing with more severe load changes. In other words, it is more necessary to use the online adaptive model when the load change is more drastically

In summary, the online adaptive model has an overall improvement in modeling accuracy. The online adaptive can improve the modeling accuracy by up to 5%. The improvement is more obvious when the load changes drastically.

6.5 Conclusions

In this chapter, an adaptive online model for polymer electrolyte fuel cell was developed, which is based on the least squares support vector (LSSVM). The internal parameters in the LSSVM is first tuned automatically then updated in real-time. The genetic algorithm was used to find initial parameters of the model by using pre-existing data from the previous experiments. Then, the initial parameters are used to establish the first sub-LSSVM model for the fuel cell transient voltage. The gradient method was used to update the internal parameters online. The whole process was divided into several sub-sections over time. The internal parameters have been updated in each sub-model and forwarded to the next sub-model.

The efficiency of the adaptive online model had been validated by comparing with the experimental data collected from the test rig. The results indicate that the proposed model has a good approximation ability and high model accuracy in modeling fuel cell transient voltage. When comparing the adaptive online model with other models, the necessity of finding the initial internal parameters and online updating these parameters is confirmed. The superiority of using genetic algorithm to automatically tune the parameters is obvious, because the model's performance is significantly improved when the genetic algorithm was applied. In addition, the advantage of online updating model's internal parameters is also confirmed by the high determination of coefficient and low MAPE of the modeling results from the adaptive online model when comparing with the GA initialization model.

The improvement of the online adaptive model to the LSSVM model in modeling accuracy was confirmed by using the artificial data generated in chapter 5. The modeling accuracy was improved by up to 5%. The results show that the online adaptive model improves the modeling accuracy more obvious when drastic load changes are applied to the fuel cell.

7 Discussions

The purpose of this thesis was to apply the machine learning in modeling of the dynamics of the PEFC. This chapter includes a discussion of major findings as related to the establishment of the LSSVM model to predict the dynamic behaviors of the PEFC, identification of the credibility and limitation of the model, and modify the model in order to improve its modeling accuracy. The chapter concludes with a discussion of the limitations of the study, areas for future research and a brief summary.

This chapter contains discussion and future research possibilities to help answer the research questions:

- What is the limitation of the LSSVM method when modeling and predicting the dynamic behaviors of the PEFCs?
- How does the load change affect the performance of the LSSVM model?
- How to regulate the system's setup and load changes in order to ensure a satisfactory modeling accuracy of LSSVM model?
- How to improve the modeling accuracy when LSSVM method is used?

The limitation of the LSSVM method is comprised of two themes in this study: a) idealized cases and b) oscillated cases. Both are with the help of artificial data generated by a white-box model that followed the physical and electrochemical law of the fuel cells. One relates primarily to the theoretical operation of the PEFCs with determined output, which is commonly used to investigate the impacts of fuel cell parameters by models [121–123]. The other relates to the real operation of the PEFCs, in which the oscillation on the cell voltage was included. The oscillation in voltage exists commonly in the application of the PEFCs.

The results from both studies on the idealized cases indicate that a higher frequency sampling results in a better model performance. Four sampling intervals are considered, namely $\Delta t = 1$ s, 3 s, 5 s, 8 s. Large value of sampling interval, for example 8 s considered in the thesis, leads to incomplete information as sharp peak of the fuel cell dynamic behaviors would be missed. This results in poor modeling performance. Consistent conclusions can be drawn from Figure 4-14 and Table 5-IV, as the value of the sampling interval increases, the coefficient of determination of the LSSVM model results under the corresponding sampling interval decreases while the integrated error increases. In addition, the analysis on the LSSVM model's performance under load changes supports the theory that the LSSVM model can predict the cell voltage more precisely when smooth load change is applied. This result builds on existing evidence of identical conclusion drawn from Figure 4-18 and Figure 5-14 when the effects of ramp value on the performance of the LSSVM model, and from Figure 4-21 and Figure 5-17 when the effects of ramp time is discussed. As the ramp value increases, the integrated error and coefficient of determination trends of the two cases are very similar. A large difference in the

LSSVM modeling error is found when ramp value less than 0.5 A cm^{-2} and larger than 0.5 A cm^{-2} are applied to the fuel cell load, respectively. The LSSVM model's performance drops significantly when the ramp value increase from 0.5 A cm^{-2} to 0.6 A cm^{-2} , as the integrated error increased by 50% and the coefficient of determination decreased by 0.03-0.04. However, when the ramp value is larger than 0.5 A cm^{-2} , and then continue to increase the ramp value, the performance of the LSSVM model does not change much. The results indicate that the ramp value $\Delta i = 0.5 \text{ A cm}^{-2}$ could be regarded as a turning point. Although the performance of the model when the ramp value Δi is greater than 0.5 A cm^{-2} is worse than when it is less than 0.5 A cm^{-2} , the LSSVM model performance is still very good overall, however, thoughtful decision should be given if a larger ramp value is applied to the fuel cell load. The performance of the LSSVM model under the two cases shares similar trend when the effects of the ramp time are discussed. As the ramp time increases, the integrated error decreases and the coefficient of determination increase. When the ramp time is less than 30 s, slightly increase the ramp time, the performance of the LSSVM model will be significantly improved. The longer the ramp time, for example $\Delta t > 120 \text{ s}$, the increase in ramp time will not significantly improve the LSSVM model's performance.

The combined effects of the sampling interval, ramp value and ramp time are discussed in chapter 5. When higher frequency sampling is used to collect the data of the PEFCs during operation, as it provides detailed information of the PEFCs to the LSSVM model, the prediction of the model is more accurate than if low frequency sampling is considered. Also, when high frequency sampling is applied, the impacts of the load change on the model's performance become are smaller than that of when low frequency sampling is applied. As discussed in Figure 5-18, with sampling interval $\Delta t = 1 \text{ s}$, the coefficient of determination ranges from 0.930 to 0.999, but with $\Delta t = 8 \text{ s}$, this value ranges from 0.650 to 0.990. This result indicates that if the load variation of a PEFC changes drastically, a high frequency sampling should be considered to offset the impact of the drastic load change on the modeling performance of the LSSVM model. From Figure 5-18, the load change behavior can be classified into two types, smooth ramp change and sharp ramp change. The ramp values less than 0.5 A cm^{-2} are called smooth change and larger than 0.5 A cm^{-2} are called sharp change. When the fuel cell ramp value Δi exceeds 0.5 A cm^{-2} , the effect of ramp value on model performance becomes insignificant, as R^2 value of those processes are almost the same. This result is consistent with the previous conclusion.

Accuracy is the key to a model, and is commonly used to evaluate the fuel cell model. The models' accuracy have been discussed in many cases [86,124,125], but there discussed the model's accuracy only in one load behavior. However, in automotive application of the PEFCs, it often experience various load changes, such as sudden start-up, shut-down, idle speed, and acceleration [44]. In chapter 5, an investigation on the LSSVM model's accuracy under various

load variations was implemented. And a systematical way has been applied to analyze the performance of the LSSVM model; no similar works have been done before. The result suggest that no matter how strong approximation ability of a modeling method is, it is still necessary to identify the model's limitation in order to ensure that the anticipated modeling accuracy is achieved. In order to ensure the accuracy of the LSSVM model, a working zone for regulating the sampling interval, load changes were provided. It is easy to define the working zone when the anticipated modeling error or the maximum tolerable error is provided.

The improvement of the LSSVM model was presented in chapter 6 and comprised of two steps in this study: a) a genetic algorithm and b) gradient method. Parameters involved in the LSSVM method itself is initialized by a genetic algorithm, then, the parameters are updated online by gradient method. Kang et al. [94] and Acuña et al. [126] have used the genetic algorithm to tune the parameters for the LSSVM model. After the parameters were adjusted by the genetic algorithm, they are used in the LSSVM model for modeling and predicting. Despite the inaccuracy caused by manual adjustment of the parameters has been overcome by genetic algorithm, these tuned parameters remain fixed throughout the modeling process, which may not be optimal value over time. But the calculation time for running the genetic algorithm is quite long, which is not suitable for an operating fuel cell that requiring online modeling and prediction. Thus, the gradient method, which requires less calculation time, is used to realize online updating for the internal parameter set. Two parameters are involved in the LSSVM model. The results indicate that a suitable parameter set $\{\gamma, \sigma\}$ is of great importance in getting good model performance, and it can be realized by using genetic algorithm. Although online updating by gradient method can improve the model accuracy, it is important to choose suitable internal parameters as a starting point. In addition, the modeling performance of the online adaptive was test by oscillated artificial data generated in chapter 5. An improvement in model performance of the online adaptive LSSVM model was proved when comparing its modeling results with the LSSVM model, especially when drastic load changes were applied to the PEFCs. The online adaptive improves the modeling accuracy by up to 5% when comparing the LSSVM model established in chapter 3. This adaptive online model can also be applied to other research fields when model's internal parameters have large impact on the model performance and severe change of the system parameters is evitable to the system.

Further investigations on the machine learning in modeling of the dynamics of polymer electrolyte fuel cells are necessary. There are some challenges which have not been well studied in this work.

Due to the complexity of the fuel cells, different dynamic behavior is shown under different operating conditions and load changes. The analysis on the LSSVM model considered only one operating condition in this work. Under this operating condition, impacts of load changes were carried out. How the LSSVM model works in different operating conditions, namely relative

humidity, temperature and pressure, is a remaining problem. Generally speaking, more data at a wide range of operating conditions are needed.

White-box model is an efficient approach to provide data that needed for the investigation on the performance of the LSSVM model. Most of the existing white-box models can only work under some assumptions. How to get a detailed model that can describe the fuel cells very well and provide accurate data of the fuel cell is a challenge. The identification of the fuel cell system based on the mechanism in combination with experimental research is a promising approach.

Optimal experiment design (both to experiment in test station and numerical experiment in simulation) to obtain informative data is very important for parameter estimation and system approximation. The selection of the methods may be also included in this topic. Whether the method can be extended to other application is still an open question.

8 Conclusions

The studies of polymer electrolyte fuel cells (PEFCs) become more and more active and import because of clean energy needs in the industry. Nonlinear dynamics considered in the thesis is a crucial issue in the application of the PEFCs. Modeling is required by predicting, controlling and optimizing the PEFCs system. The complex characteristics, such as multi-physics coupling, nonlinearity, time-varying, unknown disturbances and various working conditions make the modeling of the fuel cell system difficult and challenging.

This thesis is focused on the dynamic modeling to the PEFCs system with the help of a data-driven method, and the performance of the data-driven method under various load changes are discussed based on the statistical analysis. The main attributions and conclusions made in this thesis are as following:

- An accurate and fast responsive model was established, which overcomes the complex nonlinear, time-varying properties in fuel cells. The model is based on the least squares support vector machine (LSSVM), which has the ability to approximate any nonlinear system by a simple model structure. With this model, the dynamic behavior of the PEFCs is described. Due to its fast reaction to the load change, it bridges the gap between complex physical phenomena and fast transient response;
- Artificial data was generated by a white-box model that follows physical and electrochemical laws. The artificial data were regarded as an alternative to experimental data, which is able to provide numerical data of fuel cells under sharp and extreme load changes that are prohibited by the fuel cells test rig and harmful to the fuel cells. Two types of artificial data were obtained: one is idealized artificial data that have been used to investigate the LSSVM model's performance under theoretical operation; another is oscillated artificial data with oscillations based on the analysis of fluctuations in experimental data.
- The effects of fuel cell system's setup (sampling interval) and exterior loads' properties (ramp time and ramp value) on the LSSVM model were thoroughly investigated. The results showed that a low frequency sampling lead to incomplete information because the sharp peak of the system would be missed, as consequence, causes poor modeling performance. And the LSSVM model performs well when a smooth load changes are applied, which means smaller change step of the current density and longer time for the current density change bring about better model performance, when the data used have same sampling interval;
- A working zone intended to ensure the LSSVM model's accuracy was presented. The working zone regulates the selection of sampling interval, ramp time and ramp value. Based on maximum absolute error and average absolute error that are acceptable by

the fuel cell system, a set of possible combination of sampling interval, ramp time and ramp value can be found from the working zone;

- An online adaptive LSSVM model was proposed in order to overcome the limitations of the LSSVM model in dealing with various load changes and unforeseen change in the fuel cell behavior over time. The proposed model used genetic algorithm to search the internal parameters of the model instead of manual selection, which avoids the model suffering from local minima. In addition, the internal parameters were updated online according to adjacent fuel cell system information, by which the effects of uncertainties and online disturbance on the LSSVM model's performance can be solved.

The effectiveness of the LSSVM model and the online adaptive model has been verified on our test rig. They have the following advantages: i). little process knowledge. They are data-driven modeling and do not require priori knowledge on the system; ii). simple nonlinear structure. They are mapping the original data from the primal space into the feature space with the help of kernel functions. As a consequence, the dimensionality is then largely reduced, which are suitable for the industry application. Besides, the online adaptive model has the advantage on the selection and optimization of the internal parameters, which was implemented by the combination of the genetic algorithm and gradient method.

Because almost no system knowledge is involved in the modeling process, the data used in the models play an important role in the models' modeling and predicting performance. Thus, sampling interval, which defines the level of detail of the system information obtained by the model, should be determined before running the fuel cell system. System with strong dynamic characteristics should consider high frequency sampling to obtain detailed information for the model in order to achieve desirable modeling performance. But high frequency sampling brings about the problem of storage and computation burden, thus, a tradeoff between economic and accuracy should be balanced.

The proposed online adaptive model makes it feasible to tune the hyper parameters of the LSSVM model from time by time to overcome unforeseen changes in the fuel cell characteristics.

Appendix

A.1 Workflow of the modeling process in chapter 3

The workflow of the modeling process in chapter 3 is shown in Figure A-1. The meaning of each icon used in the figure is shown in Table A-I. If same icon appears in the workflow, it means they represent the same thing. The arrow represents the direction of the process. Arrows with dash line mean that there is data transmission between the steps.

- Data collection: raw data is first collected from our test rig;
- Data analysis: during this step, raw data are processed into a readable form to the modeling software;
- Data filtering: the data that have a larger impact on the system are selected and preserved. Those filtered data are separated into two parts: one is called training data that are used to train the model and the other one is called testing data that are used to validate the model's efficiency;
- Modeling training: model is trained here;
- Model validation: the testing data are used here to validate the model, the model's accuracy will be judged with criteria. The criteria vary from different modeling purposes. If the model's accuracy satisfies the modeling requirement, then the model structure is determined and will be used to predict the system future behaviors; however, if the model's accuracy is not satisfactory, then the model needs to be retrained;
- Prediction: after the model structure is determined, the model is used to predict the behavior of the system. The model inputs are the same as the system input to the experiments.

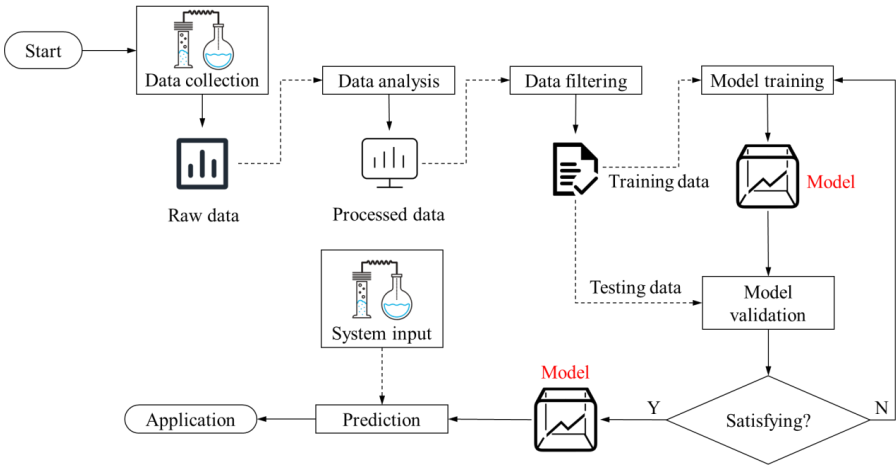







Figure A-1: Workflow of the LSSVM modeling process.

Table A-I: Icons in Figure A-1 and their meaning.

Icon	Meaning
	:represents experimental processes where the raw data coming from
	:represents raw data collected from experiments that may not be recognized by computer/processor/controller
	:represents processed data that could be read by computer/processor/controller
	:represents filtered data that will be employed to establish model and validate the model; those data are separated into two parts: training data and testing data
	:represents the model

A.2 Workflow of the modeling process in chapter 4

The workflow for chapter 4 is shown in Figure A-2. The meaning of each icon used in the figure is shown in Table A-II. The arrow represents the direction of the process. Arrows with dash line mean that there is data transmission between the steps.

Data collection: artificial data are generated by Simulink simulation. Large amount of artificial data that cover various load changes are generated;

Data analysis: during this step, artificial data were processed into a readable form to the modeling software;

Data filtering: the data that have a greater impact on the system were selected and preserved. Those filtered data are regarded as the model input;

Modeling results: The model used here is the trained model in chapter 3, and artificial data are used here. The model predicts the corresponding output based on different inputs, and the prediction values are evaluated by comparing with the artificial data;

Results analysis: the predicted outputs are compared with the data that generated by the Simulink simulation and analysis on those modeling results are carried out.

System input: the analysis will be used to regulate the system input in order to maintain a reliable forecasting result by the model.

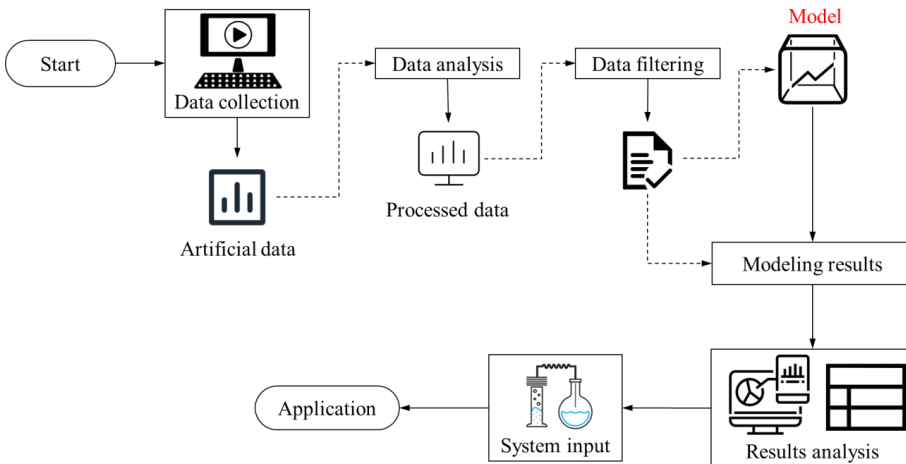









Figure A-2: Workflow of the suitability analysis on the LSSVM model (ideal cases).

Table A-II: Icons in Figure A-2 and their meaning.

Icon	Meaning
	: represents Simulink process where the artificial data are generated
	: represents artificial data generated by Simulink simulation
	: represents processed data that could be read by computer/processor/controller
	: represents filtered data that have a greater impact on the system
	: represents the model, which has been determined in the chapter 3
	: represents the analysis process on the modeling results
	: represents experimental processes where the raw data coming from

A.3 White-box model for generating artificial data

A.3.1 Voltage module

The theoretical fuel cell potential is calculated corresponding to Gibbs free energy, as follows:

$$E = -\frac{\Delta G}{nF} + \frac{RT}{nF} \ln \left(\frac{p_{H_2} p_{O_2}^{0.5}}{p_{H_2O}} \right) \quad (A-1)$$

$$\Delta G = \Delta H - T\Delta S \quad (A-2)$$

here, ΔG is the Gibbs free energy, ΔH is the difference between the heats of formation of products and reactants, and ΔS is the difference between entropies of products and reactants, n is the number of electrons per molecule of reactant, F is Faraday's Constant (96485 C mol^{-1}), R is the universal gas constant ($8.31 \text{ J kg}^{-1} \text{ K}^{-1}$), T is the temperature (K) and p_{H_2} , p_{O_2} and p_{H_2O} are the partial pressure of hydrogen, oxygen and vapor, respectively.

However, in practice the cell potential is always lower than the theoretical potential, as there are many kinds of voltage losses in a fuel cell. Three main voltage losses are considered here, namely activation loss, ohmic loss and concentration loss. At low current densities, the main loss in the fuel cell is the activation loss, which is due to sluggish electrode kinetics. This loss occurred on both sides, but a much slower reaction was on the cathode side; therefore, only the cathode side is considered in this model. The Ohmic loss is caused by the resistance to ion transportation in the electrolyte and electrons transferring through the conductive. Moreover, the concentration loss is caused by the limitation of mass transport. Thus, the cell voltage can be expressed as follows:

$$V_{cell} = E - \Delta V_{act} - \Delta V_{ohmic} - \Delta V_{conc} \quad (A-3)$$

here, E is the theoretical potential Eq. A-1, which is largely depend on the temperature and pressure, ΔV_{act} is activation loss, ΔV_{ohmic} the ohmic loss and ΔV_{conc} the concentration loss.

Activation loss occurs on both sides. Due to a much faster electrochemical reaction on the anode side, only the cathode side is considered here. The Tafel equation is used to calculate the activation loss

$$\Delta V_{act} = a + b \ln(i) \quad (A-4)$$

where i is the current density. a and b for the white-box model were obtained by fitting the experimental data collected from our test rig. $a = 0.2267$ and $b = 0.0298$.

The Ohmic can be expressed as:

$$\Delta V_{ohm} = I(R_i + R_e + R_c) \quad (A-5)$$

where I is the current, R_i is the ionic resistance, R_e is the electronic resistance and R_c is the contact loss. Electronic resistance is neglected here, and so the membrane resistivity can be expressed as [127]:

$$R_{resis} = \frac{r_m}{A} \cdot L \quad (A-6)$$

where L is the thickness of the membrane ($L = 178 \times 10^{-6}$ m), here the Nafion membrane is considered [109]. A is the active area (1.746×10^{-3} cm²) and r_m (Ω cm) is the specific resistivity for the flow of hydrated protons, which can be calculated as [128]:

$$r_m = \frac{181.6 \left(0.03 \frac{I}{A} + 1 + 0.062 \left(\frac{T}{303} \right)^2 \left(\frac{I}{A} \right)^{2.5} \right)}{\left(\lambda_m - 0.634 - 3 \frac{I}{A} \right) \cdot e^{4.18 \frac{(T-303)}{T}}} \quad (\text{A-7})$$

where λ_m is the membrane water content, which is a function of water vapor activity, the details of which are described in the membrane model section.

The concentration loss increases when the reactant is rapidly consumed, so that the concentration gradients appear. This causes a sharp drop in voltage at high current density, with the calculation given as:

$$\Delta V_{conc} = \frac{RT}{nF} \ln \left(\frac{i_{max}}{i_{max} - i} \right) \quad (\text{A-8})$$

The concentration loss increases when the reactant is rapidly consumed, so that the concentration gradients appear. This causes a sharp drop in voltage at high current density. i_{max} is the limiting current density, here $i_{max} = 1.22$ A cm⁻².

A.3.2 Anode module

Mass conservation principle is employed to establish the anode module, $\sum(\dot{m}_i)_{in} = \sum(\dot{m}_i) + \sum(\dot{m}_i)_{out}$. Pure hydrogen is delivered to the anode side, and before it entering the fuel cell, it will be humidified. Then, the states of hydrogen and water are as follows:

$$\frac{dm_{H_2}}{dt} = \dot{m}_{H_2,in} - \dot{m}_{H_2,used} - \dot{m}_{H_2,out} \quad (\text{A-9})$$

$$\frac{dm_{H_2O,an}}{dt} = \dot{m}_{H_2O,an,in} - \dot{m}_{H_2O,mbr} - \dot{m}_{H_2O,an,out} - \dot{m}_{H_2O,an,l} \quad (\text{A-10})$$

where m_{H_2} is the mass of hydrogen inside the fuel cell, $\dot{m}_{H_2,in}$ is the mass flow of hydrogen at inlet, $\dot{m}_{H_2,used}$ is the consumption rate of hydrogen during the electrochemical reaction, $\dot{m}_{H_2,out}$ is the hydrogen mass flow at outlet, $m_{H_2O,an}$ is the mass of water on the anode side, $\dot{m}_{H_2O,an,in}$ is the water mass flow at inlet, $\dot{m}_{H_2O,mbr}$ is the mass flow rate of water transport through the membrane, $\dot{m}_{H_2O,an,out}$ is the outlet mass flow of water, $\dot{m}_{H_2O,an,l}$ is the liquid water flow rate; the mass of each gas has units of kg, and all flow rates have units of kg s⁻¹.

The consumption rate of hydrogen is determined by Faraday's Law:

$$\dot{m}_{H_2,used} = M_{H_2} \frac{I}{2F} \quad (\text{A-11})$$

where M_{H_2} is the molar mass of hydrogen, 0.002 kg mol⁻¹;

The flow rate of hydrogen and water leaving the anode side can be calculated by:

$$\dot{m}_{H_2,out} = \frac{1}{1 + \omega_{an,out}} \dot{m}_{an,out} \quad (\text{A-12})$$

$$\dot{m}_{H_2O,an,out} = \dot{m}_{an,out} - \dot{m}_{H_2,out} \quad (\text{A-13})$$

The calculations of hydrogen and water mass are used to compute the partial pressure of the substance existing on the anode side. The ideal gas law is applied:

$$pV = nRT \quad (\text{A-14})$$

Hydrogen partial pressure:

$$p_{H_2} = \frac{m_{H_2}}{M_{H_2}} \frac{RT}{V_{an}} \quad (\text{A-15})$$

Vapor partial pressure at anode side:

$$p_{v,an} = \frac{m_{H_2O,an}}{M_v} \frac{RT}{V_{an}} \quad (\text{A-16})$$

The humidity ratio is then:

$$\omega_{an,out} = \frac{M_v}{M_{H_2}} \frac{p_{v,an}}{p_{H_2}} \quad (\text{A-17})$$

where M_v is the molar mass of vapor, $0.018 \text{ kg mol}^{-1}$.

Water transport through the membrane $\dot{m}_{H_2O,mbr}$, is introduced in the membrane module, details of which can be found in section A.3.4. The temperature is assumed to be perfectly controlled as a constant, $T = 343.15 \text{ K}$.

A.3.3 Cathode module

The mass conservation law is also used to construct the cathode module. Here assumed that air is delivered to the cathode side as oxidant, thus, the mass balance of oxygen, nitrogen and water are considered. Water flow across the membrane will be introduced later, in section A.3.4. The states of oxygen, water and nitrogen are as follows:

$$\frac{dm_{O_2}}{dt} = \dot{m}_{O_2,in} - \dot{m}_{O_2,used} - \dot{m}_{O_2,out} \quad (\text{A-18})$$

$$\frac{dm_{H_2O,ca}}{dt} = \dot{m}_{H_2O,ca,in} + \dot{m}_{H_2O,gen} + \dot{m}_{H_2O,mbr} - \dot{m}_{H_2O,ca,out} - \dot{m}_{H_2O,ca,l} \quad (\text{A-19})$$

$$\frac{dm_{N_2}}{dt} = \dot{m}_{N_2,in} - \dot{m}_{N_2,out} \quad (\text{A-20})$$

where m_{O_2} is the mass of oxygen inside the fuel cell, $\dot{m}_{O_2,in}$ the mass flow of oxygen at inlet, $\dot{m}_{O_2,used}$ is the consumption rate of oxygen, $\dot{m}_{O_2,out}$ is the mass flow of oxygen leaving the fuel cell, $m_{H_2O,ca}$ is the water mass in the cathode side, $\dot{m}_{H_2O,ca,in}$ is the mass flow of water at inlet of the cathode side, $\dot{m}_{H_2O,gen}$ is the rate of water generated during the electrochemical reaction, $\dot{m}_{H_2O,ca,out}$ is the mass flow of water leaving the cathode side, $\dot{m}_{H_2O,ca,l}$ is the liquid water flow rate on the cathode side, m_{N_2} is the mass of nitrogen inside the fuel cell, $\dot{m}_{N_2,in}$ the nitrogen mass flow rate at inlet, $\dot{m}_{N_2,out}$ the nitrogen mass flow rate leaving the fuel cell.

The consumption of hydrogen is:

$$\dot{m}_{O_2,used} = M_{O_2} \frac{I}{4F} \quad (\text{A-21})$$

The water generated on the cathode side is:

$$\dot{m}_{H_2O,gen} = M_v \frac{I}{2F} \quad (\text{A-22})$$

Oxygen partial pressure:

$$p_{O_2} = \frac{m_{O_2} RT}{M_{O_2} V_{ca}} \quad (A-23)$$

Vapor partial pressure on the cathode side:

$$p_{v,ca} = \frac{m_{H_2O,ca} RT}{M_v V_{ca}} \quad (A-24)$$

Nitrogen partial pressure:

$$p_{N_2} = \frac{m_{N_2} RT}{M_{N_2} V_{ca}} \quad (A-25)$$

where M_{N_2} is the molar mass of nitrogen ($0.028 \text{ kg mol}^{-1}$);

The humidity ratio is then:

$$\omega_{ca,out} = \frac{M_{v,ca}}{M_{dry,ca,out}} \frac{p_{v,ca}}{p_{dry,ca,out}} \quad (A-26)$$

where $p_{dry,ca,out}$ is the partial pressure of dry gas on the cathode side and $M_{dry,ca,out}$ is the molar mass of dry gas.

$$p_{dry,ca,out} = p_{O_2} + p_{N_2} \quad (A-27)$$

$$M_{dry,ca,out} = y_{O_2,dry} \times M_{O_2} + (1 - y_{O_2,dry}) \times M_{N_2} \quad (A-28)$$

The flow rate of oxygen and water leaving the cathode side can be calculated by:

$$\dot{m}_{dry,out} = \frac{1}{1 + \omega_{ca,out}} \dot{m}_{ca,out} \quad (A-29)$$

$$\dot{m}_{O_2,out} = x_{O_2,dry} \dot{m}_{dry,out} \quad (A-30)$$

$$x_{O_2,dry} = \frac{y_{O_2,dry} \times M_{O_2}}{y_{O_2,dry} \times M_{O_2} + (1 - y_{O_2,dry}) \times M_{N_2}} \quad (A-31)$$

$$y_{O_2,dry} = \frac{p_{O_2}}{p_{N_2} + p_{O_2}} \quad (A-32)$$

A.3.4 Membrane module

Water transport through the membrane is a function of the current density and the relative humidity at the anode and cathode sides. There are two forms of water transport through the membrane: electro-osmotic drag ($N_{v,osmotic}$ ($\text{mol s}^{-1} \text{ cm}^{-2}$)) and back diffusion ($N_{v,diff}$ ($\text{mol s}^{-1} \text{ cm}^{-2}$)). Then, the water transport through the membrane can be described as [129]:

$$N_{v,membr} = N_{v,osmotic} - N_{v,diff} \quad (A-33)$$

where the positive direction is defined from the anode to cathode.

Electro-osmotic drag is attributed to the proton across the membrane from the anode to the cathode accompanied with water molecules dragged. It can be calculated by:

$$N_{v,osmotic} = n_d \frac{i}{F} \quad (A-34)$$

here, n_d is the electro-osmotic drag coefficient, as following [130]:

$$n_d = 0.0029 \lambda_m^2 + 0.05 \lambda_m - 3.4 \times 10^{-19} \quad (A-35)$$

where λ_m is the membrane water content that is a function of the water vapor activity:

$$\lambda_x = \begin{cases} 0.0443 + 17.81a_x + 39.85a_x^2 + 36a_x^3, & a_x \leq 1 \\ 1.4(a_x - 1) + 14 & \text{else} \end{cases} \quad (\text{A-36})$$

where x stands for an , ca and m , which represent the anode, cathode and membrane. a_x is water vapor activity, which is:

$$a_{an} = \frac{p_{v,an}}{p_{sat,an}} \quad (\text{A-37})$$

$$a_{ca} = \frac{p_{v,ca}}{p_{sat,ca}} \quad (\text{A-38})$$

$$a_m = \frac{1}{2}(a_{an} + a_{ca}) \quad (\text{A-39})$$

The back diffusion is caused by a gradient of water concentration across the membrane, which is expressed as:

$$N_{v,diff} = D_w \frac{dc_v}{dy} \quad (\text{A-40})$$

here D_w is the diffusion coefficient, c_v is the water concentration and y is the distance of the water transport through the membrane. Only linear function is considered here, $N_{v,diff} = D_w \frac{c_{v,ca} - c_{v,ca}}{t_m}$.

The diffusion coefficient is:

$$D_w = D_\lambda \cdot e^{2416(\frac{1}{303} - \frac{1}{T})} \quad (\text{A-41})$$

where:

$$D_\lambda = \begin{cases} 10^{-6} & \lambda_m < 2 \\ (1 + 2(\lambda_m - 2)) \times 10^{-6} & 2 \leq \lambda_m \leq 3 \\ (3 - 1.67(\lambda_m - 3)) \times 10^{-6} & 3 < \lambda_m < 4.5 \\ 1.25 \times 10^{-6} & \text{else} \end{cases} \quad (\text{A-42})$$

The water concentration is:

$$c_{v,x} = \frac{\rho_{m,dry}}{M_{m,dry}} \lambda_x \quad (\text{A-43})$$

here, $\rho_{m,dry}$ is the membrane density (kg m^{-3}), $M_{m,dry}$ is the molecular weight of membrane (kg mol^{-1}).

The mass flow rate of water across the membrane is:

$$\dot{m}_{H_2O,mbr} = N_{v,memvr} \cdot M_{H_2O} \cdot A \quad (\text{A-44})$$

Combining equations from A-33 to A-44, the mass flow transport through the membrane is then calculated.

A.4 Workflow of the modeling process in chapter 5

The workflow of the modeling process in chapter 5 is shown in Figure A-3. The meaning of each icon used in the figure is shown in Table A-III. The arrow represents the direction of the process. Arrows with dash line mean that there is data transmission between the steps.

Historical data: historical data collected from our test rig were retrieved, and then the oscillations on the cell voltage are analyzed;

Data analysis: statistical analysis on the oscillation on cell voltage is carried out;

Data collection: statistical results were combined with the Simulink simulation. Then, bunches of raw data that cover various load changes were generated, where the oscillation on the cell voltage is considered;

Data analysis: during this step, artificial data were processed into a readable form to the modeling software;

Data filtering: the data that have a greater impact on the system were selected and preserved. Those filtered data are regarded as the model input;

Modeling results: The model used here is the trained model in chapter 3, and artificial data considered oscillation are used here. The model predicts the corresponding output based on different inputs, and the prediction values are evaluated by comparing with the artificial data;

Results analysis: the predicted outputs are compared with the data that generated by the Simulink simulation and analysis on those modeling results are carried out.

System input: the analysis will be used to regulate the system input in order to maintain a reliable forecasting result by the model.

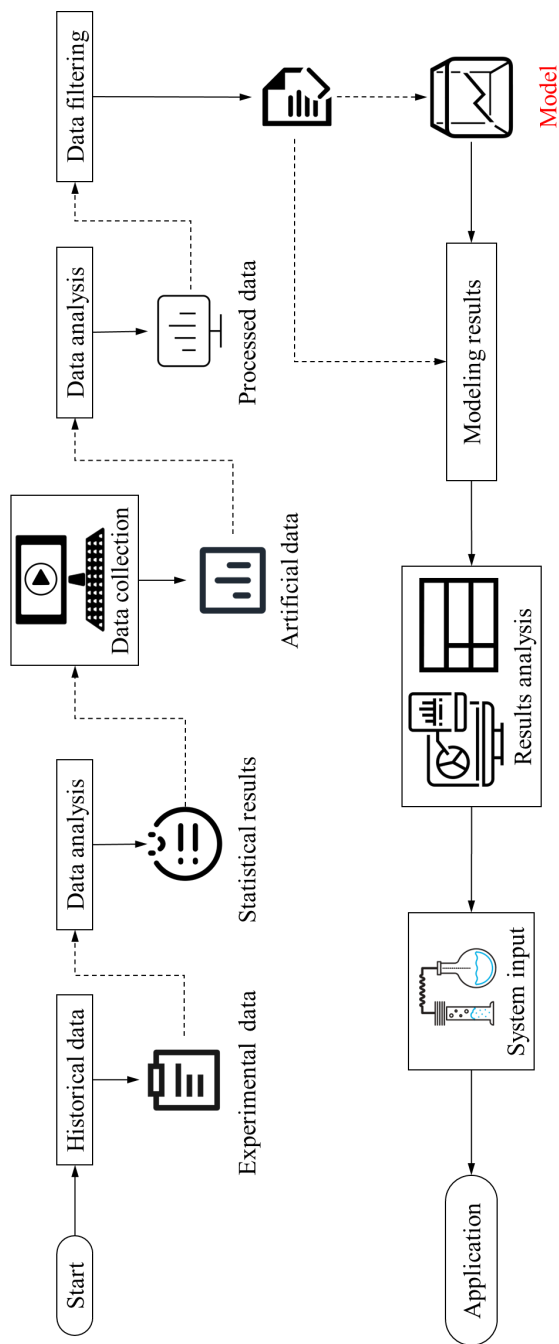











Figure A-3: Workflow of the suitability analysis on the LSSVM model (oscillation included cases).

Table A-III Icons in Figure A-3 and their meaning.

Icon	Meaning
	:represents data collected from experiments
	: represents statistical results on the historical data
	: represents Simulink process where the artificial data are generated
	:represents data collected from experiments or generated by Simulink simulation
	:represents processed data that could be read by computer/processor/controller
	:represents filtered data that have a greater impact on the system
	:represents the model, which has been determined in the chapter 3
	:represents the analysis process on the modeling results
	:represents experimental processes where the raw data coming from

A.5 Workflow of the modeling process in chapter 6

An online adaptive model is developed in chapter 6. The workflow of the modeling process in chapter 6 is shown in Figure A-4. The meaning of each icon used in the figure is shown in Table A-IV. The arrow represents the direction of the process. Arrows with dash line mean that there is data transmission between the steps.

Historical data: historical data collected from our test rig were retrieved;

Genetic algorithm: this gray-box method is used to find optimal parameters for the model;

Data collection: raw data is first collected from our test rig;

Data analysis: during this step, raw data are processed into a readable form to the modeling software;

Data filtering: the data that have a higher impact on the system are selected and preserved. Those filtered data are separated into two parts: one is called training data that are used to train the model and the other one is called testing data that are used to validate the model's efficiency;

Modeling training: model is trained here;

Model validation: the testing data are used here to validate the model, the model's accuracy will be judged with criteria that vary from different modeling purposes. If the model's accuracy satisfies the modeling requirement, then the model structure is determined and will be used to predict the system future behaviors; however, if the model's accuracy is not satisfactory, then the model needs to be retrained;

Prediction: after the model structure is determined, the model is used to predict the behavior of the system. The model inputs are the same as the system input to the experiments.

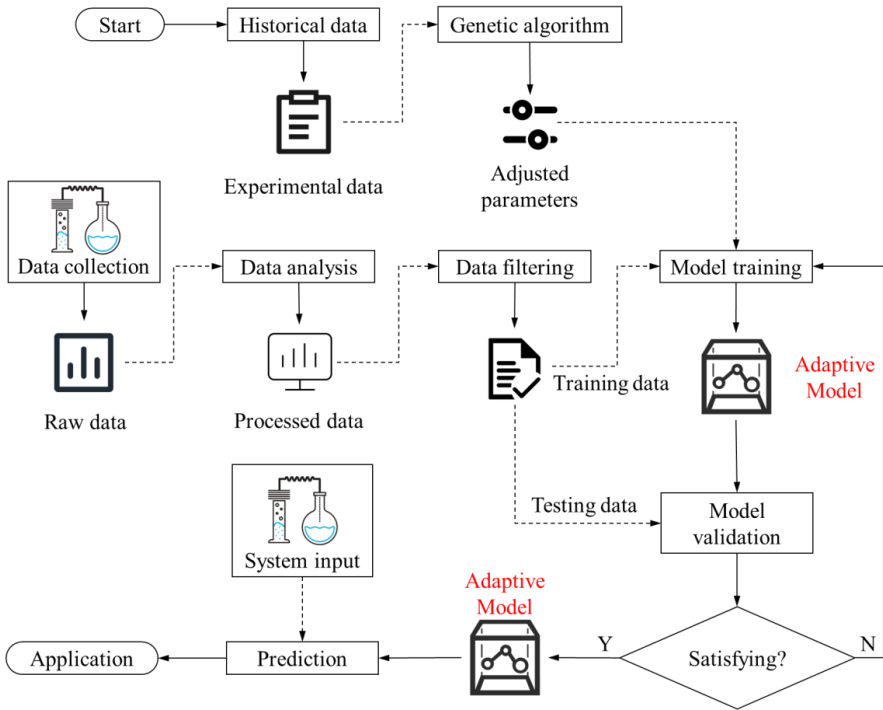


Figure A-4: Workflow of the online adaptive model (chapter 6).

Reference

- [1] Smil V. Energy transitions: global and national perspectives. Praeger; 2017.
- [2] Shindell D, Smith CJ. Climate and air-quality benefits of a realistic phase-out of fossil fuels. *Nature* 2019;573:408–11.
- [3] Eriksson ELV, Gray EMA. Optimization and integration of hybrid renewable energy hydrogen fuel cell energy systems – A critical review. *Appl Energy* 2017;202:348–64.
- [4] Kirubakaran A, Jain S, Nema RK. A review on fuel cell technologies and power electronic interface. *Renew Sustain Energy Rev* 2009;13:2430–40.
- [5] Barbir F. PEM Fuel Cells: Theory and Practice. Elsevier Inc.; 2005.
- [6] Kim M-E, Sohn Y-J. Study on polymer electrolyte fuel cells with nonhumidification using metal foam in dead-ended operation. *Energies* 2020;13.
- [7] Pratt JW, Klebanoff LE, Munoz-Ramos K, Akhil AA, Curgus DB, Schenkman BL. Proton exchange membrane fuel cells for electrical power generation on-board commercial airplanes. *Appl Energy* 2013;101:776–96.
- [8] Wang Y, Chen KS, Mishler J, Cho SC, Adroher XC. A review of polymer electrolyte membrane fuel cells: Technology, applications, and needs on fundamental research. *Appl Energy* 2011;88:981–1007.
- [9] Santangelo PE, Tartarini P. Effects of load variation and purge cycles on the efficiency of Polymer Electrolyte Membrane Fuel Cells for stationary applications. *J Renew Sustain Energy* 2018;10.
- [10] Xu L, Reimer U, Li J, Huang H, Hu Z, Jiang H, et al. Design of durability test protocol for vehicular fuel cell systems operated in power-follow mode based on statistical results of on-road data. *J Power Sources* 2018;377:59–69.
- [11] Sanchez DG, Ruiu T, Friedrich KA, Sanchez-Monreal J, Vera M. Analysis of the Influence of Temperature and Gas Humidity on the Performance Stability of Polymer Electrolyte Membrane Fuel Cells. *J Electrochem Soc* 2016;163:F150–9.
- [12] Li X. Principles of fuel cells. CRC Press; 2005.
- [13] Cho EA, Jeon US, Hong SA, Oh IH, Kang SG. Performance of a 1 kW-class PEMFC stack using TiN-coated 316 stainless steel bipolar plates. *J Power Sources* 2005;142:177–83.
- [14] Lee KH, Lee SH, Kim JH, Lee YY, Kim YH, Kim MC, et al. Effects of thermal oxidation on the corrosion resistance and electrical conductivity of 446M stainless steel for PEMFC bipolar plates. *Int J Hydrogen Energy* 2009;34:1515–21.
- [15] Andersson M, Beale SB, Espinoza M, Wu Z, Lehnert W. A review of cell-scale multiphase flow modeling, including water management, in polymer electrolyte fuel cells. *Appl Energy* 2016;180:757–78.
- [16] Cindrella L, Kannan AM, Lin JF, Saminathan K, Ho Y, Lin CW, et al. Gas diffusion layer for proton exchange membrane fuel cells-A review. *J Power Sources* 2009;194:146–60.
- [17] Loo KH, Wong KH, Tan SC, Lai YM, Tse CK. Characterization of the dynamic response of proton exchange membrane fuel cells - A numerical study. *Int J Hydrogen Energy* 2010;35:11861–77.
- [18] Tang Y, Yuan W, Pan M, Li Z, Chen G, Li Y. Experimental investigation of dynamic performance and transient responses of a kW-class PEM fuel cell stack under various load changes. *Appl Energy* 2010;87:1410–7.
- [19] Pei P, Chen H. Main factors affecting the lifetime of Proton Exchange Membrane fuel cells in vehicle applications: A review. *Appl Energy* 2014;125:60–75.
- [20] Matraji I, Laghrouche S, Jemei S, Wack M. Robust control of the PEM fuel cell air-feed system via sub-optimal second order sliding mode. *Appl Energy* 2013;104:945–57.
- [21] Ramos-Paja CA, Giral R, Martinez-Salamero L, Romano J, Romero A, Spagnuolo G. A PEM fuel-cell model featuring oxygen-excess-ratio estimation and power-electronics interaction. *IEEE Trans Ind Electron* 2010;57:1914–24.

- [22] Raj A, Shamim T. Investigation of the effect of multidimensionality in PEM fuel cells. *Energy Convers Manag* 2014;86:443–52.
- [23] Wang J. Theory and practice of flow field designs for fuel cell scaling-up: A critical review. *Appl Energy* 2015;157:640–63.
- [24] Liu D, Lin R, Feng B, Yang Z. Investigation of the effect of cathode stoichiometry of proton exchange membrane fuel cell using localized electrochemical impedance spectroscopy based on print circuit board. *Int J Hydrogen Energy* 2019;44:7564–73.
- [25] Liu J, Li Q, Chen W, Yan Y, Wang X. A fast fault diagnosis method of the PEMFC system based on extreme learning machine and dempster-shafer evidence theory. *IEEE Trans Transp Electrif* 2019;5:271–84.
- [26] Mert SO, Dincer I, Ozcelik Z. Exergoeconomic analysis of a vehicular PEM fuel cell system. *J Power Sources* 2007;165:244–52.
- [27] Saygili Y, Eroglu I, Kincal S. Model based temperature controller development for water cooled PEM fuel cell systems. *Int J Hydrogen Energy* 2015;40:615–22.
- [28] Yu S, Jung D. Thermal management strategy for a proton exchange membrane fuel cell system with a large active cell area. *Renew Energy* 2008;33:2540–8.
- [29] Wan Z, Shen J, Zhang H, Tu Z, Liu W. In situ temperature measurement in a 5 kW-class Proton Exchange Membrane Fuel Cell stack with pure oxygen as the oxidant. *Int J Heat Mass Transf* 2014;75:231–4.
- [30] Barbir F, Fuchs M, Husar A, Neutzler J. Design and operational characteristics of automotive PEM fuel cell stacks. *Fuel Cell Power Transp* 2000 2000;SAE SP-150.
- [31] Tsushima S, Hirai S. In situ diagnostics for water transport in proton exchange membrane fuel cells. *Prog Energy Combust Sci* 2011;37:204–20.
- [32] Cho J, Kim HS, Min K. Transient response of a unit proton-exchange membrane fuel cell under various operating conditions. *J Power Sources* 2008;185:118–28.
- [33] Yan X, Hou M, Sun L, Cheng H, Hong Y, Liang D, et al. The study on transient characteristic of proton exchange membrane fuel cell stack during dynamic loading. *J Power Sources* 2007;163:966–70.
- [34] Hsu CY, Weng FB, Su A, Wang C, Hussaini IS, Feng TL. Transient phenomenon of step switching for current or voltage in PEMFC. *Renew Energy* 2009;34:1979–85.
- [35] Silva RE, Gouriveau R, Jemei S, Hissel D, Boulon L, Agbossou K, et al. Proton exchange membrane fuel cell degradation prediction based on Adaptive Neuro-Fuzzy Inference Systems. *Int J Hydrogen Energy* 2014;39:11128–44.
- [36] Kheirandish A, Motlagh F, Shafiabady N, Dahari M, Khairi A, Wahab A. Dynamic fuzzy cognitive network approach for modelling and control of PEM fuel cell for power electric bicycle system. *Appl Energy* 2017;202:20–31.
- [37] Li S, Cao H, Yang Y. Data-driven simultaneous fault diagnosis for solid oxide fuel cell system using multi-label pattern identification. *J Power Sources* 2018;378:646–59.
- [38] Zeng T, Zhang C, Huang Z, Liu H, Chan SH, Chen J, et al. Fast identification of power change rate of PEM fuel cell based on data dimensionality reduction approach. *Int J Hydrogen Energy* 2019;44:21101–9.
- [39] Kheirandish A, Shafiabady N, Dahari M, Kazemi MS, Isa D. Modeling of commercial proton exchange membrane fuel cell using support vector machine. *Int J Hydrogen Energy* 2016;41:11351–8.
- [40] Suykens JAK, De Brabanter J, Lukas L, Vandewalle J. Weighted least squares support vector machines: robustness and sparse approximation. *Neurocomputing* 2002;48:85–105.
- [41] Cheng Y, Zerhouni N, Lu C. A prognostic framework for PEMFC based on least squares support vector regression-particle filter. 2017 IEEE Veh Power Propuls Conf VPPC 2017 - Proc 2018;2018-Janua:1–6.
- [42] Li X, Cao G, Zhu X. Modeling and control of PEMFC based on least squares support vector machines. *Energy Convers Manag* 2006;47:1032–50.
- [43] Li X, Han K, Song Y. Dynamic behaviors of PEM fuel cells under load changes. *Int J Hydrogen Energy* 2020;45:20312–20.

- [44] Zhao J, Jian Q, Luo L, Huang B, Cao S, Huang Z. Dynamic behavior study on voltage and temperature of proton exchange membrane fuel cells. *Appl Therm Eng* 2018;145:343–51.
- [45] Zendehboudi S, Rezaei N, Lohi A. Applications of hybrid models in chemical, petroleum, and energy systems: A systematic review. *Appl Energy* 2018;228:2539–66.
- [46] Na WK, Gou B. Feedback-linearization-based nonlinear control for PEM fuel cells. *IEEE Trans Energy Convers* 2008;23:179–90.
- [47] Chavan SL, Talange DB. Modeling and performance evaluation of PEM fuel cell by controlling its input parameters. *Energy* 2017;138:437–45.
- [48] Wang Y, Wang C. Transient analysis of polymer electrolyte fuel cells. *Electrochim Acta* 2005;50:1307–15.
- [49] Wang Y, Wang C. Dynamics of polymer electrolyte fuel cells undergoing load changes. *Electrochim Acta* 2006;51:3924–33.
- [50] Shan Y, Choe S-Y. A high dynamic PEM fuel cell model with temperature effects. *J Power Sources* 2005;145:30–9.
- [51] Shan Y, Choe S-Y. Modeling and simulation of a PEM fuel cell stack considering temperature effects. *J Power Sources* 2006;158:274–86.
- [52] Shan Y, Choe S-Y, Choi SH. Unsteady 2D PEM fuel cell modeling for a stack emphasizing thermal effects. *J Power Sources* 2007;165:196–209.
- [53] Liso V, Nielsen MP, Kær SK, Mortensen HH. Thermal modeling and temperature control of a PEM fuel cell system for forklift applications. *Int J Hydrogen Energy* 2014;39:8410–20.
- [54] Fly A, Thring RH. Temperature regulation in an evaporatively cooled proton exchange membrane fuel cell stack. *Int J Hydrogen Energy* 2015;40:11976–82.
- [55] Rakhtala SM, Shafiee Roudbari E. Fuzzy PID control of a stand-alone system based on PEM fuel cell. *Int J Electr Power Energy Syst* 2016;78:576–90.
- [56] Mahjoubi C, Olivier JC, Skander-mustapha S, Machmoum M, Slama-belkhdja I. An improved thermal control of open cathode proton exchange membrane fuel cell. *Int J Hydrogen Energy* 2019;44:11332–45.
- [57] Huangfu Y, Gao F, Abbas-Turki A, Bouquain D, Miraoui A. Transient dynamic and modeling parameter sensitivity analysis of 1D solid oxide fuel cell model. *Energy Convers Manag* 2013;71:172–85.
- [58] Pecht M, Kumar S. Data Analysis Approach for System Reliability, Diagnostics and Prognostics. *Pan Pacific Microelectron Symp* 2008:22–4.
- [59] Pecht MG. A prognostics and health management roadmap for information and electronics-rich systems. *Microelectron Reliab* 2010;50:317–23.
- [60] Panchal S. Artificial Neural Networks — Mapping the Human Brain. *Medium* 2018, <https://medium.com/predict/artificial-neural-networks-mapping-the-human-brain-2e0bd4a93160>, Web, 20.07.2020.
- [61] Aggarwal CC. *Neural Networks and Deep Learning*. Springer; 2018.
- [62] Makinde FA, Ako CT, Orodu OD, Asuquo IU. Prediction of crude oil viscosity using feed-forward back-propagation neural network (FFBPNN). *Pet Coal* 2012;54:120–31.
- [63] Silva IN da, Spatti DH, Flauzino RA, Liboni LHB, Alves SF dos R. *Artificial Neural Networks: A Practical Course*. Springer; 2017.
- [64] Barzegari MM, Rahgoshay SM, Mohammadpour L, Toghraie D. Performance prediction and analysis of a dead-end PEMFC stack using data-driven dynamic model. *Energy* 2019;188:116049.
- [65] Han I-S, Park SK, Chung CB. Modeling and operation optimization of a proton exchange membrane fuel cell system for maximum efficiency. *Energy Convers Manag* 2016;113:52–65.
- [66] James S. To stop the machines taking over we need to think about fuzzy logic. *Conversat* 2015, <https://theconversation.com/to-stop-the-machines-taking-over-we-need-to-think-about-fuzzy-logic-37961>, Web, 30.08.2020.
- [67] Zadeh LA. Fuzzy sets. *Inf Control* 1965;8:338–53.

- [68] Tanaka K, Wang HO. Fuzzy control systems design and analysis: A linear matrix inequality approach. John Wiley & Sons, Inc.; 2001.
- [69] Ata S, Dincer K. Fuzzy logic modeling of performance proton exchange membrane fuel cell with spin method coated with carbon nanotube. *Int J Hydrogen Energy* 2017;42:2626–35.
- [70] Baruch IS, Lopez RB, Guzman JO, Flores JM. A fuzzy-neural multi-model for nonlinear systems identification and control. *Fuzzy Sets Syst* 2008;159:2650–67.
- [71] Zhang T, Feng G. Rapid load following of an SOFC power system via stable fuzzy predictive tracking controller. *IEEE Trans Fuzzy Syst* 2009;17:357–71.
- [72] Entchev E, Yang L. Application of adaptive neuro-fuzzy inference system techniques and artificial neural networks to predict solid oxide fuel cell performance in residential microgeneration installation. *J Power Sources* 2007;170:122–9.
- [73] Furey TS, Cristianini N, Duffy N, Bednarski DW, Schummer M, Haussler D. Support vector machine classification and validation of cancer tissue samples using microarray expression data. *Bioinformatics* 2000;16:906–14.
- [74] Kecman V. Support Vector Machines – An Introduction. In: Wang L, editor. *Support Vector Mach. Theory Appl.*, Springer; 2005, p. 1–47.
- [75] Schölkopf B, Smola AJ. *Learning with kernels: Support vector machines, regularization, optimization and beyond*. The MIT Press; 2006.
- [76] Moghaddam VH, Hamidzadeh J. New Hermite orthogonal polynomial kernel and combined kernels in Support Vector Machine classifier. *Pattern Recognit* 2016;60:921–35.
- [77] Jouin M, Bressel M, Morando S, Gouriveau R, Hissel D, Péra M-C, et al. Estimating the end-of-life of PEM fuel cells: Guidelines and metrics. *Appl Energy* 2016;177:87–97.
- [78] Li Z, Outbib R, Giurgea S, Hissel D, Jemei S, Giraud A, et al. Online implementation of SVM based fault diagnosis strategy for PEMFC systems. *Appl Energy* 2016;164:284–93.
- [79] Suykens JAK, Vandewalle J. Least squares support vector machine classifiers. *Neural Process Lett* 1999;9:293–300.
- [80] Zhong Z, Zhu X, Cao G, Shi J. A hybrid multi-variable experimental model for a PEMFC. *J Power Sources* 2007;164:746–51.
- [81] Lv Y, Hong F, Yang T, Fang F, Liu J. A dynamic model for the bed temperature prediction of circulating fluidized bed boilers based on least squares support vector machine with real operational data. *Energy* 2017;124:284–94.
- [82] Suykens JAK, Vandewalle J. Recurrent Least Squares Support Vector Machines. *Circuits Syst I ...* 2000;47:1109–14.
- [83] Mercer J. Functions of Positive and Negative Type, and their Connection with the Theory of Integral Equations. *Philos Trans R Soc A Math Phys Eng Sci* 1909;209:415–46.
- [84] Huo HB, Zhu X, Cao G. Nonlinear modeling of a SOFC stack based on a least squares support vector machine. *J Power Sources* 2006;162:1220–5.
- [85] Wu X, Ye Q. Fault diagnosis and prognostic of solid oxide fuel cells. *J Power Sources* 2016;321:47–56.
- [86] Zou W, Froning D, Lu X, Lehnert W. An online spatiotemporal temperature model for high temperature polymer electrolyte fuel cells. *Energy Convers Manag* 2019;199.
- [87] Li D, Yu Y, Jin Q, Gao Z. Maximum power efficiency operation and generalized predictive control of PEM (proton exchange membrane) fuel cell. *Energy* 2014;68:210–7.
- [88] Chavan SL, Talange DB. Electrical equivalent circuit modeling and parameter estimation for PEM fuel cell. 2017 *Innov Power Adv Comput Technol i-PACT* 2017 2018:1–6.
- [89] Chavan SL, Talange DB. Statistical design of experiment approach for modeling and optimization of PEM fuel cell. *Energy Sources, Part A Recover Util Environ Eff* 2018;40:830–46.

- [90] Lü X, Wu Y, Lian J, Zhang Y, Chen C, Wang P, et al. Energy management of hybrid electric vehicles: A review of energy optimization of fuel cell hybrid power system based on genetic algorithm. *Energy Convers Manag* 2020;205:112474.
- [91] Mohamed I, Jenkins N. Proton exchange membrane (PEM) fuel cell stack configuration using genetic algorithms. *J Power Sources* 2004;131:142–6.
- [92] Li X, Deng Z, Wei D, Xu C, Cao G. Parameter optimization of thermal-model-oriented control law for PEM fuel cell stack via novel genetic algorithm. *Energy Convers Manag* 2011;52:3290–300.
- [93] Nejad HC, Farshad M, Gholamalizadeh E, Askarian B, Akbarimajd A. A novel intelligent-based method to control the output voltage of Proton Exchange Membrane Fuel Cell. *Energy Convers Manag* 2019;185:455–64.
- [94] Kang Y, Li J, Cao G, Tu H, Li J, Yang J. Dynamic temperature modeling of an SOFC using least squares support vector machines. *J Power Sources* 2008;179:683–92.
- [95] Hatti M, Tioursi M, Nouibat W. Static modelling by neural networks of a PEM fuel cell. *IECON Proc (Industrial Electron Conf 2006)*:2121–6.
- [96] Puranik S V., Keyhani A, Khorrami F. Neural network modeling of proton exchange membrane fuel cell. *IEEE Trans Energy Convers* 2010;25:474–83.
- [97] Re L Del, Allgöwer F, Glielmo L, Guardiola C, Kolmanovskz I. *Automotive Model Predictive Control: Models, Methods and Applications*. Springer; 2010.
- [98] Pei P, Yuan X, Gou J, Liang P. Dynamic response during PEM fuel cell loading-up. *Materials (Basel)* 2009;2:734–48.
- [99] Hu Z, Xu L, Song Z, Li J, Ouyang M. A semiempirical dynamic model of reversible open circuit voltage drop in a PEM fuel cell. *Int J Energy Res* 2019;43:2550–61.
- [100] Li Z, Outbib R, Giurgea S, Hissel D. Diagnosis for PEMFC systems: A data-driven approach with the capabilities of online adaptation and novel fault detection. *IEEE Trans Ind Electron* 2015;62:5164–74.
- [101] Costamagna P, De Giorgi A, Moser G, Serpico SB, Trucco A. Data-driven techniques for fault diagnosis in power generation plants based on solid oxide fuel cells. *Energy Convers Manag* 2019;180:281–91.
- [102] Han I-S, Chung CB. Performance prediction and analysis of a PEM fuel cell operating on pure oxygen using data-driven models: A comparison of artificial neural network and support vector machine. *Int J Hydrogen Energy* 2016;41:10202–11.
- [103] Jing C, Hou J. SVM and PCA based fault classification approaches for complicated industrial process. *Neurocomputing* 2015;167:636–42.
- [104] Yin Z, Hou J. Recent advances on SVM based fault diagnosis and process monitoring in complicated industrial processes. *Neurocomputing* 2016;174:643–50.
- [105] Padilha CADA, Barone DAC, Neto ADD. A multi-level approach using genetic algorithms in an ensemble of Least Squares Support Vector Machines. *Knowledge-Based Syst* 2016;106:85–95.
- [106] Pillonetto G, Dinuzzo F, Chen T, De Nicolao G, Ljung L. Kernel methods in system identification, machine learning and function estimation: A survey. *Automatica* 2014;50:657–82.
- [107] Shi Y, Janßen H, Lehnert W. A transient behavior study of polymer electrolyte fuel cells with cyclic current profiles. *Energies* 2019;12:1–13.
- [108] Zou W, Froning D, Shi Y, Lehnert W. A least-squares support vector machine method for modeling transient voltage in polymer electrolyte fuel cells. *Appl Energy* 2020;271.
- [109] Xue XD, Cheng KWE, Sutanto D. Unified mathematical modelling of steady-state and dynamic voltage-current characteristics for PEM fuel cells. *Electrochim Acta* 2006;52:1135–44.
- [110] Panha K, Fowler M, Yuan XZ, Wang H. Accelerated durability testing via reactants relative humidity cycling on PEM fuel cells. *Appl Energy* 2012;93:90–7.
- [111] Lü X, Chen C, Wang P, Meng L. Status evaluation of mobile welding robot driven by fuel cell hybrid power system based on cloud model. *Energy Convers Manag* 2019;198:111904.

- [112] Zou W, Froning D, Shi Y, Lehnert W. Working zone for a least squares support vector machine in the modeling of polymer electrolyte fuel cell voltage. Accepted by Appl Energy n.d.
- [113] Yan W, Chu H, Chen J, Soong CY, Chen F. Transient analysis of water transport in PEM fuel cells. *J Power Sources* 2006;162:1147–56.
- [114] Sutharssan T, Montalvao D, Chen YK, Wang WC, Pisac C, Elemara H. A review on prognostics and health monitoring of proton exchange membrane fuel cell. *Renew Sustain Energy Rev* 2017;75:440–50.
- [115] Garcia-Sanchez D, Ruiu T, Biswas I, Schulze M, Helmly S, Friedrich KA. Local impact of humidification on degradation in polymer electrolyte fuel cells. *J Power Sources* 2017;352.
- [116] Kadyk T, Hanke-Rauschenbach R, Sundmacher K. Nonlinear frequency response analysis of dehydration phenomena in polymer electrolyte membrane fuel cells. *Int J Hydrogen Energy* 2012;37:7689–701.
- [117] Garcia-Sanchez D, Morawietz T, da Rocha PG, Hiesgen R, Gazdzicki P, Friedrich KA. Local impact of load cycling on degradation in polymer electrolyte fuel cells. *Appl Energy* 2020;259:114210.
- [118] Zou W, Froning D, Shi Y, Lehnert W. An Online Adaptive Model for the Nonlinear Dynamics of Fuel Cell Voltage. Submitted to Appl Energy n.d.
- [119] Laref R, Losson E, Sava A, Siadat M. On the optimization of the support vector machine regression hyperparameters setting for gas sensors array applications. *Chemom Intell Lab Syst* 2019;184:22–7.
- [120] Chen K, Laghrouche S, Djerdir A. Degradation model of proton exchange membrane fuel cell based on a novel hybrid method. *Appl Energy* 2019;252:113439.
- [121] Qi Y, Espinoza-Andaluz M, Thern M, Li T, Andersson M. Dynamic modelling and controlling strategy of polymer electrolyte fuel cells. *Int J Hydrogen Energy* 2019.
- [122] Kim H, Cho CY, Nam JH, Shin D, Chung T-Y. A simple dynamic model for polymer electrolyte membrane fuel cell (PEMFC) power modules: Parameter estimation and model prediction. *Int J Hydrogen Energy* 2010;35:3656–63.
- [123] Chavan SL, Talange DB. Modeling and simulation of effect of double layer capacitance on PEM fuel cell performance. 2017 7th Int Conf Power Syst ICPS 2017 2018:259–64.
- [124] Wilberforce T, Olabi AG. Performance prediction of proton exchange membrane fuel cells (PEMFC) using adaptive neuro inference system (ANFIS). *Sustainability* 2020;12:4952.
- [125] Napoli G, Ferraro M, Sergi F, Brunaccini G, Antonucci V. Data driven models for a PEM fuel cell stack performance prediction. *Int J Hydrogen Energy* 2013;38:11628–38.
- [126] Acuña G, Möller H. Indirect training of gray-box models using LS-SVM and genetic algorithms. 2016 IEEE Lat Am Conf Comput Intell LA-CCI 2016 - Proc 2017:1–5.
- [127] Sharifi Asl SM, Rowshanzamir S, Eikani MH. Modelling and simulation of the steady-state and dynamic behaviour of a PEM fuel cell. *Energy* 2010;35:1633–46.
- [128] Laoun B, Naceur MW, Khellaf A, Kannan AM. Global sensitivity analysis of proton exchange membrane fuel cell model. *Int J Hydrogen Energy* 2016;41:9521–8.
- [129] Hosseinzadeh E, Rokni M, Rabbani A, Mortensen HH. Thermal and water management of low temperature Proton Exchange Membrane Fuel Cell in fork-lift truck power system. *Appl Energy* 2013;104:434–44.
- [130] Larminie J, Dicks A. *Fuel Cell Systems Explained*. 2nd ed. John Wiley & Sons Ltd; 2003.

List of Figures

Figure 1-1: The main parts of a PEFC in Forschungszentrum Jülich: Exposed fuel cell components.	2
Figure 2-1: Classification of dynamic models based on their dependency on mechanisms and data [45]	10
Figure 2-2: General processing procedure of black-box modeling.	14
Figure 2-3: Biological neural network [62].....	14
Figure 2-4: Configuration of an artificial neural network with three layers: one hidden layer.	15
Figure 2-5: Two hidden layers neural network model [64]	17
Figure 2-6: Neural network structure for modeling the stack-humidifier [65]	17
Figure 2-7: Classification of class 1 (circles) and class 2 (squares) data using a line classifier, having: (a) the smallest margin and (b) the largest margin [74]	20
Figure 2-8: General processing procedure of gray-box modeling.....	24
Figure 2-9: General procedures of the genetic algorithm.....	25
Figure 3-1: Dynamic voltage-current density profiles (Brown curve: current density; Black curve: cell voltage; Operating temperature: 343.15 K; $RH_{an}=100\%$; $RH_{ca} = 100\%$; Active area: 17.46 cm^2 ; $\lambda_{an} = \lambda_{ca} = 2$).	32
Figure 3-2: Greenlight Technology's G40 test stand and sensors layout	35
Figure 3-3: Current density profile. (Limited current density: 1.2 A cm^{-2} ; Ramp values: 0.1 A cm^{-2} ; Sampling interval $\Delta t = 1 \text{ s}$)	35
Figure 3-4: Anode inlet pressure: hydrogen is fueled into the anode side (Stoichiometry of both side is set as 2; Relative humidity of both sides is $RH = 90\%$; Cell temperature is $T = 343.15 \text{ K}$).....	36
Figure 3-5: Cathode inlet pressure: air is delivered into the cathode side (Stoichiometry of both side is set as 2; Relative humidity of both sides is $RH = 90\%$; Cell temperature is $T = 343.15 \text{ K}$).....	37
Figure 3-6: Output of the fuel cell: black line is the cell voltage profile and brown line is the current density profile (Stoichiometry of both side is set as 2; Relative humidity of both sides is $RH = 90\%$; Cell temperature is $T = 343.15 \text{ K}$).	37
Figure 3-7: LSSVM determination with training and testing data (Black dots: the training data; Red dots: the testing data).....	38
Figure 3-8: LSSVM model results: a) the model output against the experimental data; b) the absolute error; and c) zoomed region.....	41
Figure 3-9: Correlation between the model's output and experimental data.....	41

List of Figures

Figure 4-1: Framework of the methodology. (The LSSVM model in this chapter is the same as in the previous chapter).....	44
Figure 4-2: Configuration of the fuel cell system simulation (Four modules are included: voltage, anode, cathode and membrane module) [108].	45
Figure 4-3: Schematic of a PEFC system (Anode module: section A.3.2; Cathode module: section A.3.3; Membrane module: section A.3.4; Voltage module: A.3.1; Parameters are listed in Table 4-I and Table 4-II) [108].....	46
Figure 4-4: Artificial data approximates against the experimental data (Brown line: current density; Black line: voltage collected from the test station; Green line: cell voltage calculated by the white-box model). Details can be found in section A.3.....	48
Figure 4-5: Relative error of the white-box model (Eq.4-1).	48
Figure 4-6: Current density profile with ramp value $\Delta i = 0.4 \text{ A cm}^{-2}$, ramp time $t_{in} = 60 \text{ s}$. The artificial data was collected with a sampling interval of $\Delta t = 1 \text{ s}$ (Operating condition is listed in Table 4-II).....	49
Figure 4-7: Artificial data collection with different intervals: a) $\Delta t = 1 \text{ s}$ with zoomed region marked; b) $\Delta t = 3 \text{ s}$; and c) $\Delta t = 8 \text{ s}$; a.1) zoomed region, 1 s and 3 s; a.2) zoomed region, 1 s and 8 s (Operating condition is listed in Table 4-II).	50
Figure 4-8: Artificial data with ramp value $\Delta i = 0.2 \text{ A cm}^{-2}$, ramp time $t_{in} = 60 \text{ s}$: a. current density; b. cell voltage (Operating condition is listed in Table 4-II).	51
Figure 4-9: Artificial data with ramp value $\Delta i = 0.2 \text{ A cm}^{-2}$, ramp time $t_{in} = 180 \text{ s}$: a. current density; b. cell voltage (Operating condition is listed in Table 4-II).	52
Figure 4-10: Artificial data with ramp value $\Delta i = 0.3 \text{ A cm}^{-2}$, ramp time $t_{in} = 60 \text{ s}$ (a. current density; b. cell voltage).	53
Figure 4-11: Artificial data with ramp value $\Delta i = 0.5 \text{ A cm}^{-2}$, ramp time $t_{in} = 60 \text{ s}$ (a. current density; b. cell voltage).	53
Figure 4-12: The LSSVM model performance with data preserved with sampling interval $\Delta t = 3 \text{ s}$: a) Model output approximated against artificial data; b) absolute error (Eq. 3-6); c) zoomed region [108].	55
Figure 4-13: The LSSVM model performance with data preserved with sampling interval $\Delta t = 3 \text{ s}$: a) Model output approximated against artificial data; b) absolute error (Eq. 3-6); c) zoomed region [108].	55
Figure 4-14: Performance comparison at different sampling intervals ($\Delta t = 1, 3, 5, 8 \text{ s}$) [108].	56
Figure 4-15: Current density with ramp ramp time $t_{in} = 60 \text{ s}$ (Operating condition is listed in Table 4-II).	57

Figure 4-16: LSSVM model performance – Case 1 ($\Delta i = 0.2 \text{ A cm}^{-2}$): a) Model output approximated to artificial data; b) absolute error; c) zoomed region [108].	57
Figure 4-17: Model performance – Case 4 ($\Delta i = 0.5 \text{ A cm}^{-2}$): a) Model output approximated to artificial data; b) absolute error; c) zoomed region [108].	58
Figure 4-18: Effects of ramp value on the LSSVM model performance [108].	58
Figure 4-19: Performance analysis of the LSSVM model: $t_{in} = 60 \text{ s}$ (Top row: current density profile; Middle row: the black line is an artificial voltage and the red line is the LSSVM model's output; Bottom row: the absolute error of the model) [108]...	59
Figure 4-20: Performance analysis of the LSSVM model: $t_{in} = 180 \text{ s}$ (Top row: current density profile; Middle row: the black line is an artificial voltage and the red line is the LSSVM model's output; Bottom row: the absolute error of the model) [108]...	60
Figure 4-21: Effect of the ramp time on the LSSVM model's performance [108].	60
Figure 4-22: The coefficient of determination(R^2) among three effect factors: sampling interval (from Figure 4-22a to Figure 4-22d), ramp time (x -axis) and ramp value: A cm^{-2} (different colored lines). Higher R^2 represents better model's performance [108].	61
Figure 4-23: Performance comparison with different ramp values [108].	62
Figure 4-24: Performance comparison with different ramp times [108].	63
Figure 5-1: Voltage-current density profiles: collected from test rig (Brown line: current density; black line: cell voltage; operating temperature: 343.15 K ; $\lambda_{an} = 2.0$, $\lambda_{ca} = 2.0$; $\text{RH}_{an} = 90\%$, $\text{RH}_{ca} = 90\%$).	65
Figure 5-2 :Voltage-current density profiles collected from test rig: a) experiments No. 1; b) experiments No.3; c) experiments No. 6; d) experiments dfdfgdfgdfNo. 9 (Black line: cell voltage; brown line: current density; operating temperature: 343.15 K ; $\lambda_{an} = 2.0$, $\lambda_{ca} = 2.0$; $\text{RH}_{an} = 90\%$, $\text{RH}_{ca} = \text{sdfsdfsdfsdf}90\%$).	68
Figure 5-3: Filtering results of cell voltage, experiment No.1 in Table 5-II (Brown line: current density, black line: cell voltage collected from the test rig, blue line: smooth cell voltage removed oscillation).	70
Figure 5-4: Extracted noise from cell voltage, experiment No.1 in Table 5-II.	70
Figure 5-5: Filtering results of cell voltage, experiment No.5 in Table 5-II (Brown line: current density, black line: cell voltage collected from the test rig, blue line: smooth cell voltage removed oscillation).	71
Figure 5-6: Extracted noise from cell voltage, experiment No.5 in Table 5-II.	71
Figure 5-7: Artificial data against experimental data, experiments No.1 in Table 5-II (Brown line: current density; Black line: cell voltage collected from the test rig; Green line: artificial data with oscillation).	72
Figure 5-8: Absolute error between experimental data and artificial data.	73

Figure 5-9: Data collecting with different intervals : (a) current density; (b) cell voltage with $\Delta t = 1$ s; (c) zoomed region, 3 s; (d) zoomed region, 8 s; (e) cell voltage with $\Delta t = 3$ s; (f) cell voltage with $\Delta t = 8$ s ($T_{an} = 343.15$ K, $T_{ca} = 343.13$ K, $\lambda_{an} = \lambda_{ca} = 2$, $RH_{an}=100\%$ and $RH_{ca} = 100\%$).	74
Figure 5-10: Model performance under sampling interval $\Delta t = 3$ s.	75
Figure 5-11: Model performance under sampling interval $\Delta t = 8$ s.	76
Figure 5-12: Model performance Case 1, ramp value $\Delta i = 0.2$ A cm ⁻² : (a) current density; (b) model output against the artificial voltage; (c) absolute error of the modeling results [112].	77
Figure 5-13: Model performance Case 3, ramp value $\Delta i = 0.4$ A cm ⁻² : (a) current density; (b) model output against the real voltage; (c) absolute error of the modeling results [112].	78
Figure 5-14: Model results of nine cases.	79
Figure 5-15: Performance analysis of the LSSVM model: $t_{in} = 30$ s (Top row: current density profile; Middle row: black line is artificial voltage and red line is LSSVM model output; Bottom row: the absolute error of the model) [112].	80
Figure 5-16: Performance analysis of the LSSVM model: $t_{in} = 180$ s (Top row: current density profile; Middle row: black line is artificial voltage and red line is LSSVM model output; Bottom row: the absolute error of the model) [112].	81
Figure 5-17: Effect of ramp time on LSSVM model performance [112].	81
Figure 5-18: The value of coefficient of determination (R^2) among three effect factors: sampling interval (x-axis, positive direction: from right to left), ramp time (y-axis: positive direction: from outside to inside) and ramp value (different colored lines). Higher R^2 represents better model's performance [112].	83
Figure 5-19: The value of maximum absolute error among three effect factors: sampling interval (x-axis, positive direction: from left to right), ramp time (y-axis: positive direction: from inside to outside) and ramp value (different colored lines). Lower maximum absolute error represents better model's performance. (The red plane shows the expected maximum absolute of 0.15 V; the possible cases are under this plane) [112].	84
Figure 5-20: The value of average absolute error among three effect factors: sampling interval (x-axis, positive direction: from right to left), ramp time (y-axis: positive direction: from inside to outside) and ramp value (different colored lines). (The red plane shows an example of expected average absolute error of 0.015 V; Possible cases are under this red plane) [112].	85
Figure 6-1: Factors affecting the fuel cell performance [118].	87
Figure 6-2: Procedure of the developed adaptive LSSVM method.	88

Figure 6-3: Procedures of the genetic algorithm.	91
Figure 6-4: Schematic diagram of crossover and mutation in the genetic algorithm.	91
Figure 6-5: Configuration of the proposed method [118].	92
Figure 6-6: Current density profile and corresponding cell output voltage (Operating condition: Table 6-II) [118].	94
Figure 6-7: Relative error of each generation (Genetic algorithm) [118].	95
Figure 6-8: Updating process of γ (Eq. 6-4) [118].	96
Figure 6-9: Updating process of σ (Eq. 6-5) [118].	96
Figure 6-10: Calculation time of each updating process (Calculation was implemented using Matlab on a desktop computer with a 3.40 GHz Intel® Core™ i7-2600 CPU and with 16GB RAM) [118].	96
Figure 6-11: Model performance: prediction by the model against the real experimental data [118].	97
Figure 6-12: Relative error of the modeling results (Eq. 6-6) [118].	97
Figure 6-13: Case 2, ramp value $\Delta i = 0.2 \text{ A cm}^{-2}$ and ramp time $t_{in} = 60 \text{ s}$ (Blue line: current density profile; Black line: cell voltage collected from experiment; Operating condition: Table 6-II) [118].	98
Figure 6-14: Case 3, ramp value $\Delta i = 0.5 \text{ A cm}^{-2}$ and ramp time $t_{in} = 1 \text{ s}$ (Blue line: current density profile; Black line: cell voltage collected from experiment; Operating condition: Table 6-II) [118].	98
Figure 6-15: Case 4, ramp value $\Delta i = 0.5 \text{ A cm}^{-2}$ and ramp time $t_{in} = 60 \text{ s}$ (Blue line: current density profile; Black line: cell voltage collected from experiment; Operating condition: Table 6-II) [118].	99
Figure 6-16: Coefficient of determination (R^2): higher value represents better model performance (Case 1: $t_{in} = 1 \text{ s}$, $\Delta i = 0.2 \text{ A cm}^{-2}$; Case 2: $t_{in} = 60 \text{ s}$, $\Delta i = 0.2 \text{ A cm}^{-2}$; Case 3: $t_{in} = 1 \text{ s}$, $\Delta i = 0.5 \text{ A cm}^{-2}$; Case 4: $t_{in} = 60 \text{ s}$, $\Delta i = 0.5 \text{ A cm}^{-2}$) [118].	100
Figure 6-17: Mean absolute percentage error (MAPE): higher value represents poorer model performance (Case 1: $t_{in} = 1 \text{ s}$, $\Delta i = 0.2 \text{ A cm}^{-2}$; Case 2: $t_{in} = 60 \text{ s}$, $\Delta i = 0.2 \text{ A cm}^{-2}$; Case 3: $t_{in} = 1 \text{ s}$, $\Delta i = 0.5 \text{ A cm}^{-2}$; Case 4: $t_{in} = 60 \text{ s}$, $\Delta i = 0.5 \text{ A cm}^{-2}$) [118].	101
Figure 6-18: Coefficient of determination (R^2) of the online adaptive LSSVM model: with oscillated artificial data collected by sampling interval $\Delta t = 3 \text{ s}$	102
Figure 6-19: Coefficient of determination (R^2) of the LSSVM model: with oscillated artificial data collected by sampling interval $\Delta t = 3 \text{ s}$	102
Figure 6-20: Improvement of the online adaptive model (Eq. 6-9).	103

List of Tables

Table 2-I: Activation and transfer functions used in the ANNs [63].	16
Table 2-II: Fuzzy decision of humans whether they reach their hand into the water.	18
Table 2-III: Commonly used kernel functions [76].	21
Table 2-IV: Different modeling methods and their properties [97].	27
Table 2-V: Comparison among different black-box modeling methods.	28
Table 3-I: Results of cross-validation (hold-out method): Coefficient of determination is used to evaluate the results: higher value represents better results.	40
Table 4-I: Parameters used in the white-box model [107–109].	47
Table 4-II: Operating conditions [108].	47
Table 4-III: Ramp values: Amplitude of current density change.	49
Table 5-I: Operating conditions.	66
Table 5-II: Properties of current density profiles in test rig.	66
Table 5-III: Analyzed noises amplitude at different current densities [112].	72
Table 5-IV: Indices for the model by four sampling intervals.	76
Table 5-V: Ramp value in current density.	76
Table 5-VI: Ramp times.	79
Table 6-I: Parameters of GA.	90
Table 6-II: The fuel cell's operating condition.	93
Table 6-III: Computation time of generations (Calculation was implemented using Matlab on a desktop computer with a 3.40 GHz Intel® Core™ i7-2600 CPU and with 16GB RAM) [118].	95
Table 6-IV: Current density change characteristic of four cases.	98
Table 6-V: Properties of reference models in comparison with the proposed model.	99

Acknowledgments

Throughout my four-year doctoral research, I have received a great deal of support and assistance.

I would first like to thank my doctoral father, Professor Werner Lehnert who provided me such a valuable opportunity four years ago, so that I can study and work in the institute of energy and climate research (IEK-14) in Forschungszentrum Jülich. Your expertise is invaluable in formulating the academic questions and research methodology. Your insightful feedback after each of our discussion enlightened me and reshaped my thinking and brought my work to a higher level.

I would like to acknowledge my co-supervisor Mr. Dieter Froning for his meticulous concern and very patient instruction on my work. Thank you for checking, reviewing and modifying my research papers. Your attitude towards work inspires me and I will take it as a lifetime learning model. I do really appreciate to have you during my doctoral research. Without your help, it would be very tough to conduct my work.

I would like to thank my colleague Mr. Yan Shi for helping design and carry out the experiments. You provided me with the data that I needed and successfully complete my doctoral thesis.

I would like to appreciate the colleagues who gave me strong support during my study. Thank you Ms. Birgit Schumacher, Dr. Uwe Reimer, Dr. Holger Janßen, Dr. Yu Lin, Dr. Shidong Zhang, Dr. Shuai Liu, Dr. Yasser Rahim, Mr. Christopher Wood, Ms. Anke Clemens.

I am very grateful to have a group of lovely, interesting and outstanding colleagues: Dr. Yulin Yan, Dr. Diankai Qiu, Prof. Xu, Prof. Ni, Hui Hou, Eugen Hoppe, Sebastian Holtwerth, Jingjing Lin, Michael Sietmann, Yanpeng Suo, Dr. Philipp Irmscher, Elena Borgardt, who all helped me in different ways.

I would like to express my gratitude to the Chinese Scholarship Council (CSC) for funding my study my living in German (Grant number:201606370028).

In addition, I would like to thank my father Qing Zou and my mother Yufen Zeng for their wise counsel and sympathetic ear, for every time I doubt myself, your encourage help me regain my courage and face every challenge. At last, my deepest gratitude is to the love of my life Junting Chen. Thank you for believing in me even when I lost faith in myself, and for sharing my wish and accompanying with me till I reach the goal of completing the task.

Band / Volume 547

Effects of root temperature on food quality of horticultural crops

F. He (2021), V, 143 pp

ISBN: 978-3-95806-565-9

Band / Volume 548

Verhalten und Kontrolle von Schlacken des bioliq®-Vergasers

K. Mielke (2021), 162, XXXV pp

ISBN: 978-3-95806-566-6

Band / Volume 549

Gravity waves resolved in Numerical Weather Prediction products

C. Strube (2021), iii, 139 pp

ISBN: 978-3-95806-567-3

Band / Volume 550

Experimental study of the chemical degradation of biogenic volatile organic compounds by atmospheric OH radicals

M. Rolletter (2021), XIII, 199 pp

ISBN: 978-3-95806-568-0

Band / Volume 551

Infiltrated Positive Electrodes for All-Solid-State Sodium Batteries

T. Lan (2021), vi, 104 pp

ISBN: 978-3-95806-576-5

Band / Volume 552

Trajectory Analysis on the Asian Tropopause Aerosol Layer (ATAL) based on Balloon Measurements at the Foothills of the Himalayas

S. Hanumanthu (2021), xiv, 147 pp

ISBN: 978-3-95806-578-9

Band / Volume 553

Field assisted sintering of yttria ceramics for plasma etching applications

M. Kindelmann (2021), VI, 122, XXX pp

ISBN: 978-3-95806-579-6

Band / Volume 554

Characterisation of the effect of redox potential on the emission of greenhouse gases using wireless sensing techniques

J. Wang (2021), XIV, 104 pp

ISBN: 978-3-95806-581-9

Band / Volume 555

**Stability assessment of variably saturated hillslopes
using coupled hydromechanical models**

S. Moradi (2021), xxxii, 123 pp

ISBN: 978-3-95806-583-3

Band / Volume 556

**Catalytic-doping of Silicon Alloys for the Use in Silicon Heterojunction
Solar Cells**

Y. Liu (2021), 126 pp

ISBN: 978-3-95806-591-8

Band / Volume 557

**Formation of highly oxygenated organic molecules from α -pinene
photochemistry**

S. Kang (2021), xvii, 156 pp

ISBN: 978-3-95806-596-3

Band / Volume 558

**Synthese von Cr_2AlC MAX-Phasen Kompositen und Bestimmung ihrer
oxidativen Eigenschaften**

T. Go (2021), ii, 119 pp

ISBN: 978-3-95806-598-7

Band / Volume 559

**Distribution of Relaxation Times for Analysis of Solid Oxide
Fuel Cell Stacks**

K. Fitzek (2021), 237 pp

ISBN: 978-3-95806-599-4

Band / Volume 560

**Machine Learning in Modeling of the Dynamics of Polymer
Electrolyte Fuel Cells**

W. Zou (2021), vii, 139 pp

ISBN: 978-3-95806-601-4

Weitere **Schriften des Verlags im Forschungszentrum Jülich** unter
<http://www.zb1.fz-juelich.de/verlagextern1/index.asp>

Energie & Umwelt / Energy & Environment
Band / Volume 560
ISBN 978-3-95806-601-4